Stochastic Turing patterns in a synthetic bacterial population

David Karig[a,b,1], K. Michael Martini[c,1], Ting Lu[d,1], Nicholas A. DeLateur[e], Nigel Goldenfeld[c,2], and Ron Weiss[f,2]

[a]Research and Exploratory Development Department, Johns Hopkins University Applied Physics Laboratory, Laurel, MD 20723; [b]Department of Chemical and Biomolecular Engineering, Johns Hopkins University, Baltimore, MD 21218; [c]Department of Physics, Center for the Physics of Living Cells and Carl R. Woese Institute for Genomic Biology, University of Illinois at Urbana-Champaign, Urbana, IL 61801; [d]Department of Bioengineering and Carl R. Woese Institute for Genomic Biology, University of Illinois at Urbana-Champaign, Urbana, IL 61801; [e]Department of Chemistry, Massachusetts Institute of Technology, Cambridge, MA 02139; and [f]Department of Biological Engineering, Massachusetts Institute of Technology, Cambridge, MA 02139

Contributed by Nigel Goldenfeld, May 9, 2018 (sent for review November 29, 2017; reviewed by Raymond E. Goldstein, Eric Klavins, and Ehud Meron)

The origin of biological morphology and form is one of the deepest problems in science, underlying our understanding of development and the functioning of living systems. In 1952, Alan Turing showed that chemical morphogenesis could arise from a linear instability of a spatially uniform state, giving rise to periodic pattern formation in reaction–diffusion systems but only those with a rapidly diffusing inhibitor and a slowly diffusing activator. These conditions are disappointingly hard to achieve in nature, and the role of Turing instabilities in biological pattern formation has been called into question. Recently, the theory was extended to include noisy activator–inhibitor birth and death processes. Surprisingly, this stochastic Turing theory predicts the existence of patterns over a wide range of parameters, in particular with no severe requirement on the ratio of activator–inhibitor diffusion coefficients. To explore whether this mechanism is viable in practice, we have genetically engineered a synthetic bacterial population in which the signaling molecules form a stochastic activator–inhibitor system. The synthetic pattern-forming gene circuit destabilizes an initially homogenous lawn of genetically engineered bacteria, producing disordered patterns with tunable features on a spatial scale much larger than that of a single cell. Spatial correlations of the experimental patterns agree quantitatively with the signature predicted by theory. These results show that Turing-type pattern-forming mechanisms, if driven by stochasticity, can potentially underlie a broad range of biological patterns. These findings provide the groundwork for a unified picture of biological morphogenesis, arising from a combination of stochastic gene expression and dynamical instabilities.

Turing patterns | biofilm | synthetic biology | signaling molecules | stochastic gene expression

A central question in biological systems, particularly in developmental biology, is how patterns emerge from an initially homogeneous state (1). In his seminal 1952 paper "The chemical basis of morphogenesis," Alan Turing showed, through linear stability analysis, that stationary, periodic patterns can emerge from an initially uniform state in reaction–diffusion systems where an inhibitor morphogen diffuses sufficiently faster than an activator morphogen (2). However, the requirements for realizing robust pattern formation according to Turing's mechanism are prohibitively difficult to realize in nature. Although Turing patterns were observed in a chemical system in 1990 (3), the general role of Turing instabilities in biological pattern formation has been called into question, despite a few rare examples (ref. 4 and references therein).

Recently, Turing's theory was extended to include intrinsic noise arising from activator and inhibitor birth and death processes (5–8). According to the resulting stochastic Turing theory, demographic noise can induce persistent spatial pattern formation over a wide range of parameters, in particular, removing the requirement for the ratio of inhibitor–activator diffusion coefficients to be large. Moreover, stochastic Turing theory shows that the extreme sensitivity of pattern-forming systems to intrinsic noise stems from a giant amplification resulting from the nonorthogonality of eigenvectors of the linear stability operator about the spatially uniform steady state (8). This amplification means that the magnitude of spatial patterns arising from intrinsic noise is not limited by the noise amplitude itself, as one might have thought naively. These developments imply that intrinsic noise can drive large-amplitude stochastic Turing patterns for a much wider range of parameters than the classical, deterministic Turing theory. In particular, it is often the case in nature that the activator and inhibitor molecules do not have widely differing diffusion coefficients; nevertheless, stochastic Turing theory predicts that, even in this case, pattern formation can occur at a characteristic wavelength that has the same functional dependence on parameters as in the deterministic theory.

To explore how global spatial patterns emerge from local interactions in isogenic cell populations, we present here a synthetic bacterial population with collective interactions that can be controlled and well-characterized (an introduction to this perspective is in ref. 9), where patterning is driven by activator–inhibitor diffusion across an initially homogeneous lawn of cells. Synthetic systems can be forward-engineered to include relatively simple circuits that are loosely coupled to the larger natural

Significance

In 1952, Alan Turing proposed that biological morphogenesis could arise from a dynamical process in reaction systems with a rapidly diffusing inhibitor and a slowly diffusing activator. Turing's conditions are disappointingly hard to achieve in nature, but recent stochastic extension of the theory predicts pattern formation without such strong conditions. We have forward-engineered bacterial populations with signaling molecules that form a stochastic activator–inhibitor system that does not satisfy the classic Turing conditions but exhibits disordered patterns with a defined length scale and spatial correlations that agree quantitatively with stochastic Turing theory. Our results suggest that Turing-type mechanisms, driven by gene expression or other source of stochasticity, may underlie a much broader range of patterns in nature than currently thought.

Author contributions: D.K., K.M.M., T.L., N.G., and R.W. designed research; D.K., K.M.M., T.L., N.G., and R.W. performed research; D.K., T.L., and R.W. contributed new reagents/analytic tools; D.K., K.M.M., T.L., N.A.D., N.G., and R.W. analyzed data; D.K., K.M.M., T.L., N.A.D., N.G., and R.W. wrote the paper.

Reviewers: R.E.G., University of Cambridge; E.K., University of Washington; and E.M., Ben-Gurion University, Blaustein Institutes for Desert Research.

The authors declare no conflict of interest.

Data deposition: The DNA sequences of plasmids reported in this paper have been deposited in the GenBank database (accession nos. MH300673–MH300677).

[1]D.K., K.M.M., and T.L. contributed equally to this work.

[2]To whom correspondence may be addressed. Email: nigel@illinois.edu or rweiss@mit.edu.

This article contains supporting information online at www.pnas.org/lookup/suppl/doi:10.1073/pnas.1720770115/-/DCSupplemental.

Published online June 11, 2018.

system into which they are embedded. This makes it easier to design and control the molecular underpinnings of the biological pattern phenomenon (10) and even front propagation phenomena (11). Previous pattern formation efforts in synthetic biology have focused on oscillations in time (12) or required either an initial template (13) or an expanding population of cells (14), neither of which show a Turing mechanism.

Experimental Results

Synthetic Biology of a Bacterial Community. In our synthetic gene network design, which was guided by computational modeling (*SI Appendix*, section 1), we used two artificial diffusible morphogens: the small molecule *N*-(3-oxododecanoyl) homoserine lactone, denoted here as A3OC12HSL, and the small molecule *N*-butanoyl-L-homoserine lactone, denoted here as IC4HSL, from the *Pseudomonas aeruginosa las* and *rhl* quorum sensing pathways, respectively, in *P. aeruginosa* (15). A3OC12HSL serves as an activator of both its own synthesis and that of IC4HSL, while IC4HSL serves as an inhibitor of both signals (Fig. 1 *A* and *B* and *SI Appendix*, section 1). A3OC12HSL activates its own synthesis and synthesis of IC4HSL by binding regulatory protein LasR to form a complex that activates the hybrid promoter $P_{Las-OR1}$. This promoter regulates expression of LasI, an A3OC12HSL synthase, and RhlI, an IC4HSL synthase. To increase the sensitivity of A3OC12HSL self-activation, LasR is regulated by a second copy of $P_{Las-OR1}$. IC4HSL inhibits synthesis of A3OC12HSL and itself by forming a complex with the regulatory protein RhlR. This complex activates expression of lambda repressor CI, which in turn, represses transcription of LasI, RhlI, LasR, and RhlR. Pattern formation in our system can be modulated by altering the concentration of isopropyl β-D-1-thiogalactopyranoside (IPTG), a small molecule inducer that binds LacI and alleviates repression of $P_{Rhl-lacO}$. GFP and red fluorescent protein (RFP) are expressed from the *rhl* and *las* hybrid promoters, respectively, to aid in experimental observation (*SI Appendix*, section 2).

In our experimental setup, the A3OC12HSL activator diffuses more slowly than the IC4HSL inhibitor (*SI Appendix*, section 3). The estimated diffusion coefficient for A3OC12HSL is 83 $\mu m^2/s$, and for IC4HSL, it is 1,810 $\mu m^2/s$. The experimentally determined ratio of diffusion rates in our system of 21.6 is much higher than the value of 1.5 predicted by Wilke–Chang correlation in water (16), likely due to partitioning of A3OC12HSL in the cell membrane, which slows its diffusion from cell to cell (17). The slower diffusion rate of A3OC12HSL coupled with positive feedback regulating its synthesis allows A3OC12HSL to aggregate in local domains, leading to formation of visible red fluorescent spots (cellular lawn illustration is shown in Fig. 1*C*). Within these red domains, both A3OC12HSL and IC4HSL are found in high concentrations, but because A3OC12HSL competitively binds RhlR (*SI Appendix*, section 4 and Fig. S8), GFP is attenuated (18). The faster diffusion rate of IC4HSL allows it to diffuse into regions outside of the red fluorescent domains. Here, IC4HSL is free to bind RhlR, activating GFP expression. Collectively, these processes lead to green regions between red spots.

Experimental Patterns and Controls. To study pattern-forming behavior, engineered cells are first cultured in liquid media, and then, they are concentrated and plated on a petri dish to form an initially homogeneous "lawn" of cells (*Materials and Methods*). After plating, the petri dish is incubated for 24 h at 30 °C, and microscope fluorescence images are captured as needed. Before the self-activation of the A3OC12HSL synthase positive feedback loop, the cell lawn exhibits no fluorescence. However, over time, red fluorescent spots emerge with sizes much larger than that of a single cell (10–1,000×). Simultaneously, green fluorescence develops in a pattern with dark voids positioned precisely in the locations of the intense red fluorescence (Fig. 2*A*). Time series microscopy reveals that patterns begin to emerge after approximately 16 h (*SI Appendix*, Fig. S12).

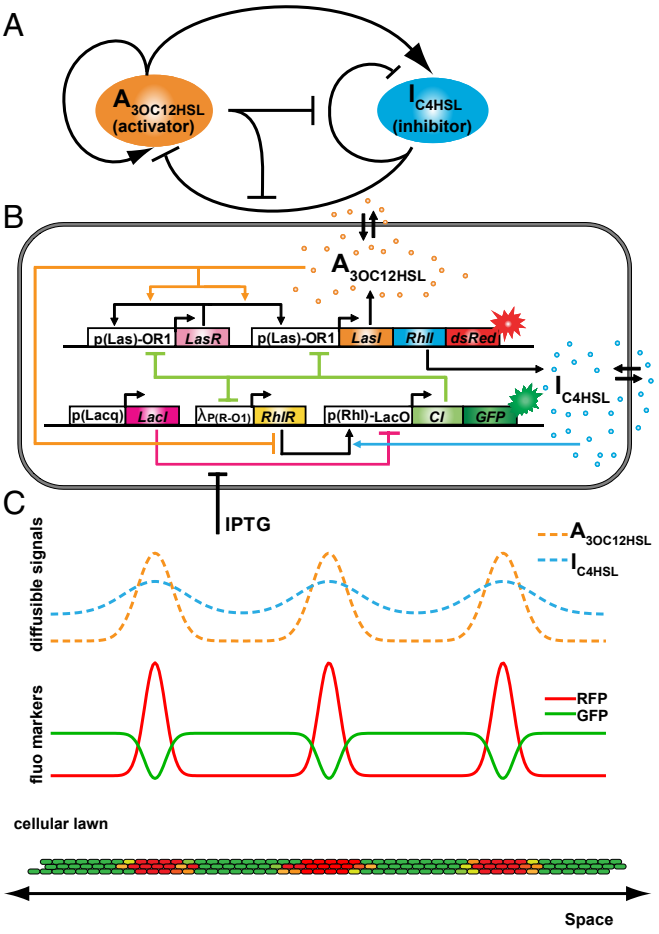

Fig. 1. Design of a synthetic multicellular system for emergent pattern formation. (*A*) Abstractly, the system consists of two signaling species A3OC12HSL and IC4HSL. A3OC12HSL is an activator catalyzing synthesis of both species, while IC4HSL is an inhibitor repressing their synthesis, with additional repression by A3OC12HSL via competitive binding. (*B*) Genetic circuit implementation. Promoter regions are indicated by white boxes, while protein coding sequences are indicated by colored boxes. IPTG is an external inducer modulating system dynamics. (*C*, *Top*) Illustration of signaling species concentrations in 1D space. The dashed orange and blue lines correspond to A3OC12HSL and IC4HSL, respectively. (*C*, *Middle*) Spatial profiles of reporter proteins. RFP expression (red line) correlates with A3OC12HSL concentrations, while GFP expression (green line) roughly mirrors RFP expression. (*C*, *Bottom*) A vertical slice of cell lawn. Cells express fluorescence proteins according to the profiles above and produce a global multicellular pattern.

In control experiments, we show that our patterns are not simply a result of the outward growth of clusters of differentially colored cells (Fig. 2 *B* and *C* and *SI Appendix*, section 5). Also, by performing an experiment with cells that harbor independent bistable green/red toggle switches, we test whether observable patterns would emerge if individual cells autonomously made cell fate decisions at some point after plating (*SI Appendix*, section 5). The fluorescence fields after 24 h of incubation at 30 °C in both control experiments are uniform, showing no emergence of patterns.

Next, we examine how changes in the strengths of localized interactions lead to different global outcomes in our pattern-forming gene circuit. In our system, IPTG can be used to modulate the inhibitory efficiency of IC4HSL in individual cells by affecting CI expression from $P_{Rhl-lacO}$. Specifically, IPTG relieves LacI repression of CI and GFP reporter. The increased range of CI ultimately increases inhibition of both morphogens, which is expected to decrease activator spot sizes, while causing

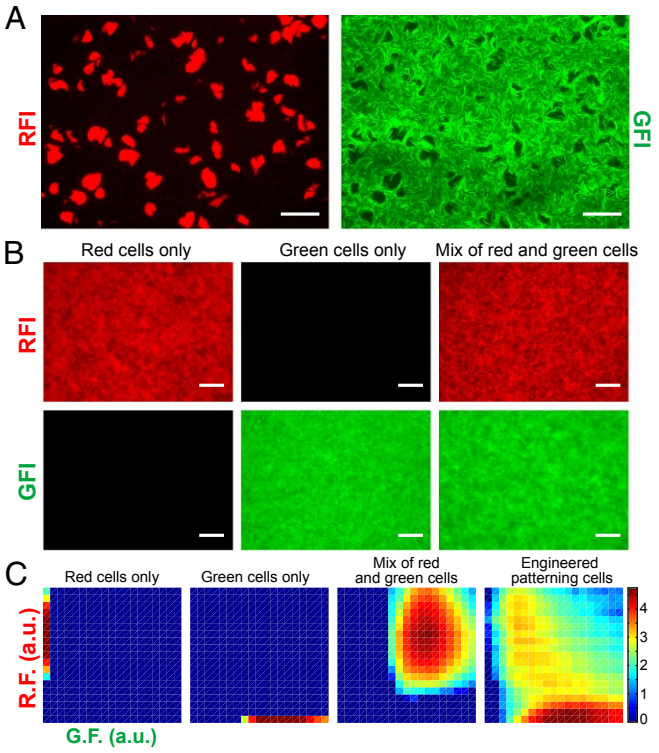

Fig. 2. Experimental observations of emergent pattern formation measured by green fluorescence intensity (GFI) and red fluorescence intensity (RFI). (*A*) Representative microscope images (based on six technical replicates) of a typical field of view showing a fluorescent pattern formed by an initially homogeneous isogenic lawn of cells harboring the Turing circuit with no IPTG. Spots and voids appear in the red fluorescence (RF) and green fluorescence (GF) channels, respectively. (Scale bar: 100 μm.) (*B*) Microscope images of cell lawns with constitutive expression of fluorescent proteins. (*Left*) Cells expressing RFP, (*Center*) cells expressing GFP, and (*Right*) mixed population of red and green cells. (*C*) Fluorescence density plots computed from the images above (from left to right: red, green, red/green, and Turing). Color intensity is in log scale [arbitrary units (a.u.)].

the field of CI and GFP reporter to be more strongly expressed. Our data show that mean GFP levels increase sigmoidally with inducer concentration, while the overall area of red spots decreases (Fig. 3 *A* and *C*). In addition to offering further support that our gene circuit gives rise to emergent patterns, these results show how pattern formation characteristics can potentially be tuned to fit future application needs.

Theoretical Results

Having established that our system forms emergent patterns, we proceeded to study the mechanisms driving these patterns. We formulated deterministic and stochastic models and analyzed our data to assess agreement with the theory of stochastic Turing patterns.

Deterministic Model. We first developed a detailed deterministic reaction–diffusion model (*SI Appendix*, section 7). The model explicitly describes chemical reactions for the LasI and RhlI synthases, regulatory protein CI, and synthesis and diffusion of the morphogens A3OC12HSL and IC4HSL. As the overall system involves a large number of reactions with rate constants that span multiple timescales, we made two commonly used simplifying assumptions. First, we assume that operator states of a promoter fluctuate much faster than protein degradation rates. Second, we assume that mRNA half-life is much shorter than protein half-life. These assumptions allow us to eliminate operator fluctuation and mRNA kinetics and model the system at the communication signals and protein levels as follows:

$$\frac{\partial U}{\partial t} = \alpha_u I_u - \gamma_u U + D_u \nabla^2 U \quad [1]$$

$$\frac{\partial V}{\partial t} = \alpha_v I_v - \gamma_v V + D_v \nabla^2 V \quad [2]$$

$$\frac{\partial I_u}{\partial t} = \alpha_{iu} F_1(X_1, C) - \gamma_{iu} I_u \quad [3]$$

$$\frac{\partial I_v}{\partial t} = \alpha_{iv} F_1(X_1, C) - \gamma_{iv} I_v \quad [4]$$

$$\frac{\partial C}{\partial t} = \alpha_c F_2(X_2, L) - \gamma_c C, \quad [5]$$

where U and V are the concentrations of the two diffusible morphogens A3OC12HSL and IC4HSL, respectively; I_u and I_v are the concentrations of corresponding acyl homoserine lactone (AHL) synthases, respectively; and C refers to CI.

We model the hybrid promoters using the following Hill functions:

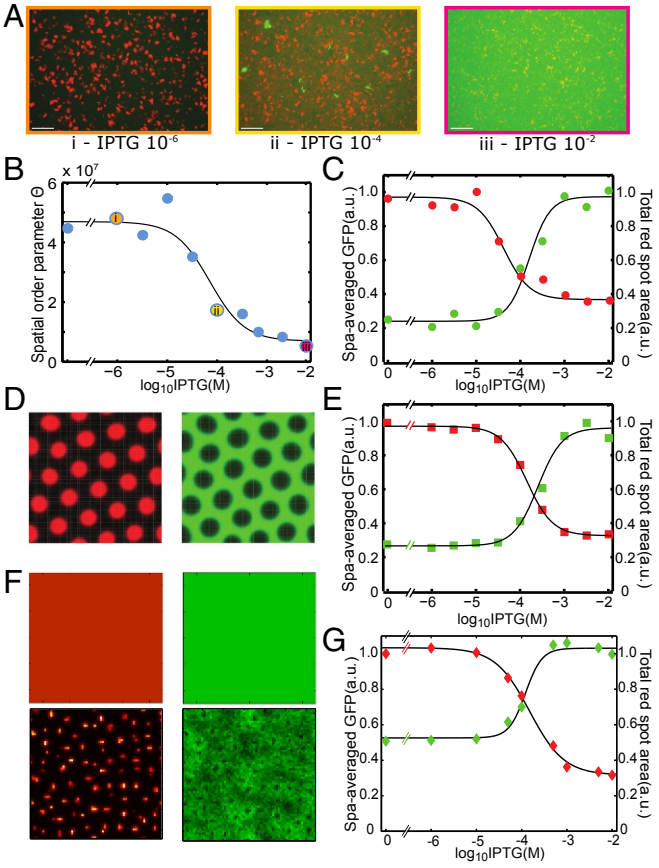

Fig. 3. Mathematical modeling and correlation between pattern modulation experiments and simulations. (*A*) Experimental results for IPTG modulation of pattern formation with microscopy images corresponding to specific IPTG concentrations in *B*. The same display mappings were used for all images in *A*. (*B*) Collectivity, metric parameter Θ is influenced by IPTG modulation. (*C*) Pattern statistics over IPTG modulation for experimental results. (*D*) Pattern obtained from simulating a deterministic reaction–diffusion model with $D_v/D_u = 100$. (*E*) Pattern statistics over IPTG modulation for deterministic modeling. (*F*) Patterns obtained from simulating our deterministic model (*Upper*) and stochastic spatiotemporal model (*Lower*) at the measured diffusion ratio of $D_v/D_u = 21.6$. (*G*) Pattern statistics over IPTG modulation for stochastic modeling. a.u., arbitrary unit.

$$F_1(X_1, C) = \frac{\left[1 + f_1\left(\frac{X_1}{K_{d1}}\right)^{\theta_1}\right]\left[1 + f_2^{-1}\left(\frac{C}{K_{d2}}\right)^{\theta_2}\right]}{\left[1 + \left(\frac{X_1}{K_{d1}}\right)^{\theta_1}\right]\left[1 + \left(\frac{C}{K_{d2}}\right)^{\theta_2}\right]} \quad [6]$$

$$F_2(X_2, L) = \frac{\left[1 + f_3\left(\frac{X_2}{K_{d3}}\right)^{\theta_3}\right]\left[1 + f_4^{-1}\left(\frac{L}{K_{d4}}\right)^{\theta_4}\right]}{\left[1 + \left(\frac{X_2}{K_{d3}}\right)^{\theta_3}\right]\left[1 + \left(\frac{L}{K_{d4}}\right)^{\theta_4}\right]}, \quad [7]$$

where $F_1(X_1, C)$ and $F_2(X_2, L)$ are the production rates of the promoters $P_{Las-OR1}$ and $P_{Rhl-lacO}$, respectively; X_1 and X_2 are the LasR-A3OC12HSL complex and the RhlR-IC4HSL complex, respectively; and L is the concentration of unbound LacI protein. We use the definitions

$$X_1 = R_u U \quad [8]$$

$$X_2 = \frac{R_v V}{(1 + U/K_{c3})} \quad [9]$$

$$L = \lambda_l \left(\frac{1 + f_6^{-1}(I/K_{d6})^{\theta_6}}{1 + (I/K_{d6})^{\theta_6}}\right), \quad [10]$$

where I is the IPTG concentration and R_u and R_v are the regulatory proteins LasR and RhlR, respectively:

$$R_u = \lambda_u I_u \quad [11]$$

$$R_v = \lambda_v \left(\frac{1 + f_5^{-1}(C/K_{d5})^{\theta_5}}{1 + (C/K_{d5})^{\theta_5}}\right). \quad [12]$$

A summary of the variables used in our model is available in *SI Appendix*, Table S5, and definitions of the rate constants are in *SI Appendix*, Tables S6 and S7. Hill functions used in this model have a shared form of $Y = \frac{1+f(X/K)^{\theta}}{1+(X/K)^{\theta}}$, where X and Y correspond to the input and output of the function, respectively; K is the dissociation constant; θ is the Hill coefficient; and f is the fold change of Y on full induction by X.

We initially ran simulations of this model using a high diffusion rate ratio ($\frac{D_v}{D_u}$) of 100. These simulations yield patterns of red spots and green voids (Fig. 3*D*), suggesting that the underlying dynamics of our system are Turing-like, with the potential for Turing instabilities. Deterministic simulations of IPTG modulations also correlate well with the trends of the experimental results (Fig. 3*E* and *SI Appendix*, section 6).

While the overall behavior of our system is reminiscent of classical Turing patterns (19), there are key differences. In particular, when we ran simulations at the measured diffusion rate ratio of $\frac{D_v}{D_u} \approx 21.6$, patterns did not arise (Fig. 3*F*). For some two-node implementations of Turing systems, this rate would be sufficient for pattern formation (20). In addition, certain networks with more nodes can allow small or even equal morphogen diffusion rate ratios to generate Turing instabilities (21). However, a practical biological implementation imposes certain dynamics, such as delays associated with protein production, that can strongly impact pattern formation (22, 23). Indeed, our deterministic modeling results suggest that the ratio of diffusion constants for the activator and inhibitor in our system is either barely within the range required for a Turing instability or even outside the range, depending on the precise medium in which signal diffusion is measured (*SI Appendix*, section 7). In addition, whereas in the deterministic simulation, spots are identical and evenly distributed, those in the experimental systems vary in size, shape, fluorescence intensity, and the intervals between them.

Stochastic Model. The deterministic modeling results indicate that our system may be beyond the regime where classical Turing patterns are formed but still within the regime where stochastic Turing patterns occur (5–8). Indeed, gene expression in microbes is inherently noisy due to the small volume of cells and the fact that many reactants are present in low numbers, suggesting that stochastic Turing patterns could be present in our system (24).

Noise in stochastic Turing patterns expands the range of parameters in which patterns form, in contrast to the usual expectation that noise serves as a destabilizing agent. The patterns observed in stochastic Turing systems correspond to the slowest decaying mode of the fluctuations. Similar noise stabilization phenomena can be observed in other systems that are out of equilibrium. For example, in predator–prey systems, fluctuations can drive temporal oscillations of populations (25, 26). Noise-driven stabilization has also been recently discovered in the clustering of molecules on biological membranes (27, 28) and in models that exhibit Turing-like pattern formation (7). In particular, whereas spatial symmetry breaking and pattern formation via the original Turing design require two morphogens with diffusion rates that differ by a large factor on the order of 10 or 100 (1), the requirements to form stochastic Turing patterns are less stringent. For example, in a pattern-forming plankton–herbivore ecosystem, the noise associated with discrete random birth and death processes reduces the required ratio of diffusion constants for pattern formation from a threshold of 27.8 for normal Turing patterns to a threshold of 2.48 for stochastic Turing patterns (5–8).

To determine whether noise in the chemical reactions underlying gene expression and morphogen diffusion in our system can cause the emergence of patterns over a wider range of parameters than a deterministic model, we constructed a stochastic spatiotemporal model using the same biochemical reactions, diffusion, and rate constants used in our deterministic model (*SI Appendix*, section 8). This model captures stochastic effects in the production and degradation of the proteins and morphogens in our system but approximates diffusion as deterministic. Simulations of the stochastic model generically produce patterns with large variability in spot size, shape, intensity, and intervals, which are similar to the patterns observed in our experiments and different from those predicted for the deterministic model (Fig. 3*F*). We have compared the experimental patterns with stochastic simulations in both real space and in 2D Fourier transform (2DFT) space (*SI Appendix*, section 8). Neither the experimental 2DFT nor the simulated 2DFT contain pronounced peaks that would be present in a deterministic honeycomb Turing pattern. Moreover, as the IPTG concentration is increased, both experimental and simulated patterns become more regular (Fig. 3*G*).

To further test the hypothesis that we are observing stochastic Turing patterns, we measured the power spectrum for both of our fluorescent reporters. Theory predicts that the power spectrum will have a power law tail as a function of wavenumber, k, for large wavenumbers, with an exponent characteristic of the noise source (7, 25). The exponent values are -2 and -4 for stochastic Turing patterns and deterministic Turing patterns with additive noise, respectively, and can be interpreted simply as follows. The -2 arises, because at small frequency or wavenumber, the random variable (i.e., concentration) is simply diffusing and therefore, follows the behavior of a random walk, which has a power spectrum that exhibits a -2 power law. The -4 arises, because for a system that is executing deterministic damped periodic motion but driven by additive white noise, the response of the random variable is a Lorentzian, with an asymptotic behavior for the power spectrum that exhibits a -4 exponent.

For the GFP channel, we observe a power law tail with an exponent of -2.3 ± 0.4 (Fig. 4*B* and *SI Appendix*, section 9A). For the RFP channel, we also observe a power law tail with an exponent of -3.9 ± 0.4 (*SI Appendix*, section 9A). To better understand the implications of these tails, we examined our detailed stochastic model of the genetic systems and also developed a reduced stochastic model that explicitly includes only the morphogens (*SI Appendix*, section 9B). Both models

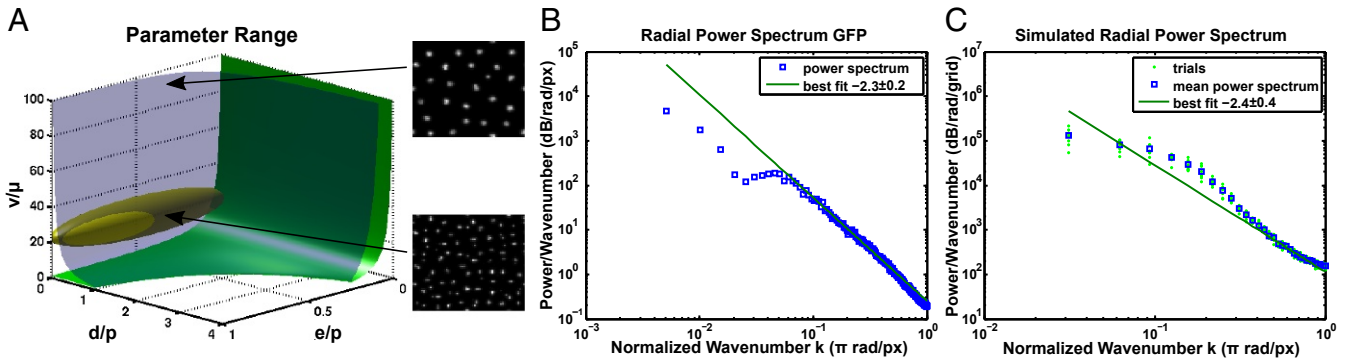

Fig. 4. Spectral analysis and parameter analysis. (*A*) Pattern-forming regimes in parameter space and estimated parameters for our system. Parameters above the green surface of neutral stochastic stability can form stochastic patterns, and parameters above the blue surface of deterministic neutral stability can form deterministic Turing patterns. The ratio of the diffusion coefficients ν/μ, the ratio of degradation rate to production rate d/p, and the ratio of production rates are estimated for our system by the yellow ellipsoid. The parameters for our system are mostly in the regime where stochastic patterns form and outside the region where deterministic Turing patterns form. Example stochastic simulations are shown for parameters drawn from a deterministic parameter region with $D_\nu/D_\mu = 100$ (*Upper Right*) and a stochastic region with $D_\nu/D_\mu = 21.6$ (*Lower Right*). (*B*) Radial power spectrum of green fluorescence and best fit power law tail with an exponent of -2.3 ± 0.2. (*C*) Radial power spectrum for eight trials of our stochastic simulation, their mean, and the best fit power law tail.

predict that our experimental parameters will produce a stochastic pattern with a power law tail of -2 for both the activator and the inhibitor at asymptotically large wavenumbers (Fig 4*C* and *SI Appendix*, section 9C). However, in the range of parameters likely to correspond to the experiments (Fig. 4*A* and *SI Appendix*, section 9C), the detailed stochastic model predicts that the exponent of the power law tail for the activator will be -4 over a large range of intermediate wavenumbers before it eventually undergoes a cross-over to a power law with an exponent -2 at high wavenumbers (*SI Appendix*, Fig. S24). This behavior once again agrees with our experimental data and supports our identification of stochastic Turing patterns. In summary, spectral analysis of the patterns of activator and inhibitor is consistent with a model in which fluctuations in the amount of signaling morphogens drive stochastic Turing patterns.

Our analysis of the stochastic Turing model predicts that stochastic patterns form over a wide range of parameters (*SI Appendix*, section 8). Indeed, our stochastic model predicts that stochastic Turing patterns are possible at the measured ratio of diffusion rates for A3OC12HSL and IC4HSL (Figs. 3*F* and 4*A*). In addition, to determine the sensitivity of the stochastic model to the parameters chosen, we individually varied parameters from $0.5\times$ their nominal value to $1.5\times$ their nominal value while keeping all other parameters fixed at their best estimated value. For each set of parameters, we calculate the analytical power spectrum and the eigenvalues of the Jacobian (linear stability matrix) of the stochastic model evaluated at a fixed point found numerically. Based on this analysis (*SI Appendix*, section 8), we classify each set of parameters as producing an unstable homogeneous state at wavenumber $k = 0$, a stable homogeneous state, a stochastic Turing pattern, or a deterministic Turing pattern. Specifically, we classify a set of parameters as producing a pattern if they produce a peak in the calculated power spectrum at a nonzero wavenumber. To distinguish between stochastic Turing patterns and deterministic Turing patterns, we examine the eigenvalues of the corresponding Jacobian. If the real part of all of the eigenvalues is negative for all wavenumbers, then the pattern must be due to stochasticity. If there is any range of wavenumbers that have corresponding positive real parts of their eigenvalues, then the pattern is produced by the traditional Turing mechanism. The results of this analysis are shown in *SI Appendix*, Fig. S22 and illustrate the significant ranges for each parameter that can lead to stochastic Turing patterns. Indeed, the estimated parameter values yield stochastic Turing patterns and variation of D_u, D_v, and IPTG, and several other parameters never produce deterministic patterns; therefore, our results are very insensitive to estimation error of these important parameters. Overall, varying the parameters one at a time, 68% of the values yield stochastic Turing patterns.

To quantify the way in which stochasticity enlarges the pattern-forming regime of parameter space, we simultaneously varied all model parameters and performed the classification used above. Specifically, we used Latin hypercube sampling to randomly generate 500 parameter sets, where all of the parameters were allowed to vary between $0.5\times$ and $1.5\times$ their nominal value. For this analysis, we found that 24.8% of parameters produced unstable fixed points, 43.2% produced stable homogeneous states, 13.2% produced stochastic Turing patterns, and 18.8% produced Turing patterns. Thus, over this arbitrarily large range of parameters, pattern formation occurs only 18.8% of the time in the absence of stochasticity but 32% of the time when stochasticity is included. By including stochasticity, the range in which patterns can form has been increased by 70%.

Discussion

Alternative Hypotheses. Now, we consider alternative hypotheses to our claim that the theory of stochastic Turing patterns explains our experimental observations. We consider the duration and dynamics of our pattern formation experiments. One may expect to observe early events in Turing pattern formation, such as splitting of clusters or increases in intercluster distances. These processes may be, in fact, be taking place but may be difficult to observe due to weak reporter expression in the earlier stages. In addition, we must consider the limited duration of our experiments and the possibility that, theoretically, longer observations may result in different patterns if nonlinear processes eventually began to dominate dynamics. Indeed, we do not feed fresh nutrients to sustain the system for extremely long durations. However, as confirmed by analysis of the dynamics in *SI Appendix*, Fig. S12, cluster size growth and spacing between clusters appear to be stabilizing toward the end of the experiment. In addition, domains are neither created nor destroyed in the later time periods. Essentially, it appears that the patterns are close to stabilizing within the 32-h observation period.

Another alternative hypothesis is that cell growth dynamics primarily drive the observed pattern formation. Our control experiments with mixtures of red and green cell populations (*SI Appendix*, Fig. S9) along with our bistable switch control (*SI Appendix*, Fig. S10) suggest that cell growth does not explain our patterns. Moreover, our ability to tune pattern characteristics offers support for the fact that our patterns are not a simple consequence of natural biofilm growth morphologies but rather, are driven by our genetic circuit. However, growth may indeed impact regularity and may likely explain the fact that our

experimental patterns are less regular than those observed in our stochastic models (Fig. 3*F*). Indeed, future experiments to show different classes of patterns (e.g., labyrinth patterns) would offer further support, but collectively, our experiments strongly support our hypothesis that a Turing mechanism driven by our genetic circuit explains our observed patterns.

Summary of Evidence for Stochastic Turing Patterns. We summarize our evidence for showing stochastic Turing patterns and not showing amplification of random noise as follows. Our control experiments with mixtures of red and green cells (Fig. 2*B* and *SI Appendix*, Fig. S9) along with a bistable switch (*SI Appendix*, Fig. S10) did not produce the patterns that we observe with our genetic circuit (Fig. 2*A*). Our ability to tune pattern characteristics offers further support that pattern formation is driven by our genetic circuit. In addition to our experimental controls, we identify patterns in the stochastic model but not in the deterministic model of our system for the experimentally observed ratio of diffusion rates (Fig. 3*F*). These model patterns resemble the experimentally observed patterns in real space, exhibit no peaks in the 2DFT (*SI Appendix*, Figs. S13 and S20), and recapitulate the observed trend with IPTG variation. Analyses of our experimental data are also in accord with the theory of stochastic Turing patterns. The exponents in the tails of the experimental radial power spectra agree with theoretical predictions (Fig. 4*B* and *SI Appendix*, Fig. S13). In addition, although spatial regularity is weak, we observe a radial spectral peak for our experimental patterns (Fig. 4*B* and *SI Appendix*, Fig. S13), indicating a characteristic length scale. Furthermore, exploration of the large parameter space of the stochastic model indicates that the experimental parameters are most likely to be in the regime where only stochastic patterns can form (*SI Appendix*, section 8). Collectively, this body of evidence suggests that our experiments indeed exhibit stochastic Turing pattern formation.

Materials and Methods

Strains and Conditions. Our patterning system was constructed using two plasmids that correspond to the upper and lower portions of the circuit diagram in Fig. 1*B*: pFNK512 and pFNK806 in Fig. 2*A* and pFNK512 and pFNK804lacOlacI in Fig. 3. The two-color bistable toggle switch plasmid pTOG-1 was constructed from plasmid pIKE-107. All plasmids were constructed using standard cloning and DNA recombination techniques. Plasmid construction details are described here and in *SI Appendix*, section 2. *Escherichia coli* strain MG1655 was used for all experiments.

Code Availability. Custom code used in this manuscript is currently available at https://www.dropbox.com/sh/di3hbaaubx5qd0q/AADpSOMfJtm_F_lEDRFoch0sa?dl=0.

Experimental Procedure. Cells harboring appropriate plasmids were initially grown in LB liquid media with corresponding antibiotics at 30 °C until OD at 600 nm was reached $0.1 - 0.3$. Cells were then concentrated and resuspended in M9 media with appropriate antibiotics (29); 0.5 mL of concentrated cell solutions ($OD_{600} = 2.0$) were poured onto a 2% M9 agar plate (60×15-mm petri dish) to form a cellular lawn. Plates were incubated at 30 °C, and fluorescence images were captured periodically. To examine the single-cell fluorescence evolution of toggle switch cell populations, we performed flow cytometry at the beginning of the experiment (0 h) and the end of the experiment (24 h).

Data Analysis. Fluorescence density plots, power spectrum of green fluorescence, averaged green fluorescence, total area of red spots, collectivity metric, and Moran's I were all computed by analyzing the experimental time-lapse microscopy data with custom Matlab software.

Mathematical Modeling. The patterning system was simulated by numerically integrating differential equations using in house-developed C software. We also developed stochastic spatiotemporal models using a hybrid stochastic simulation algorithm (30). *SI Appendix* has details about the models and the simulation environments.

Note Added in Proof. After the completion and acceptance of this work, an independent observation of stochastic Turing patterns in the cyanobacteria colonies of *Anabaena* sp. was reported (31).

ACKNOWLEDGMENTS. We thank D. Volfson and T. Danino for help in mathematical modeling and E. Andrianantoo for help in plasmid construction. We also thank R. Mehreja and J. Ku for help in creation of the RhlR mutant. We thank members of the laboratory of R.W., especially N. Davidsohn, J. Sun, S. Gupta, M. Chen, C. Grecu, L. Wroblewska, and Y. Li, for discussions. This work was supported by the NIH and National Science Foundation Grants CCF-1521925 and CNS-1446474. D.K. acknowledges support from the Independent Research and Development Program of the Johns Hopkins University Applied Physics Laboratory. K.M.M. acknowledges partial support from the Center for the Physics of Living Cells through National Science Foundation Physics Frontiers Center Program PHY 1430124.

1. Gierer A, Meinhardt H (1972) A theory of biological pattern formation. *Biol Cybern* 12:30–39.
2. Turing A (1952) The chemical basis of morphogenesis. *Philos Trans R Soc Lond Ser B Biol Sci* 237:37–72.
3. Castets V, Dulos E, Boissonade J, De Kepper P (1990) Experimental evidence of a sustained standing Turing-type nonequilibrium chemical pattern. *Phys Rev Lett* 64:2953–2956.
4. Raspopovic J, Marcon L, Russo L, Sharpe J (2014) Digit patterning is controlled by a Bmp-Sox9-Wnt Turing network modulated by morphogen gradients. *Science* 345:566–570.
5. Butler T, Goldenfeld N (2009) Robust ecological pattern formation induced by demographic noise. *Phys Rev E* 80:030902.
6. Biancalani T, Fanelli D, Di Patti F (2010) Stochastic turing patterns in the brusselator model. *Phys Rev E* 81:046215.
7. Butler T, Goldenfeld N (2011) Fluctuation-driven turing patterns. *Phys Rev E* 84:011112.
8. Biancalani T, Jafarpour F, Goldenfeld N (2017) Giant amplification of noise in fluctuation-induced pattern formation. *Phys Rev Lett* 118:018101.
9. Scholes NS, Isalan M (2017) A three-step framework for programming pattern formation. *Curr Opin Chem Biol* 40:1–7.
10. Andrianantoandro E, Basu S, Karig D, Weiss R (2006) Synthetic biology: New engineering rules for an emerging discipline. *Mol Syst Biol* 2:0028.
11. Tayar AM, Karzbrun E, Noireaux V, Bar-Ziv RH (2015) Propagating gene expression fronts in a one-dimensional coupled system of artificial cells. *Nat Phys* 11:1037–1041.
12. Stricker J, et al. (2008) A fast, robust and tunable synthetic gene oscillator. *Nature* 456:516–519.
13. Fernandez-Rodriguez J, Moser F, Song M, Voigt CA (2017) Engineering RGB color vision into Escherichia coli. *Nat Chem Biol* 13:706–708.
14. Liu C, et al. (2011) Sequential establishment of stripe patterns in an expanding cell population. *Science* 334:238–241.
15. Pesci E, Iglewski B (1997) The chain of command in Pseudomonas quorum sensing. *Trends Microbiol* 5:132–134.
16. Stewart P (2003) Diffusion in biofilms. *J Bacteriol* 185:1485–1491.
17. Pearson J, Van Delden C, Iglewski B (1999) Active efflux and diffusion are involved in transport of Pseudomonas aeruginosa cell-to-cell signals. *J Bacteriol* 181:1203–1210.
18. Pesci E, Pearson J, Seed P, Iglewski B (1997) Regulation of las and rhl quorum sensing in Pseudomonas aeruginosa. *J Bacteriol* 179:3127–3132.
19. Kondo S, Miura T (2010) Reaction-diffusion model as a framework for understanding biological pattern formation. *Science* 329:1616–1620.
20. Hagberg A, Meron E (1994) Pattern formation in non-gradient reaction-diffusion systems: The effects of front bifurcations. *Nonlinearity* 7:805–835.
21. Marcon L, Diego X, Sharpe J, Müller P (2016) High-throughput mathematical analysis identifies turing networks for patterning with equally diffusing signals. *eLife* 5:e14022.
22. Gaffney EA, Monk NAM (2006) Gene expression time delays and Turing pattern formation systems. *Bull Math Biol* 68:99–130.
23. Seirin Lee S, Gaffney EA, Monk NAM (2010) The influence of gene expression time delays on Gierer–Meinhardt pattern formation systems. *Bull Math Biol* 72:2139–2160.
24. Kærn M, Elston TC, Blake WJ, Collins JJ (2005) Stochasticity in gene expression: From theories to phenotypes. *Nat Rev Genet* 6:451–464.
25. McKane AJ, Newman TJ (2005) Predator-prey cycles from resonant amplification of demographic stochasticity. *Phys Rev Lett* 94:218102.
26. Howard M, Rutenberg AD (2003) Pattern formation inside bacteria: Fluctuations due to the low copy number of proteins. *Phys Rev Lett* 90:128102.
27. Wehrens M, ten Wolde PR, Mugler A (2014) Positive feedback can lead to dynamic nanometer-scale clustering on cell membranes. *J Chem Phys* 141:205102.
28. Altschuler SJ, Angenent SB, Wang Y, Wu LF (2008) On the spontaneous emergence of cell polarity. *Nature* 454:886–889.
29. Brenner K, Karig D, Weiss R, Arnold F (2007) Engineered bidirectional communication mediates a consensus in a microbial biofilm consortium. *Proc Natl Acad Sci USA* 104:17300–17304.
30. Rossinelli D, Bayati B, Koumoutsakos P (2008) Accelerated stochastic and hybrid methods for spatial simulations of reaction–diffusion systems. *Chem Phys Lett* 451:136–140.
31. Di Patti F, et al. (2018) Robust stochastic Turing patterns in the development of a one-dimensional cyanobacterial organism. *PLoS Biol* 16:e2004877.

Supplementary Information for Stochastic Turing patterns in a synthetic bacterial population

David Karig et al. 10.1073/pnas.XXXXXXXXXX

1. System design

Turing-type pattern formation is based on short range activation and long range inhibition in a system of interacting "morphogen" species. As shown by Gierer and Meinhardt, one short range, dissipative "activator" morphogen must be autocatalytic, and there are two general possibilities for the longer range morphogen (1). In one type of system, the longer range species inhibits the activator. Alternatively, the longer range species may serve as a substrate necessary for catalysis of the activator, and the long range inhibition effectively occurs through depletion of this substrate. Implementing Turing pattern formation in cells requires two non-interacting intercellular signaling pathways such that one signal serves as the "activator," while the other serves as either the "inhibitor" or "substrate." We chose to use elements from the Las and Rhl quorum sensing systems of *Pseudomonas aeruginosa*, such that $A_{3OC12HSL}$ is effectively the "activator" and I_{C4HSL} is the "inhibitor" (Fig. S1a). Evidence suggested that certain promoters in *P. aeruginosa* respond specifically to either I_{C4HSL}/RhlR or $A_{3OC12HSL}$/LasR (2–4). These systems were also appealing due to the different diffusion properties of the $A_{3OC12HSL}$ and I_{C4HSL} signal molecules (5). We explore these signal specificity and diffusion aspects in detail in later sections.

Designing complex multicellular systems such as a Turing pattern formation system requires the use of computational modeling. Many more reactions are necessary for a biological implementation than for a simple chemical implementation, as the activator and inhibitor do not directly interact. Rather, the system in Figure S1a must be implemented through several signal-protein, protein-protein, and protein-DNA interactions. Due to the number of reactions and of different design variations possible, computational modeling is critical for guiding the translation of the abstract design in Figure S1a into a genetic network.

As a starting point, we explored the genetic network design shown in Figure S1b. In this system, $A_{3OC12HSL}$ binds LasR and activates two different p(Las)-OR1 promoters that express *lasI* and *rhlI*. Since LasI catalyzes $A_{3OC12HSL}$ synthesis, $A_{3OC12HSL}$ is effectively autocatalytic. Similarly, since RhlI catalyzes synthesis of I_{C4HSL}, the $A_{3OC12HSL}$ activator also activates the I_{C4HSL} inhibitor. I_{C4HSL} binds RhlR and activates the p(Rhl) promoter, which expresses the λ phage CI repressor. CI represses the two p(Las)-OR1 promoters and thus inhibits further production of $A_{3OC12HSL}$ and I_{C4HSL}. CI also represses the p(Rhl)-OR1 promoter. We developed a detailed model of this system and confirmed through linear stability analysis that Turing instabilities could be achieved for certain parameter sets, and also confirmed through spatial simulations that patterns could form (6).

We then proceeded to consider design modifications that could potentially result in more robust patterning. One of the overall design goals was to create a network enriched for Turing instabilities but simple enough to physically construct and tune. In order to increase the chances of finding parameter sets with Turing instabilities without making the system much more complex, we developed code to perform stability analysis on random parameter sets for different design variations. As shown in Figure S2a, these alternative implementations had CI OR1 binding domains in different combinations of promoters, and some expressed a $A_{3OC12HSL}$ degrading acylase from the p(Rhl) promoter (7). Equations 1-27 were used to model the design variations, and kinetic rates were chosen according to Tables S1-S3. This model explicitly captures production and decay of mRNA, production and decay of proteins, and binding and dissociation of AHL and R-proteins. However, quasi steady state approximations were used for protein-DNA interactions. As found by other synthetic biology studies (8), detailed models of this nature can be important for capturing delays that impact system function.

www.pnas.org/cgi/doi/10.1073/pnas.1720770115

$$\frac{\partial mrnalasr}{\partial t} = k_{XSCRIBE\_LASR} * PCOPY * hill\_ci\_lasr - k_{DEC\_MRNA} * mrnalasr \quad [1]$$

$$\frac{\partial mrnarhli}{\partial t} = k_{XSCRIBE\_QSCLAS1} * PCOPY * hill\_activ\_qsclas1 * hill\_ci\_qsclas1 - k_{DEC\_MRNA} * mrnarhli \quad [2]$$

$$\frac{\partial lasr}{\partial t} = k_{XLATE\_LASR} * mrnalasr - k_{BIND\_LASR\_A} * lasr * A + k_{DIS\_LASR\_A} * lasr\_A - k_{DEC\_LASR} * lasr \quad [3]$$

$$\frac{\partial rhli}{\partial t} = k_{XLATE\_RHLI} * mrnarhli - k_{DEC\_RHLI} * rhli \quad [4]$$

$$\frac{\partial lasr\_A}{\partial t} = k_{BIND\_LASR\_A} * lasr * A - k_{DIS\_LASR\_A} * lasr\_A - k_{DEC\_LASR\_A} * lasr\_A \quad [5]$$

$$\frac{\partial A}{\partial t} = k_{SYNTH\_A} * lasi - k_{BIND\_LASR\_A} * lasr * A + k_{DIS\_LASR\_A} * lasr\_A - k_{BIND\_RHLR\_A} * rhlr * A + k_{DIS\_RHLR\_A} * rhlr\_A - k_{BIND\_ACYLASE} * acylase * A - k_{DEC\_A} * A + k_{DIFFUSE\_A} * \nabla^2 A \quad [6]$$

$$\frac{\partial I}{\partial t} = k_{SYNTH\_I} * rhli - k_{BIND\_RHLR\_I} * rhlr * I + k_{DIS\_RHLR\_I} * rhlr\_I - k_{DEC\_I} * I + k_{DIFFUSE\_I} \nabla^2 I \quad [7]$$

$$\frac{\partial mrnarhlr}{\partial t} = k_{XSCRIBE\_RHLR} * PCOPY * hill\_ci\_rhlr - k_{DEC\_MRNA} * mrnarhlr \quad [8]$$

$$\frac{\partial mrnaci}{\partial t} = k_{XSCRIBE\_QSCRHL} * PCOPY * hill\_activ\_qscrhl * hill\_ci\_qscrhl - k_{DEC\_MRNA} * mrnaci \quad [9]$$

$$\frac{\partial rhlr}{\partial t} = k_{XLATE\_RHLR} * mrnarhlr$$

$$
\begin{aligned}
&- k_{BIND\_RHLR\_I} * rhlr * I \\
&+ k_{DIS\_RHLR\_I} * rhlr\_I \\
&- k_{BIND\_RHLR\_A} * rhlr * A \\
&+ k_{DIS\_RHLR\_A} * rhlr\_A \\
&- k_{DEC\_RHLR} * rhlr
\end{aligned} \quad [10]
$$

$$
\begin{aligned}
\frac{\partial ci}{\partial t} &= k_{XLATE\_CI} * mrnaci \\
&- k_{DEC\_CI} * ci
\end{aligned} \quad [11]
$$

$$
\begin{aligned}
\frac{\partial rhlr\_I}{\partial t} &= k_{BIND\_RHLR\_I} * rhlr * I \\
&- k_{DIS\_RHLR\_I} * rhlr\_I \\
&- k_{DEC\_RHLR\_I} * rhlr\_I
\end{aligned} \quad [12]
$$

$$
\begin{aligned}
\frac{\partial mrnalasi}{\partial t} &= k_{XSCRIBE\_QSCLAS2} * PCOPY * hill\_activ\_qsclas2 * hill\_ci\_qsclas2 \\
&- k_{DEC\_MRNA} * mrnalasi
\end{aligned} \quad [13]
$$

$$
\begin{aligned}
\frac{\partial lasi}{\partial t} &= k_{XLATE\_LASI} * mrnalasi \\
&- k_{DEC\_LASI} * lasi
\end{aligned} \quad [14]
$$

$$
\begin{aligned}
\frac{\partial mrnaacylase}{\partial t} &= k_{XSCRIBE\_QSCRHL2} * PCOPY * hill\_activ\_qscrhl2 * hill\_ci\_qscrhl2 \\
&- k_{DEC\_MRNA} * mrnacylase
\end{aligned} \quad [15]
$$

$$
\begin{aligned}
\frac{\partial acylase}{\partial t} &= k_{XLATE\_ACYLASE} * mrnaacylase \\
&- k_{DEC\_acylase} * acylase
\end{aligned} \quad [16]
$$

$$
\begin{aligned}
\frac{\partial rhlr\_A}{\partial t} &= k_{BIND\_RHLR\_A} * rhlr * A \\
&- k_{DIS\_RHLR\_A} * rhlr\_A
\end{aligned} \quad [17]
$$

$$
hill\_ci\_lasr = 1 - \frac{ci^2}{ci^2 + k^2_{HALFMAX\_CI\_LASR}} \quad [18]
$$

$$
hill\_ci\_rhlr = 1 - \frac{ci^2}{ci^2 + k^2_{HALFMAX\_CI\_RHLR}} \quad [19]
$$

$$
hill\_activ\_qsclas1 = \frac{lasr\_A^2}{lasr\_A^2 + k^2_{HALFMAX\_LAS}} + k_{BASAL\_QSCLAS1} \quad [20]
$$

$$
hill\_ci\_qsclas1 = 1 - \frac{ci^2}{ci^2 + k^2_{HALFMAX\_CI\_QSCLAS1}} \quad [21]
$$

$$
hill\_activ\_qscrhl = \frac{rhlr\_I^2}{rhlr\_I^2 + k^2_{HALFMAX\_RHL}} + k_{BASAL\_QSCRHL} \quad [22]
$$

$$
hill\_activ\_qscrhl2 = \frac{rhlr\_I^2}{rhlr\_I^2 + k^2_{HALFMAX\_RHL2}} + k_{BASAL\_QSCRHL2} \quad [23]
$$

$$
hill\_ci\_qscrhl = 1 - \frac{ci^2}{ci^2 + k^2_{HALFMAX\_CI\_QSCRHL}} \quad [24]
$$

Table S1. Kinetic constants used for exploring design variations depicted in Figure S2a. Las promoter 1 is the promoter expressing *rhlI*, while Las promoter 2 refers to a separate Las promoter expressing *lasI*. Rhl promoter 1 is the promoter expressing *cI*, while Rhl promoter 2 refers to a separate Rhl promoter expressing *acylase*. $RAND(a,b)$ is a number randomly selected from the uniform interval [a,b], and bit_n is the n^{th} bit of the binary representation of the network number. Tables S2-S3 contain the rest of the parameters for this system.

$k_{XSCRIBE\_RHLR}$	transcription rate of *rhlR*	0.025 μM·hs^{-1}
$k_{XSCRIBE\_LASR}$	transcription rate of *lasR*	0.025 μM·hs^{-1}
$k_{XSCRIBE\_QSCRHL}$	Rhl promoter transcription rate	0.025 μM·hs^{-1}
$k_{XSCRIBE\_QSCLAS1}$	activated Las promoter 1 transcription rate	0.025 μM·hs^{-1}
$k_{XSCRIBE\_QSCLAS2}$	activated Las promoter 2 transcription rate	0.025 μM·hs^{-1}
k_{BASAL_QSCRHL}	basal transcription rate for Rhl promoter 1	0.001 μM·hs^{-1}
$k_{BASAL\_QSCRHL2}$	basal transcription rate for Rhl promoter 2	0.001 μM·hs^{-1}
$k_{BASAL\_QSCLAS1}$	basal transcription rate for Las promoter 1	0.001 μM·hs^{-1}
$k_{BASAL\_QSCLAS2}$	basal transcription rate for Las promoter 2	0.001 μM·hs^{-1}
k_{XLATE_RHLR}	translation rate of RhlR	$RAND(0.25,25)$ hs^{-1}
k_{XLATE_LASR}	translation rate of LasR	$RAND(0.25,25)$ hs^{-1}
k_{XLATE_CI}	translation rate of CI	$RAND(0.25,25)$ hs^{-1}
k_{XLATE_LASI}	translation rate of LasI	$RAND(0.25,25)$ hs^{-1}
k_{XLATE_RHLI}	translation rate of RhlR	$RAND(0.25,25)$ hs^{-1}
$k_{XLATE\_ACYLASE}$	translation rate of acylase	$bit_6 \cdot RAND(0.25,25)$ hs^{-1}
$k_{HALFMAX\_RHL}$	Concentration of RhlR/I complex giving half-maximal Rhl promoter 1 activation	1 μM
$k_{HALFMAX\_RHL2}$	Concentration of RhlR/I complex giving half-maximal Rhl promoter 2 activation	1 μM
$k_{HALFMAX\_LAS}$	Concentration of LasR/A complex giving half-maximal Las promoter activation	0.01 μM

$$hill\_ci\_qscrhl2 = 1 - \frac{ci^2}{ci^2 + k^2_{HALFMAX\_CI\_QSCRHL2}} \quad [25]$$

$$hill\_activ\_qsclas2 = \frac{lasr\_A^2}{lasr\_A^2 + k^2_{HALFMAX\_LAS}} + k_{BASAL\_QSCLAS2} \quad [26]$$

$$hill\_ci\_qsclas2 = 1 - \frac{ci^2}{ci^2 + k^2_{HALFMAX\_CI\_QSCLAS2}} \quad [27]$$

In the simulations, each different implementation corresponded to a certain network number. A promoter contained an OR1 domain if the corresponding bit in the binary representation of the network number was a 1 (Figure S2a). Likewise, acylase was expressed only if bit_6 of the binary representation of the network number was 1. For example, $56_{10} = 0111000_2$, so Network 56 has an OR1 site in the p(Las)-OR1 promoters expressing LasI and RhlI and in the promoter expressing RhlR since bit_3, bit_4, and bit_5 are all 1. Figure S2b shows the number of parameter sets with Turing instabilities found for each different network. Although Network 106 was most enriched for Turing instabilities, this network requires acylase expression. Networks 56 and 57, depicted in Figure S1c, do not require acylase expression and were ultimately chosen instead for the sake of simplicity.

Having chosen a network architecture, we then investigated the role of key parameters in determining the existance of Turing instabilities(6). Of particular importance, we found that sensitive responses of the p(Las)-OR1 promoter were important for achieving Turing instabilities. Since the results suggested that the Hill coefficient of p(Las) activation must be greater than 1 for pattern formation, we

Table S2. Kinetic constants used for exploring design variations, continued from Table S1. The remaining constants are in Table S3.

$k_{HALFMAX\_CI\_QSCLAS1}$	Concentration of CI giving half-maximal Las promoter 1 repression	$RAND(0.007796, 0.7796)/bit_5$ μM
$k_{HALFMAX\_CI\_QSCLAS2}$	Concentration of CI giving half-maximal Las promoter 2 repression	$RAND(0.007796, 0.7796)/bit_4$ μM
$k_{HALFMAX\_CI\_QSCRHL}$	Concentration of CI giving half-maximal Rhl promoter 1 repression	$RAND(0.007796, 0.7796)/bit_3$ μM
$k_{HALFMAX\_CI\_QSCRHL2}$	Concentration of CI giving half-maximal Rhl promoter 2 repression	$RAND(0.007796, 0.7796)/bit_0$ μM
$k_{HALFMAX\_CI\_RHLR}$	Concentration of CI giving half-maximal repression of RhlR	$RAND(0.007796, 0.7796)/bit_3$ μM
$k_{HALFMAX\_CI\_LASR}$	Concentration of CI giving half-maximal repression of LasR	$RAND(0.007796, 0.7796)/bit_1$ μM
k_{DEC_RHLR}	decay rate of RhlR	0.029 hs^{-1}
k_{DEC_LASR}	decay rate of LasR	0.029 hs^{-1}
k_{DEC_CI}	decay rate of CI	0.116 hs^{-1}
k_{DEC_LASI}	decay rate of LasI	0.116 hs^{-1}
k_{DEC_RHLI}	decay rate of RhlI	0.116 hs^{-1}
$k_{DEC\_ACYLASE}$	decay rate of acylase	0.116 hs^{-1}
k_{DEC_MRNA}	decay rate of mRNA	1.16 hs^{-1}
k_{DEC_I}	decay rate of I_{C4HSL}	0.002 hs^{-1}
k_{DEC_A}	decay rate of $A_{3OC12HSL}$	0.002 hs^{-1}
$k_{DEC\_RHLR\_I}$	decay rate of RhlR/I_{C4HSL} complex	0.029 hs^{-1}
$k_{DEC\_LASR\_A}$	decay rate of LasR/$A_{3OC12HSL}$ complex	0.029 hs^{-1}

Table S3. Kinetic constants used for exploring design variations, continued from Tables S1-S2.

D_I	I_{C4HSL} diffusion rate	0.003 gridpoints$^2 \cdot hs^{-1}$
D_A	$A_{3OC12HSL}$ diffusion rate	0.0003 gridpoints$^2 \cdot hs^{-1}$
$k_{BIND\_RHLR\_I}$	binding rate of RhlR and I_{C4HSL}	0.1 $\mu M^{-1} hs^{-1}$
$k_{BIND\_RHLR\_A}$	binding rate of RhlR and $A_{3OC12HSL}$	0.1 $\mu M^{-1} hs^{-1}$
$k_{BIND\_LASR\_A}$	binding rate of LasR and $A_{3OC12HSL}$	0.1 $\mu M^{-1} hs^{-1}$
$k_{BIND\_ACYLASE}$	destruction rate of $A_{3OC12HSL}$ by acylase	0.0023 $\mu M^{-1} hs^{-1}$
$k_{DIS\_RHLR\_I}$	dissociation of RhlR/I_{C4HSL} complex	1 hs^{-1}
$k_{DIS\_RHLR\_A}$	dissociation of RhlR/$A_{3OC12HSL}$ complex	1 hs^{-1}
$k_{DIS\_LASR\_A}$	dissociation of LasR/$A_{3OC12HSL}$ complex	1 hs^{-1}
k_{SYNTH_I}	synthesis rate of I_{C4HSL} (9)	0.5 hs^{-1}
k_{SYNTH_A}	synthesis rate of $A_{3OC12HSL}$ (9)	0.5 hs^{-1}
PCOPY	Plasmid copy number	10

considered placing LasR under the control of a p(Las)-OR1 promoter. Starting even with a p(Las) promoter that responds hyperbolically to $A_{3OC12HSL}$ (Hill coefficient of 1), an ultrasensitive reporter response can be engineered by placing *lasR* under control of the p(Las) promoter. This can be demonstrated as follows. Suppose a p(Las) promoter regulates both LasR and a reporter. It can be assumed that the steady state reporter level is proportional to the steady state LasR level. The differential equation for LasR is given in Equation 28.

$$\frac{\partial L}{\partial t} = \frac{\alpha_0 + \alpha_1 (KSL)^m}{1 + (KSL)^m} - dL \quad [28]$$

Here, α_0 is the basal expression rate and α_1 is the maximum rate of expression from the activated promoter. K is the inverse of the level of $A_{3OC12HSL}$/LasR that gives rise to promoter expression at a rate that is halfway between basal and maximal expression. S is the $A_{3OC12HSL}$ signal, d is the LasR decay rate, and m is the Hill coefficient of p(Las) activation by $A_{3OC12HSL}$/LasR.

One commonly used metric for measuring sensitivity is the cooperativity index R_C (10, 11), defined for this system as the ratio of S necessary for 90% promoter activation to S necessary for 10% promoter activation. This corresponds to Equations 29-33.

$$L_{90} = 0.1\alpha_0 + 0.9\alpha_1 \quad [29]$$

$$L_{10} = 0.9\alpha_0 + 0.1\alpha_1 \quad [30]$$

$$S_{90} = \frac{1}{KL_{90}} \sqrt[m]{\frac{dL_{90} - \alpha_0}{\alpha_1 - dL_{90}}} \quad [31]$$

$$S_{10} = \frac{1}{KL_{10}} \sqrt[m]{\frac{dL_{10} - \alpha_0}{\alpha_1 - dL_{10}}} \quad [32]$$

$$R_C = \frac{S_{90}}{S_{10}} \quad [33]$$

For a p(Las) promoter that has a Hill coefficient of 1 when LasR is constitutively expressed, L is given by Equation 34, and the cooperativity index is given by Equation 35. For $\alpha_1 \gg \alpha_0$, the cooperativity index is almost 9. Although Equation 34 is not a Hill equation, a cooperativity index of 9 would correspond to a Hill coefficient of 2. Figure S3 illustrates the enhancement in sensitivity gained by placing LasR under control of p(Las). Reporter output versus $A_{3OC12HSL}$ is shown for constitutive LasR expression and for LasR under control of p(Las) using the following parameter set: $\alpha_0 = 0.01$, $\alpha_1 = 1$, $K = 0.5$, $d = 1$, $m = 1$.

$$L = \frac{\alpha_1 KS - d + \sqrt{(\alpha_1 KS - d)^2 + 4dK\alpha_0 S}}{2dKS} \quad [34]$$

$$R_C = \frac{81(9\alpha_0 + \alpha_1)}{\alpha_0 + 9\alpha_1} \quad [35]$$

Equation 34 was used to represent reporter concentration for the case of LasR under control of p(Las). This was done because the steady state reporter level is proportional to the level of LasR, as mentioned previously. For the case of constitutive LasR expression, the Equation 36 was used to represent steady state reporter concentration.

$$reporter_{LasRconstit} = \frac{\alpha_0 + \alpha_1 \frac{K\alpha_1 S}{d}^m}{d(1 + \frac{K\alpha_1 S}{d}^m)} \quad [36]$$

Having modified our design to incorporate positive feedback on LasR, we arrived at the final design shown in Fig. S1c and Fig. 1 of the main text. We then proceeded to construct the system in a modular fashion.

2. System construction

Each genetic part for our system was characterized prior to assembly into devices. Table S4 describes provides references to characterizations of the constructs used for this study. For many of these components, standardized BioBrick components are available. Devices were assembled from these genetic parts in a modular fashion (6). We now describe the DNA constructs for our final system.

Table S4. Sources of genetic parts.

Genetic Part	References
lasI(LVA)	(6, 12), BBa_C0078
rhlI	(6, 12), BBa_C0170
lasR	(6, 12), BBa_C0179
rhlR-I124F	(6)
cI(LVA)	(13–15), BBa_C0051
lacI	BBa_I732100
GFP(LVA)	(16), BBa_K082003
DsRed-Express	Clontech
$\lambda_{P(R-O1)}$	(6)
pLas-OR1	(6), BBa_I14016
pRhl-LacO	this study

A. Plasmid Construction. Our patterning circuit design was implemented by partitioning the system into two plasmids, namely pFNK-512 (Fig. S4a) and pFNK-804-LacO-LacI (Fig. S4b), corresponding to the upper and lower parts of the circuit diagram in Fig. 1b of the main text. pFNK-512 was constructed by inserting two identical divergent copies of the hybrid promoter $P_{Las-OR1}$ as well as the genes *lasI(LVA)*, *rhlI*, *dsRed*, and *lasR* into the pPROTet.E vector (ColE1 ori and Cm resistance, Clontech). The promoter $P_{Las-OR1}$ was constructed by fusing a mutant CI binding domain O_{R1}-mut4 (17) to a wildtype Las promoter in *P. aeruginosa* (PAO1 strain) (6, 18). The hybrid promoter sequence is shown in Fig. S4g. This approach for constructing promoters that are activated by quorum sensing signals, yet repressed by repressors such as cI has been previously described (13). A Las regulatory gene *lasR* was placed downstream of one copy of the hybrid promoter. $A_{3OC12HSL}$ and I_{C4HSL} synthase genes *lasI(LVA)* and *rhlI* were inserted downstream of the other $P_{Las-OR1}$ promoter followed by a red fluorescence reporter gene *dsRed-exp* (from Clontech plasmid pDsRed-Exp). RBSII was used for all ribosome binding sites in this plasmid (17).

pFNK-804-LacO-LacI was constructed starting from the pPROLar.A vector (ColE1 ori and Kan resistance, Clontech) and integrating the promoters p_{LacIq}, $\lambda_{P(R-O1)}$, and $P_{Rhl-lacO}$ and the genes *lacI*, *rhlR*, *cI*, and *GFP(LVA)* (19). The constitutive promoter p_{LacIq}, ribosome binding site RBSII, and *lacI* gene were inserted into the vector for constitutive expression of LacI (17). A mutant *rhlR* (6) was placed under control of a CI-regulated promoter $\lambda_{P(R-O1)}$ and the ribosome binding site RBSH (6, 18, 19). The *rhlR* mutant, *RhlR-I124F* was selected by directed evolution for its response to lower concentrations of I_{C4HSL} than the wildtype (6). Hybrid promoter $P_{Rhl-lacO}$ was constructed by adding a LacO operator binding site to a wildtype RhlR promoter in *P. aeruginosa* (Fig. S4g). Genes *cI* and *GFP(LVA)* were placed under transcriptional control of the hybrid promoter $P_{Rhl-lacO}$. Ribosome binding sites RBSH and RBSII were used for *cI* and *GFP* respectively (17, 19).

Plasmid pFNK-806 (Fig. S4c) was derived from pFNK-804-LacO-LacI. It was constructed by replacing promoter $\lambda_{P(R-O1)}$ in pFNK-804-LacO-LacI with the constitutive promoter p_{LacIq}, and replacing the corresponding ribosome binding site RBSII with RBSG (17). This provided a plasmid without the inhibition of RhlR production by CI.

Plasmid pTOG-1 (Fig. S4d was created from toggle switch plasmid pIKE-107 (ColE1 ori and Amp resistance) (20). We inserted a red fluorescence gene *mCherry* into the original plasmid downstream of the *lacI* gene that is regulated by promoter $p_{LtetO-1}$. RBSII was used as the ribosome binding site for *mCherry* (17).

Plasmids pINV-5 and pASK-201 were used for the negative controls in Fig. 2b in the main text. The pINV-5 plasmid expresses *lacI* from the constitutive promoter p_{LacIq} and expresses *GFP(LVA)* from the LacI-regulated promoter p_{Lac} on a p15A plasmid with

kanamycin resistance (Fig. S4e) (21). Plasmid pASK-201 is identical to pINV-5 except that *gfp(lva)* was replaced by a red fluorescence gene *dsRed-Exp* (Fig. S4f).

All plasmids were constructed using standard molecular biology cloning techniques. Restriction enzymes were obtained from New England BioLabs Inc, and PCR primers were ordered from Integrated DNA Technologies, Inc.

3. Diffusion experiments and mathematical modeling

A requirement for Turing pattern formation is two morphogens that have distinct diffusion rates. Specifically, the activator species $A_{3OC12HSL}$ should diffuse more slowly than the inhibitor I_{C4HSL}. To quantify the difference between the diffusion rates, we performed dosage response experiments, solid-phase diffusion experiments, mathematical modeling, and parameter estimation.

AHL response threshold. To conduct the diffusion assays, we first needed to calibrate the morphogen response thresholds. We individually transformed plasmids pFNK202-qsc119 and pFNK503-qscrsaL into strain MG1655 to serve as reporter cells for I_{C4HSL} and $A_{3OC12HSL}$ respectively (12). pFNK202-qsc119 is a I_{C4HSL} reporter construct that expresses RhlR constitutively and expresses a GFP(LVA) reporter from the p(Rhl) promoter. pFNK503-qscrsaL is a $A_{3OC12HSL}$ reporter construct that expresses LasR constitutively and expresses a GFP(LVA) reporter from the p(Las) promoter (12). Reporter cells inoculated from overnight cultures were grown in M9 media for 3 hours and then induced with various levels of AHL for 6 hours. Single cell fluorescence data were subsequently collected using a Beckman Coulter Altra flow cytometer equipped with a 488-nm argon excitation laser and a 515-545 nm emission filter. Figure S5 shows the dosage response curves for I_{C4HSL} and $A_{3OC12HSL}$ receiver cells. The half activation thresholds are approximately 3×10^{-3} µM for $A_{3OC12HSL}$ and 3 µM for I_{C4HSL}. This information allows us to correlate fluorescence activation with AHL concentration in our solid-phase diffusion experiments.

Diffusion experiments. We performed solid-phase diffusion experiments in 2% M9 agar plates as described in Methods. Reporter cells picked from single colonies were cultured in liquid LB media overnight and diluted 1000:1 into fresh media the next day. When culture OD's reached $0.1 - 0.3$, cells were concentrated and resuspended in M9 media to final OD of 2.0. 1.5 mL of the concentrated cells were plated onto 80×15 mm M9 agar Petri dishes for the diffusion experiments. To correspond with the environmental conditions of our patterning experiments, plates with the cells were first incubated at 30 ^{o}C for 12 hours. Afterwards, 3 μL AHL droplets with an appropriate concentration (10 mM for I_{C4HSL}, and 0.01 mM for $A_{3OC12HSL}$) were added at the center of the plates for each type of reporter cell. We chose these concentrations based on the AHL's half activation thresholds so that the AHL's activate cells around the center but not close to the edge of the Petri dishes. Fluorescence images were taken at hours 0, 2.5, 5, and 8.75 using a Bio-rad Molecular Imager ChemiDoc XRS+ System. An XcitaBlue conversion screen was used for capturing GFP intensities.

Every image obtained from this experiment has a fluorescence radial gradient centered around the position where the AHL droplet was added. Figure S6a-b shows representative fluorescence intensity lines crossing the image centers for different time points for the two AHL diffusion experiments. The image exposure times for I_{C4HSL} and $A_{3OC12HSL}$ are 0.1 s and 0.2 s respectively. Raw images were processed to remove exposure bias in the field of view by background subtraction of reference frames.

We then conducted experiments to ensure that the diffusion of I_{C4HSL} and $A_{3OC12HSL}$ did not drastically change due to potential differences in biofilm characteristics over many hours of incubation. Specifically, the diffusion experiment was again carried out, varying the initial incubation time before AHL addition. Images were then captured following 0, 2.5, 5, and 8 hours of AHL exposure (Fig. S7).

Modeling and parameter estimation. To estimate experimental diffusion coefficients for the signaling species, we developed the following reaction-diffusion model:

$$\frac{\partial S}{\partial t} = D_s \nabla^2 S - \gamma_s S \quad [37]$$

$$\frac{\partial F}{\partial t} = \alpha_f N \frac{S}{K_s + S} - \gamma_f F \quad [38]$$

$$\frac{\partial N}{\partial t} = \alpha_n N(1 - N/N_l) \quad [39]$$

This model captures the behavior of the reporter cells harboring reporter constructs pFNK202-qsc119 and pFNK503-qscrsaL. In this model, S, F, and N refer to AHL concentration, fluorescence reporter concentration, and cell density respectively. γ_s and γ_f are the degradation rates for AHL and the fluorescence reporter, D_s is the AHL diffusion coefficient, K_s is the AHL half-activation threshold, α_f is the fluorescence reporter production rate and α_n is the cell growth rate. In this model, cell density is assumed to grow logistically (22).

According to our experimental setup, the initial conditions of the equations include $F(x,t)|_{t=0} = 0$, $N(x,t)|_{t=0} = N_0$ and $S(x,t)|_{t=0} = S_0 \mathrm{H}[x+x_0](1-\mathrm{H}[x-x_0])$, where $\mathrm{H}[x]$ is the Heaviside step function and x_0 is the radius of the initial AHL droplet. The signal's initial condition was chosen as above to simulate the localized addition of AHL droplets onto the plate. The boundary conditions of the system are $\partial S/\partial x|_{x=\pm 4} = 0$, $\partial F/\partial x|_{x=\pm 4} = 0$, and $\partial N/\partial x|_{x=\pm 4} = 0$. Since the fluorescence observed in our experiment consists of the fluorescence reporter and cell autofluorescence, the total fluorescence is indicated by $F_{total} = F + \beta_f N$.

From the literature (23), we use degradation rates of $\gamma_{s=c_{12}} = 0.002$ hr^{-1} for $\mathrm{A_{3OC12HSL}}$ and $\gamma_{s=c_4} = 0.02$ hr^{-1} for $\mathrm{I_{C4HSL}}$. The degradation rate of the fluorescent protein is $\gamma_f = 0.04$ hr^{-1}. We choose $\beta_f = 0.5$ for $\mathrm{I_{C4HSL}}$ (0.1 s exposure time) and $\beta_f = 1.0$ for $\mathrm{A_{3OC12HSL}}$ (0.2 s exposure time). From the dosage response experiment, we obtained half activation thresholds for the two AHLs of $K_{s=c_{12}} = 0.003$ μM and $K_{s=c_4} = 3$ μM. By parameter estimation using the fluorescence intensities of cells far away from the center in the model with the experimental setup, we obtained a cellular growth rate of $\alpha_n = 0.15$ hr^{-1} and saturation cell density of $N_l = 5.0$ ($N_0 = 1.0$). Then, by parameter estimation of the fluorescence wave profile over time, we estimate the diffusion coefficients to be $D_{c_{12}} = 0.003$ cm^2/hr for $\mathrm{A_{3OC12HSL}}$ and $D_{c_4} = 0.065$ cm^2/hr for $\mathrm{I_{C4HSL}}$. The corresponding simulation results are shown in Fig. S6c-d. These experiments suggest that the diffusion coefficient for the activator is approximately 21.6 fold slower than that of the inhibitor, qualitatively consistent with a previous study (24). One possible explanation for why the ratio of diffusion rates is higher than expected based on molecular weight differences alone is that the hydrophobic nature of $\mathrm{A_{3OC12HSL}}$ causes it to partition in the cell membrane, thus essentially slowing down its diffusion from cell to cell (24).

4. Signal Specificity and Competitive Inhibition

An initial design challenge was to identify sufficiently non-interacting cell-cell signaling systems. Our choice of harnessing the *Pseudomonas aeruginosa* Rhl and Las quorum sensing systems was based on the potential for achieving specific responses to two different signals in the same cell (3). In *P. aeruginosa*, $\mathrm{A_{3OC12HSL}}$ and $\mathrm{I_{C4HSL}}$ are the two signaling molecules of the Las and Rhl quorum sensing pathways: $\mathrm{A_{3OC12HSL}}$ and LasR are responsible for activation of the $\mathrm{p_{Las}}$ promoter while $\mathrm{I_{C4HSL}}$ and RhlR regulate the $\mathrm{p_{Rhl}}$ promoter. Many promoters in *P. aeruginosa* are quorum sensing controlled and exhibit varying degrees of specificity to $\mathrm{A_{3OC12HSL}}$ and/or $\mathrm{I_{C4HSL}}$. Therefore, we first identified a Rhl promoter, the rhlAB promoter, that specifically responded to $\mathrm{I_{C4HSL}}$/RhlR and a Las promoter, the rsaL promoter, that specifically responded $\mathrm{A_{3OC12HSL}}$/LasR (6). As an example demonstration of signal specificity, we used *E. coli* cells that harbor a plasmid (pFNK202-qsc119) with constitutively expressed RhlR and a $\mathrm{p_{Rhl}}$ promoter regulating a GFP(LVA) reporter (12). We performed crosstalk experiments by inducing the engineered cells with different combinations of the AHLs. Our experiments along with previous results (12) confirm that the Rhl pathway is activated by $\mathrm{I_{C4HSL}}$ but not by $\mathrm{A_{3OC12HSL}}$ in the presence of RhlR (Fig. S8a).

In spite of the specific response of our Las and Rhl promoters to $\mathrm{A_{3OC12HSL}}$/LasR and $\mathrm{I_{C4HSL}}$/RhlR, an important interaction still exists. Namely, $\mathrm{A_{3OC12HSL}}$ can competitively bind RhlR. To explore the effects of this competitive binding, we induced *rhl* receiver cells with different levels of $\mathrm{A_{3OC12HSL}}$ (0 to 30 μM) while $\mathrm{I_{C4HSL}}$ was kept high (3 μM). Figure S8b shows that the fluorescence level of single cells monotonically decreases with $\mathrm{A_{3OC12HSL}}$. This experiment suggests that $\mathrm{A_{3OC12HSL}}$ binds RhlR, the regulatory protein for $\mathrm{I_{C4HSL}}$, but the corresponding complex does not activate the promoter $\mathrm{p_{Rhl}}$. The competitive binding of $\mathrm{A_{3OC12HSL}}$ to RhlR thus reduces RhlR/$\mathrm{I_{C4HSL}}$ complex formation and, as a result, inhibits $\mathrm{p_{Rhl}}$ activation from $\mathrm{I_{C4HSL}}$. In wildtype *P. aeruginosa*, this competitive inhibition may provide an alternative mechanism for temporal control of the activation of transcription factors by delaying the induction

of genes regulated by the *rhl* quorum sensing pathway (25). In our system, this inhibition attenuates GFP in the red fluorescent activator regions.

5. Control Experiments and Pattern Characteristics

To demonstrate that our system exhibits stochastic Turing patterns, we showed that our patterns are not a result of the outward growth of clusters of differentially colored cells. For this we first assayed the phenotypic behavior of lawns of cells that express fluorescent proteins constitutively. As shown in Fig. 2b, when red and green fluorescent cells are grown separately or together, uniform fluorescent fields develop. The difference between these control experiments and the emergent patterns is illustrated clearly in the red/green fluorescence density plots (Fig. 2c). We further tested additional ratios of constitutively fluorescent green and red cells and again observed relatively uniform fields of fluorescence (Fig. S9). These experiments demonstrate that, in our experimental setup, neither cell growth nor initial spatial heterogeneity of cell density give rise to the large scale spatial patterns observed with the Turing cells.

Next, we tested whether observable patterns would emerge if individual cells autonomously made cell-fate decisions at some point after plating. This would indicate that our system is not, in fact, generating emergent patterns. To address this question, we performed another experiment with cells that harbor independent bistable green/red toggle switches (Fig. S10a) (20). For these switches, which are essentially net positive feedback loops, IPTG induction results in expression of TetR/GFP, aTc induction results in expression of LacI/RFP, and absence of inducer results in a 'memory' of the cells' most recent state (at 30^{o}C) (20). Co-induction with both inducers gives rise to co-expression of all proteins; subsequent simultaneous removal of the inducers causes each cell to make an independent quasi-random decision and enter one of the two stable states. To explore whether such an independent decision-making process results in global pattern formation, we induced toggle cells with 3 μM IPTG and 0.3 μM aTc in liquid culture for 5 hours. Flow cytometry analysis confirmed that after this initial incubation period, all cells in the population had roughly the same red/green fluorescence levels (Fig. S10b). Co-induced cells were then plated onto Petri dishes lacking inducers (bistability condition) using the same technique as the experiments above. The fluorescence fields after 24 hour incubation at 30 ^{o}C were uniform, showing no emergence of patterns (Fig. S10d-f). However, flow cytometry analysis of cells scraped from the plate after 24 hours revealed that the initially homogeneous cell population had bifurcated almost completely into two subpopulations, one with high GFP expression and the other with high RFP expression (Fig. S10c). The toggle switch cell lawn maintained spatial homogeneity but individual cells settled into one of the two states, suggesting that this autonomous quasi-random fate decision by individual cells does not lead to global spatial patterning.

Next we explored the robustness and structural stability of our results: specifically, whether and how changes in the levels of localized interactions lead to different global outcomes. In our system, IPTG can be used to modulate the inhibitory efficiency of I_{C4HSL} in individual cells by affecting CI expression from $P_{Rhl-lacO}$, up to the threshold of toxicity. Our data show that mean GFP levels increase sigmoidally with inducer concentration while the overall area of red spots decreases (Fig. 3b-c), correlating well with the results from our mathematical model (Fig. 3d-g). To quantify changes in the spatial characteristics of the patterns in response to different IPTG concentrations, we define a *collectivity metric* as follows:

$$\Theta = \sum_{i,j=1}^{M} \sigma_{i,j}, \quad \text{where } \sigma_{i,j} = \begin{cases} 1 & \text{if pixels } i \text{ and } j \text{ are in the same red spot} \\ 0 & \text{otherwise} \end{cases}$$

where M is the total number of pixels in the image. Fig. 3b shows that in our experiments, the collectivity metric decreases approximately 9 fold as a function of IPTG, indicating that an increase in the inhibitory effect of I_{C4HSL} in each individual cell results in reduced overall global clustering. Moran's I (26) is also plotted to illustrate how the spatial autocorrelation of an image decreases with IPTG (Fig. 3b, inset), qualitatively consistent with the analysis of our simulated patterns (Supplementary Information, Fig. S11).Additionally, spots become smaller due to IPTG induction as is visible in the microscope images in Fig. 3a.

We performed a 32-hour experiment to gain a better understanding of the dynamics of pattern emergence. A lawn of cells was prepared as described in Methods, placed in a microscope chamber and incubated at 30 ^{o}C. Fluorescence images of the same region

were captured once every 30 minutes. Figure S12 shows images at 4 hour intervals (0-, 4-, 8-, 12-, 16-, 20-, 24-, 28-, and 32-hour). There is no fluorescence initially until hour 16 when tiny spots emerge. These tiny spots grow quickly and new spots continue appearing and growing during the following few hours. By hour 24, spots have emerged with typical sizes much larger than that of a single cell. The spot pattern remains roughly the same from hour 24 to hour 32. However, as our experimental system is fundamentally a dissipative system, and we do not feed fresh nutrients, an eventual breakdown is inevitable.

We can also extract the characteristic scale of the pattern. To do this we found the centroid points of each clump of activator. We then created a histogram of distances to to nearest neighboring centroids Figure S13f. From this plot we found that the average separation of clumps is 45 ± 11 μm. Additionally we can extract the distribution for sizes of the spots. We found the the average radius of the clump is 14 μm.

6. Moran's I

Moran's I was developed to measure spatial autocorrelation and indicates whether adjacent observations of the same phenomenon are correlated. Moran's I was proposed as follows (26)

$$I = \frac{N}{\sum_{i=1}^{N}\sum_{j=1}^{N} w_{ij}} \frac{\sum_{i=1}^{N}\sum_{j=1}^{N} w_{ij}(x_i - \bar{x})(x_j - \bar{x})}{\sum_{i=1}^{N}(x_i - \bar{x})^2} \quad [40]$$

where N is the total number of pixels, x is the variable of interest (red fluorescence level here), $\bar{x}$ is the mean of x, and w_{ij} a weight matrix of pixels. We employ a simple form of the weight matrix as follows: $w_{ij} = 1$ if two pixels are directly adjacent and $w_{ij} = 0$ otherwise. Moran's I values typically range from $+1$, representing complete positive spatial autocorrelation, to -1, corresponding to complete negative spatial autocorrelation.

7. A deterministic reaction-diffusion model

The goal of this section is to see if a deterministic model can reproduce the principal features of the observed pattern. To this end, we use order of magnitude estimates for parameters. Our synthetic system consists of biochemical reactions involving promoters, mRNA, and proteins as well as signal diffusion, with rate constants that span multiple time-scales. To obtain a manageable model, we make the following commonly used simplifying assumptions:

- Operator states of a promoter fluctuate much faster than protein degradation rates.
- mRNA half-life is much shorter than protein half-life.

These assumptions allow us to eliminate operator fluctuation and mRNA kinetics and model the system at the communication signals and protein levels as

$$\frac{\partial U}{\partial t} = \alpha_u I_u - \gamma_u U + D_u \nabla^2 U \quad [41]$$

$$\frac{\partial V}{\partial t} = \alpha_v I_v - \gamma_v V + D_v \nabla^2 V \quad [42]$$

$$\frac{\partial I_u}{\partial t} = \alpha_{iu} F_1(X_1, C) - \gamma_{iu} I_u \quad [43]$$

$$\frac{\partial I_v}{\partial t} = \alpha_{iv} F_1(X_1, C) - \gamma_{iv} I_v \quad [44]$$

$$\frac{\partial C}{\partial t} = \alpha_c F_2(X_2, L) - \gamma_c C \quad [45]$$

where U and V are the concentrations of the two diffusible morphogens $A_{3OC12HSL}$ and I_{C4HSL}, I_u and I_v are the concentrations of corresponding AHL synthases, and C refers to CI.

We model the hybrid promoters using the following Hill functions:

$$F_1(X_1,C) = \frac{[1+f_1(\frac{X_1}{K_{d1}})^{\theta_1}][1+f_2^{-1}(\frac{C}{K_{d2}})^{\theta_2}]}{[1+(\frac{X_1}{K_{d1}})^{\theta_1}][1+(\frac{C}{K_{d2}})^{\theta_2}]} \quad [46]$$

$$F_2(X_2,L) = \frac{[1+f_3(\frac{X_2}{K_{d3}})^{\theta_3}][1+f_4^{-1}(\frac{L}{K_{d4}})^{\theta_4}]}{[1+(\frac{X_2}{K_{d3}})^{\theta_3}][1+(\frac{L}{K_{d4}})^{\theta_4}]} \quad [47]$$

where $F_1(X_1,C)$ and $F_2(X_2,L)$ are the production rates of the promoters $P_{Las-OR1}$and $P_{Rhl-lacO}$, X_1 and X_2 are the LasR-$A_{3OC12HSL}$ complex and the RhlR-I_{C4HSL} complex respectively, and L is the concentration of unbound LacI protein. We use the definitions

$$X_1 = R_u U \quad [48]$$

$$X_2 = \frac{R_v V}{(1+U/K_{c3})} \quad [49]$$

$$L = \lambda_l \left(\frac{1+f_6^{-1}(I/K_{d6})^{\theta_6}}{1+(I/K_{d6})^{\theta_6}} \right) \quad [50]$$

where I is the IPTG concentration, R_u and R_v are the regulatory proteins LasR and RhlR:

$$R_u = \lambda_u I_u \quad [51]$$

$$R_v = \lambda_v \left(\frac{1+f_5^{-1}(C/K_{d5})^{\theta_5}}{1+(C/K_{d5})^{\theta_5}} \right) \quad [52]$$

A summary of the variables used in our model is available in Table S5 and definitions of the rate constants in Tables S6-S7. Hill functions employed in this model have a shared form of $Y = \frac{1+f(X/K)^{\theta}}{1+(X/K)^{\theta}}$, where X and Y correspond to the input and output of the function, K is the dissociation constant, θ is the Hill coefficient and f is the fold change of Y upon full induction by X. For the measured values of $\frac{D_v}{D_u} \approx 21.6$, deterministic patterns do not arise. We artificially increased this ratio to 100 and found that patterns did form with similar attributes to the observed pattern, but also were more regular than the patterns observed in our experiment.

To study patterning using our model, we divide a cellular lawn into a mesoscopic $M \times M$ grid ($M = 64$ in our simulation). As is common for deterministic Turing simulations, we introduce small variation into the initial concentrations of the molecules for initial symmetry breaking. All the variables (species) were initially assigned low values (random values obeying a Gaussian distribution that has a mean of 1.0 and a variance of 0.05) to approximate the initial condition in our experimental setup. We numerically integrate the partial differential equations over time to simulate spontaneous pattern formation. We also perform numerical simulations with a range of IPTG concentrations (from 10^{-6} to 10^{-2} M) to explore modulation of pattern formation. Sizes of simulated patterns are determined in terms of relative fluorescence intensities rather than absolute values to match our image processing procedures for the experimental data.

8. A stochastic model

When the diffusion rate ratio is high enough to support pattern formation, our deterministic model correlates well with several characteristics of our experimental observations including pattern modulation by inducer IPTG. However, the deterministically simulated patterns have a uniform distribution of spot size, fluorescence intensity, and separation, whereas the experimental results display large variability in these attributes. We developed a stochastic spatiotemporal model to improve the correlation with the experimental observations. The patterning process is modeled with exactly the same biochemical reactions used in our deterministic model but simulated stochastically using an efficient tau-leaping stochastic algorithm(27, 28). To speed up this large scale spatiotemporal simulation, we employ a hybrid technique where all intracellular chemical reactions are stochastic but signal diffusion is deterministic since the diffusion time scales are typically much faster than the intracellular reactions considered in our model.

To illustrate the behavior of each species in our pattern formation system (Table S5), we performed a spatial stochastic simulation using the parameters depicted in Tables S6-S7. The top of Figure S16 shows $A_{3OC12HSL}$ and I_{C4HSL} patterns produced in our stochastic simulation using the parameters given in tables Tables S6-S7. The red line indicates the location of the cross-section used for all other

dynamic variables. The bottom of Figure S16 shows cross-sectional slices of variables U ($A_{3OC12HSL}$), V (I_{C4HSL}), I_u (LasI), I_v (RhlI), C (CI), R_u (LasR), R_v (RhlR), L (free LacI), X_1 (LasR-$A_{3OC12HSL}$ complex), and X_2 (RhlR-I_{C4HSL} complex).

As seen in Figure S16, the concentrations of LasI, RhlI, and LasR are proportional to the $A_{3OC12HSL}$ activator. This is due to the fact that these proteins are expressed from the $A_{3OC12HSL}$ activated $P_{Las-OR1}$ promoter. Likewise, the LasR-$A_{3OC12HSL}$ complex is directly proportional to $A_{3OC12HSL}$ concentrations. In addition, since RhlI catalyzes I_{C4HSL} synthesis, I_{C4HSL} is also directly proportional to $A_{3OC12HSL}$ concentrations. However, since I_{C4HSL} diffuses faster than $A_{3OC12HSL}$, relatively high concentrations of I_{C4HSL} are also found in between the $A_{3OC12HSL}$ activation domains.

Interestingly, the RhlR-I_{C4HSL} complex is inversely proportional to $A_{3OC12HSL}$. In regions of high $A_{3OC12HSL}$, $A_{3OC12HSL}$ competitively binds RhlR, lowering the concentration of the RhlR-I_{C4HSL} complex. However, as mentioned, I_{C4HSL} concentrations remain relatively high outside of the $A_{3OC12HSL}$ activation domains. Thus, RhlR-I_{C4HSL} is highest in between the activation domains. Collectively, this behavior results in green fluorescence (following the RhlR-I_{C4HSL} complex concentration) surrounding red fluorescent activation domains (following the LasR-$A_{3OC12HSL}$ complex concentration).

To characterize the stochastic simulation we calculated the distribution of spot sizes and spacing. We binarized the simulation data shown in Figure S17 and determined locations of the centroids of spots and the areas of the spots. The spacing is calculated by finding the distance to the nearest neighboring centroid. The distribution of spot sizes and spacing is shown in Figure S18. As the IPTG concentration is increased spot sizes decrease and have more variance. Similarly the spacing between spots decreases as the IPTG concentrations is increased.

To determine the sensitivity of the stochastic model to the parameters chosen, we individually varied parameters from half their nominal value to 1.5x their nominal value while keeping all other parameters fixed. For each set of parameters we calculate the analytical power spectrum and the eigenvalues of the Jacobian (linear stability matrix) of the stochastic model evaluated at a fixed point found numerically. We classify each set of parameters as either producing an unstable homogeneous state at wavenumber $k = 0$, a stable homogeneous state, a stochastic Turing pattern, or a deterministic Turing pattern. We classify a set of parameters as producing a pattern if they produce a peak in the calculated power spectrum at a nonzero wavenumber. To distinguish between stochastic Turing patterns and deterministic Turing patterns we examine the eigenvalues of the corresponding Jacobian. If the real part of all the eigenvalues is negative for all wavenumbers then the pattern must be due to stochasticity. If there is any range of wavenumbers that have corresponding positive real parts of their eigenvalues then the pattern is produced by the traditional Turing mechanism.

The results of this analysis are presented in Figure S22. This phase diagram indicates parameter ranges that produce unstable fixed points in red, stochastic patterns in blue, deterministic Turing pattern in green, and homogeneous stable states in magenta. To determine the sensitivity of the system to particular parameters we examined how the maximum eigenvalue of the Jacobian changed. In Figure S23 we have plotted the change in the real part of the maximum eigenvalue as a parameter is varied from half of its value to 1.5x its value. Positive changes, colored in red, indicate that increasing the corresponding parameter promotes traditional Turing patterns. Negative values, colored in blue, indicate that increasing the corresponding parameter promotes stochastic patterns. The amplitude of the change gives an indication of the sensitivity of the parameter.

We also used Latin hypercube sampling to randomly generate 500 parameter sets where all the parameters were allowed to vary between half their nominal value and 1.5x their nominal value. For this analysis we found that 24.8% of parameters produced unstable fixed points, 43.2% produced stable homogeneous states, 13.2% produced stochastic Turing patterns, and 18.8% produced Turing patterns. This shows that this complex stochastic model can produce the same behaviors as our effective model. Additionally it shows that by including stochasticity, the range in which patterns can form has been increased by 70%.

To calculate the analytic power spectrum we used a method similar to that described in S9. We wrote down the transition probabilities for the stochastic model directly from our deterministic model. For example, the transition probability for U gaining a particle is $T(U \to U+1) = \alpha_u I_u$ and the transition probability for U losing a particle is $T(U \to U-1) = \gamma_u U$. Using a system size expansion one can derive Langevin equations governing the fluctuations of the form

$$\partial_t x = Ax + \xi \text{ where } \left\langle \xi(t)\xi^{\dagger}(t') \right\rangle = B\delta(t-t'), \quad [53]$$

where in the case of this model

$$\begin{aligned} A &= J - \mathrm{diag}([D_u k^2, D_v k^2, 0, 0, 0]) && [54] \\ B &= \mathrm{diag}([\alpha_u I_u + \gamma_u U + D_u k^2 U, \alpha_v I_v + \gamma_v V + D_v k^2 V, \\ &\quad \alpha_{iu} F_1(X_1, C) + \gamma_{iu} I_u, \alpha_{iv} F_1(X_1, C) + \gamma_{iv} I_v, \\ &\quad \alpha_c F_2(X_2, L) + \gamma_c C]) && [55] \\ x^{\dagger} &= [\delta U, \delta V, \delta I_u, \delta I_v, \delta C], && [56] \end{aligned}$$

and J is the Jacobian of the model evaluated at the fixed point. Using these equations the power spectrum is calculated to be $P(k, w=0) = \langle xx^{\dagger} \rangle = A^{-1} B (A^{-1})^{\dagger}$. The fixed point, Jacobian, and power spectrum are numerically calculated using a custom Matlab script. Figure S24 shows the calculated power spectrum corresponding to the parameters listed in Table S6. In this figure the full model produces power spectrum with a power law tail of -2 for the inhibitor and an initial power law tail of -4 for the activator before undergoing a crossover to a -2 power law. The eigenvalues of the spatially extended Jacobian, A, are plotted in Figure S25 showing that all eigenvalues are negative. This indicates that the set of parameters in Table S6 produces a stochastic Turing pattern.

9. Stochastic Turing Patterns

In many biological and physical problems, noise is understood as a destabilizing agent. It thus comes as a surprise that when Turing-like systems are subject to noise, noise acts as a stabilizing agent for the spatially patterned state, enlarging its regime in the phase diagram. For both the case of noise external to the system (extrinsic noise) and noise associated with the discrete creation and annihilation of chemicals (demographic noise), patterns exist for a wider range of parameter space than would be the case deterministically(29, 30). The demographic noise of the signaling molecules, where one acts as an activator of gene expression and another an inhibitor, relax the criteria for separation of diffusion scales and enlarge the parameter space in which patterns should form. Patterns of this type are known as stochastic Turing patterns. Predictions for the power spectrum, the characteristic scale, and parameter regime in which stochastic Turing patterns form have been made by Butler and Goldenfeld (29).

A. Power spectra analysis of experimental observations. To test the predictions of stochastic Turing pattern theory we constructed power spectra for the experimental data. We converted the pictures of red and green fluorescent proteins into gray scale images and subtracted off the mean intensity to obtain data corresponding to the fluctuations. We then conducted a discrete two-dimensional (2D) Fourier transform of the data, finding its amplitude squared. Since it is clear from the resulting Fourier transforms that the patterns are isotropic, we perform an angular average (Figure S13a). The resulting radial power spectrum can be compared to the predictions made by Butler and Goldenfeld (29) (Figure S13c). By fitting the tail we find a power law with $\sigma = -2.3 \pm 0.4$ consistent with demographic noise. It is possible to obtain anomalous power law tails in the power spectrum due to discontinuities in the boundaries of the picture, but these artifacts are distinguishable by their lack of noise, and we are confident that such spectral leakage is not being observed in these data. The Fourier transform for the red fluorescent channel is not isotropic and the corresponding radial power spectrum has a power law with $\sigma = -3.9 \pm 0.4$ (Figure S13b,d). Radial power spectra were also calculated for other concentrations of IPTG as shown in figures S14 and S15. The spectra produced are also consistent with predictions of demographic noise.

B. Stochastic Turing pattern model. The traditional Turing mechanism usually consists of at least two chemicals. One of the chemicals is a slowly diffusing activator, activating the synthesis of itself and the inhibitor. The other chemical is a fast diffusing inhibitor, inhibiting synthesis of the activator and itself. The Turing mechanism can be explained by a simple qualitative argument consisting of three steps. Initially activator and inhibitor are distributed randomly. Areas with local concentrations of activator will autocatalytically

grow, forming dense clumps of activator. Inhibitor will also be produced near these clumps of activator. The rapidly diffusing inhibitor will suppress the spread of the clumps of activator. This simple picture of activator-inhibitor dynamics does not require large separation of diffusion rates or depend on details of rates. When this system is considered classically, however, it is found to either require fine tuning of reaction rates or have a large separation of diffusion rates. We will see shortly that the stochastic treatment solves this fine tuning problem.

Our synthetic system is system is designed to implement an activator-inhibitor system with $A_{3OC12HSL}$ as an activator of its own synthesis and that of I_{C4HSL}, while I_{C4HSL} is an inhibitor of both chemicals. To develop a simplified model of the activator inhibitor circuit, one can write down reaction diffusion equations for this system that are mathematically equivalent to the Levin-Segel model of herbivore-plankton interaction (31).

$$\partial_t \phi = \mu \nabla^2 \phi + b\phi + e\phi^2 - p\psi\phi \quad [57]$$

$$\partial_t \psi = \nu \nabla^2 \psi + p\psi\phi - d\psi^2 \quad [58]$$

Here ϕ is the concentration of activator ($A_{3OC12HSL}$), ψ is the concentration of inhibitor (I_{C4HSL}), μ and ν are the the diffusion constants of the activator and inhibitor respectively. The term $p\psi\phi$ is a competition term, $e\phi^2$ is a nonlinear activation term, and $-d\psi^2$ is a nonlinear self inhibition term for the inhibitor. These equations exhibit a Turing instability when (31):

$$\frac{\nu}{\mu} > \left(\frac{1}{\sqrt{p/d} - \sqrt{p/d - e/p}} \right)^2. \quad [59]$$

To consider the effects of extrinsic noise we can simply add white noise ξ to the system of equations above. Then we can construct the Fourier transformed stability matrix and solve for the power spectrum $\hat{P}(k,w)$ where k is the wave-number and w is frequency. When this is done it is found that the power spectrum has a power law tail, $\hat{P}(k, w=0) = \frac{k^\sigma}{\nu^2} \langle \xi\, \xi \rangle, k \gg k_m$ with an exponent $\sigma = -4$ (29). In addition, the condition for pattern formation becomes $\frac{\nu}{\mu} > \frac{p}{e}$.

Intrinsic noise, represented for example by copy number fluctuations arising from stochastic gene expression, can be studied by writing down an individual level model for the activator and inhibitor. The following set of chemical reactions describe the effective activator-inhibitor system that we engineered:

$$\begin{array}{lll} A \xrightarrow{b} AA & AI \xrightarrow{p_1/V} I & II \xrightarrow{d/V} I \\ AA \xrightarrow{e/V} AAA & AI \xrightarrow{p_2/V} II & \end{array} \quad [60]$$

Here A is the activator ($A_{3OC12HSL}$) and I is the inhibitor (I_{C4HSL}) and V is the well-mixed patch size setting the strength of the fluctuations. From these first order reactions one can derive a master equation governing the probability of having m molecules of I and n molecules of A at a given time:

$$\begin{aligned} \partial t P(m,n) =& b[(n-1)P(m,n-1) - nP(m,n)] + \frac{e}{V}[(n-1)(n-2)P(m,n-1) - n(n-1)P(m,n)] \\ &+ \frac{p_1}{V}[m(n+1)P(m,n+1) - mnP(m,n)] + \frac{p_2}{V}[(m-1)(n+1)P(m-1,n+1) - mnP(m,n)] \\ &+ \frac{d}{V}[(m+1)mP(m+1,n) - m(m-1)P(m,n)] \end{aligned} \quad [61]$$

To introduce spatial variations, the master equation can be conveniently represented as a path integral, from which mean-field equations and Langevin equations with multiplicative noise governing the fluctuations are obtained by van Kampen expansion (29). We calculate the power spectrum $\hat{P}(k,w)$ as a function of frequency w and wave-number k, obtaining a power spectrum tail ($k \gg k_m$): $\hat{P}(k, w=0) \approx \frac{\psi}{\nu} k^\sigma$ (inhibitor), $\hat{P}(k, w=0) \approx \frac{\phi}{\mu} k^\sigma$ (activator) with $\sigma = -2$. Patterns arise when

$$\frac{\nu}{\mu} > \left(\frac{p}{e}\right) \frac{5 + 7(de/p^2)}{4 + 5(de/p^2) + 3(de/p^2)^2}. \quad [62]$$

Additionally the wavelength, λ, or characteristic spacing of the pattern turns out to be the same as that for a classical Turing pattern (29) and is found to be

$$\lambda = 2\pi\sqrt{\frac{2}{\phi}\frac{\mu\nu}{e\nu - p\mu}}. \quad [63]$$

C. Stochastic model power spectra analysis. We now discuss the origin of the exponent discussed above, from the standpoint of two models that we have constructed to analyze the data. The first model is a coarse-grained phenomenological or minimal model for the morphogens. The second model is a detailed stochastic model, described in SI 8. We will see that there are two factors contributing to the -2 exponent in the inhibitor channel and the -4 exponent in the activator channel, in the context of intrinsic noise. Note that extrinsic noise, if present, would lead to an exponent of -4, but in both channels. The first explanation is that activator channel had a very sharp threshold for expressing the red fluorescence and the pictures were overexposed. This overexposure can suppress the small-scale correlations in the patterns. This idea is supported by taking data from simulations of demographic-noise induced patterns and performing image operations on the data to simulate this effect. We ran the simulated data through an image dilation morphological operator with a disk structural element 1px in radius. The resulting power spectra have power law tails with $\sigma = -4$, even though the original data were intrinsic noise-induced, having a power law tail with $\sigma = -2$. Thus, an asymptotic power-law tail of -2 in the power spectrum appears as an effective exponent of -4 in the presence of overexposure. This is further supported by looking at the spectra in figures S14 and S15. These images, taken at other IPTG concentrations, were not overexposed and their spectra have power law tails with exponents closer to -2.

The second explanation uses the detailed stochastic model described in SI 8. This model also predicts power-law tails with $\sigma = -2$ for both the activator and inhibitor, at asymptotically large values of k, because, when coarse-grained, the model should be well-described by the phenomenological model for the morphogens alone. But for the range of parameters that we estimate are consistent with the experimental data, the detailed model also predicts that for a wide range of intermediate wavenumbers, there is an effective power-law with $\sigma = -4$ for the activator, before undergoing a crossover to a power law with $\sigma = -2$ at high wave-numbers. Our interpretation is that the experiment is indeed well-described by the detailed model, and that we are observing the behavior before the crossover point in the power spectrum of the RFP channel. Overexposure does not cause any additional change to the effective -4 exponent.

The measured diffusion ratio of $\frac{\nu}{\mu} = 21.6$ is too small to produce classical Turing patterns. In fact to produce patterns qualitatively similar to the ones observed, the diffusion constants must be separated by a factor on the order of 100 in our non-stochastic simulation (See figure 3f). We can also plot the estimated range of parameters for our effective model and compare them to regimes where normal Turing patterns form and stochastic Turing patterns form (Figure S13e). We see from this plot that the estimated parameters fall mainly in the regime where stochastic patterns form, but not where normal Turing patterns can form. Any parameters above the blue surface will form classical Turing patterns. Any parameters above the green surface can form stochastic Turing patterns. The yellow oval representing our estimated range of effective parameters falls mainly below the blue surface but is above the green surface, indicating most of the parameters fall within the regime of stochastic patterns. We estimated the values and ranges of the ratios $\frac{\nu}{\mu}$, $\frac{e}{p}$, and $\frac{d}{p}$ which solely control pattern formation in the reduced model. In our analysis we used the the experimentally measured ratio of diffusion constants $\frac{\nu}{\mu} = 21.6 \pm 10$ and we estimated $\frac{e}{p} < 1$ by using the knowledge that for any pattern to form, either classical or stochastic, the homogeneous state must first be stable so $p > e$. Finally since the degradation rate is always smaller than the rate of production of our molecules we estimated $\frac{d}{p} < 1$. Even at our measured values of diffusion constants our stochastic simulation continued to produce patterns similar to the ones observed in our experiment and produced a power spectrum power law tail with $\sigma - 2.4$ consistent with our experiment.

1. Gierer A, Meinhardt H (1972) A theory of biological pattern formation. *Biol. Cybern.* 12(1):30–39.
2. Whiteley M, Lee K, Greenberg E (1999) Identification of genes controlled by quorum sensing in Pseudomonas aeruginosa.
3. Schuster M, Lostroh C, Ogi T, Greenberg E (2003) Identification, timing, and signal specificity of Pseudomonas aeruginosa quorum-controlled genes: a transcriptome analysis. *J. Bacteriol.* 185(7):2066.
4. Schuster M, Urbanowski M, Greenberg E (2004) Promoter specificity in Pseudomonas aeruginosa quorum sensing revealed by DNA binding of purified LasR. *Proc. Natl. Acad. Sci. U.S.A.* 101(45):15833–15839.
5. Stewart P (2003) Diffusion in Biofilms. *J. Bacteriol.* 185(5):1485–1491.
6. Karig D (2007) Ph.D. thesis (Princeton University, Princeton, NJ).
7. Huang JJ, Han JI, Zhang LH, Leadbetter JR (2003) Utilization of acyl-homoserine lactone quorum signals for growth by a soil pseudomonad and Pseudomonas aeruginosa PAO1. *Appl Environ Microbiol* 69(10):5941–9.
8. Stricker J, et al. (2008) A fast, robust and tunable synthetic gene oscillator. *Nature* 456(7221):516–519.
9. Schaefer AL, Val DL, Hanzelka BL, Cronan, J. E. J, Greenberg EP (1996) Generation of cell-to-cell signals in quorum sensing: acyl homoserine lactone synthase activity of a purified Vibrio fischeri LuxI protein. *Proc Natl Acad Sci U S A* 93(18):9505–9.
10. Goldbeter A, Koshland, D. E. J (1981) An amplified sensitivity arising from covalent modification in biological systems. *Proc Natl Acad Sci U S A* 78(11):6840–4.
11. Gunawardena J (2005) Multisite protein phosphorylation makes a good threshold but can be a poor switch. *Proc Natl Acad Sci U S A* 102(41):14617–22.
12. Brenner K, Karig D, Weiss R, Arnold F (2007) Engineered bidirectional communication mediates a consensus in a microbial biofilm consortium. *Proc. Natl. Acad. Sci. U.S.A.* 104(44):17300.
13. Basu S, Mehreja R, Thiberge S, Chen M, Weiss R (2004) Spatiotemporal control of gene expression with pulse-generating networks. *Proc. Natl. Acad. Sci. U.S.A.* 101(17):6355–6360.
14. Karig D, Weiss R (2005) Signal-amplifying genetic circuit enables in vivo observation of weak promoter activation in the Rhl quorum sensing system. *Biotechnol Bioeng* 89(6):709–18.
15. Yokobayashi Y, Weiss R, Arnold FH (2002) Directed evolution of a genetic circuit. *Proc Natl Acad Sci U S A* 99(26):16587–91.
16. Andersen JB, et al. (1998) New unstable variants of green fluorescent protein for studies of transient gene expression in bacteria. *Appl Environ Microbiol* 64(6):2240–6.
17. Weiss R, Basu S (2002) The device physics of cellular logic gates in *NSC-1: The First Workshop on NonSilicon Computing.* pp. 54–61.
18. Pearson J, Pesci E, Iglewski B (1997) Roles of Pseudomonas aeruginosa las and rhl quorum-sensing systems in control of elastase and rhamnolipid biosynthesis genes. *J. Bacteriol.* 179(18):5756–5767.
19. Weiss R (2001) Ph.D. thesis (Massachusetts Institute of Techonology, Cambridge, MA).
20. Gardner T, Cantor C, Collins J (2000) Construction of a genetic toggle switch in Escherichia coli. *Nature* 403(6767):339–342.
21. Weiss R, Knight T (2001) Engineered communications for microbial robotics. *Lect. Notes. Comput. Sc.* 2054:1–16.
22. Verhulst P (1838) 'Notice sur la loi que la population poursuit dans son accroissement. *Correspondance Mathe-matique et Physique* 10:113–121.
23. Chen C, Riadi L, Suh S, Ohman D, Ju L (2005) Degradation and synthesis kinetics of quorum-sensing autoinducer in Pseudomonas aeruginosa cultivation. *J. Biotechnol.* 117(1):1–10.
24. Pearson J, Van Delden C, Iglewski B (1999) Active efflux and diffusion are involved in transport of Pseudomonas aeruginosa cell-to-cell signals. *Journal of bacteriology* 181(4):1203–1210.
25. Pesci E, Pearson J, Seed P, Iglewski B (1997) Regulation of las and rhl quorum sensing in Pseudomonas aeruginosa. *J. Bacteriol.* 179(10):3127–3132.
26. Moran P (1950) Notes on continuous stochastic phenomena. *Biometrika* 37:17–33.
27. Cao Y, Gillespie D, Petzold L (2006) Efficient step size selection for the tau-leaping simulation method. *J. Chem. Phys.* 124:044109.
28. Rossinelli D, Bayati B, Koumoutsakos P (2008) Accelerated stochastic and hybrid methods for spatial simulations of reaction–diffusion systems. *Chem. Phys. Lett.* 451(1-3):136–140.
29. Butler T, Goldenfeld N (2011) Fluctuation-driven turing patterns. *Physical Review E* 84(1):011112.
30. Biancalani T, Fanelli D, Di Patti F (2010) Stochastic turing patterns in the brusselator model. *Physical Review E* 81(4):046215.
31. Levin SA (1976) Hypothesis for origin of planktonic patchiness. *Nature* 259:659.

Table S5. Variables used in the model.

Symbol	Molecule
U	$3OC_{12}HSL$
V	C_4HSL
I_u	LasI
I_v	RhlI
C	CI
R_u	LasR
R_v	RhlR
L	free LacI
X_1	LasR-$3OC_{12}HSL$ complex
X_2	RhlR-C_4HSL complex

Table S6. Definitions and values for the rate constants used in our mathematical model.

Parameter	Description	Value	Unit
α_u	$A_{3OC12HSL}$ production rate	3.0×10^1	hr^{-1}
γ_u	$A_{3OC12HSL}$ degradation rate	1.0	hr^{-1}
D_u	$A_{3OC12HSL}$ diffusion coefficient	5.0×10^{-1}	$grid^2/hr$
α_v	I_{C4HSL} production rate	3.0×10^1	hr^{-1}
γ_v	I_{C4HSL} degradation rate	1.0	hr^{-1}
D_v	I_{C4HSL} diffusion coefficient	10.8 or 50^*	$grid^2/hr$
α_{iu}	Basal production rate of LasI	1.0×10^1	molecules/hr
γ_{iu}	Degradation rate of LasI	1.0	hr^{-1}
α_{iv}	Basal production rate of RhlI	0.3	molecules/hr
γ_{iv}	Degradation rate of RhlI	1.0	hr^{-1}
α_c	Basal production rate of CI	1.0×10^1	molecules/hr
γ_c	CI degradation rate	1.0	hr^{-1}
λ_u	Ratio between LasR and LasI	1.0	$\diagup$
λ_v	Steady state level of RhlR by $\lambda_{P(R-O1)}$ w/o CI regulation	1.0×10^3	molecules
λ_l	Steady state level of LacI from p_{lacq} expression	1.5×10^2	molecules
K_{c3}	$A_{3OC12HSL}$-RhlR dissociation constant	1.5×10^2	molecules
I	IPTG concentration	$1.0 \times 10^{-6\sim-2}$	M

Table S7. Additional definitions and values for the rate constants used in our mathematical model.

Parameter	Description	Value	Unit
θ_1	Hill coeff. for LasR-$A_{3OC12HSL}$ complex activation of $P_{Las-OR1}$	1.0	⁄
K_{d1}	Disso. constant of LasR-$A_{3OC12HSL}$ complex with $P_{Las-OR1}$	1.0×10^3	molecules
f_1	Fold change for full induction of $P_{Las-OR1}$	1.0×10^3	⁄
θ_2	Hill coeff. for CI repression of $P_{Las-OR1}$	2.0	⁄
K_{d2}	Disso. constant of CI with $P_{Las-OR1}$	1.0×10^1	molecules
f_2	Fold change for full inhibition of $P_{Las-OR1}$	1.0×10^5	⁄
θ_3	Hill coeff. for RhlR-I_{C4HSL} complex activation of $P_{Las-OR1}$	1.0	⁄
K_{d3}	Disso. constant of RhlR-I_{C4HSL} complex with pRhl-lacO	1.0×10^5	molecules
f_3	Fold change for full induction of pRhl-lacO	1.0×10^3	⁄
θ_4	Hill coeff. for the LacI activation of pRhl-lacO	4.0	⁄
K_{d4}	Disso. constant of LacI with pRhl-lacO	1.0×10^2	molecules
f_4	Fold change for full inhibition of pRhl-lacO	1.0×10^3	⁄
θ_5	Hill coeff. for the CI activation of $\lambda_{P(R-O1)}$	2.0	⁄
K_{d5}	Disso. constant of CI with $\lambda_{P(R-O1)}$	1.0×10^3	molecules
f_5	Fold change for full induction of $\lambda_{P(R-O1)}$	1.0×10^5	⁄
θ_6	Hill coeff. for the IPTG binding to LacI	1.0	⁄
K_{d6}	Disso. constant of IPTG with LacI	1.0×10^{-3}	M
f_6	Fold change of LacI activity for IPTG full induction	1.0×10^5	⁄

Figure Captions

Figure S1: Design of Turing pattern formation system. **a**, $A_{3OC12HSL}$ serves as the activator species and catalyzes its own synthesis as well as that of I_{C4HSL}. I_{C4HSL} is the inhibitor, as this signal ultimately represses production of $A_{3OC12HSL}$ and I_{C4HSL}. **b**, Initial genetic network implementation. $A_{3OC12HSL}$ binds LasR and activates p(Las)-OR1 promoters that express LasI and RhlI. LasI catalyzes synthesis of $A_{3OC12HSL}$, and RhlI catalyzes synthesis of I_{C4HSL}. I_{C4HSL} binds RhlR and activates p(Rhl)-OR1, which expresses CI, and CI represses the p(Las)-OR1 promoters in addition to p(Rhl)-OR1. **c**, Modeling results suggested that a design with a CI OR1 binding site in the promoter expressing RhlR instead of in p(Rhl) was more enriched for Turing instabilities. **d**, Placing LasR under control of the p(Las)-OR1 promoter effectively increases the p(Las)-OR1 response sensitivity to $A_{3OC12HSL}$. For clarity, arrows were not shown in (c) and (d) to indicate LasR binding $A_{3OC12HSL}$ and activating p(Las)-OR1 or RhlR binding I_{C4HSL} and activating p(Rhl).

Figure S2: Computational exploration of design variations. **a**, Several different designs were simulated with CI OR1 binding domains in different combinations of promoters and both with and without $A_{3OC12HSL}$ degrading acylase. In the simulations, a promoter contains an OR1 domain if the corresponding bit in the binary representation of the network number is a 1. Likewise, acylase is expressed only if bit_6 of the binary representation of the network number is 1. For example, $56_{10} = 0111000_2$, so Network 56 has an OR1 site in the p(Las)-OR1 promoters expressing LasI and RhlI and in the promoter expressing RhlR since bit_3, bit_4, and bit_5 are all 1. **b**, Number of random parameter sets found for each network. Although Network 106 was most enriched for Turing instabilities, this network requires acylase expression. Networks 56 and 57, depicted in Figure S1c, which do not require acylase expression were ultimately chosen instead.

Figure S3: Constitutive LasR and p(Las) controlled LasR. **a**, Genetic network with constitutively expressed LasR and a p(Las) promoter expressing a reporter gene. **b**, Genetic network with p(Las) expressing both a reporter and LasR. **c**, Reporter expression versus $A_{3OC12HSL}$ for these networks using the following parameters: $\alpha_0 = 0.01$, $\alpha_1 = 1$, $K = 0.5$, $d = 1$, $m = 1$.

Figure S4: Plasmids used in our patterning and control experiments. **a**, Plasmid pFNK-512 implements activation of $A_{3OC12HSL}$ and I_{C4HSL}. It corresponds to the upper part of the circuit diagram in Figure 1b in the main text. **b**, Plasmid pFNK-804-LacO-LacI corresponds the lower part of the circuit diagram. It implements inhibition of both signals. **c**, Plasmid pFNK806 is derived from pFNK804-LacO-LacI and provides better contrast between green and red fluorescence intensities. **d**, Plasmid pTOG-1 is a two-color bistable toggle switch. It is used to explore the role of collective commitment in pattern formation. **e-f**, pINV-5 and pASK-201 are IPTG-inducible plasmids that produce GFP and RFP correspondingly. Both are used in our control experiments. **g**, Sequences for the hybrid promoters $P_{Las-OR1}$ and $P_{Rhl-lacO}$.

Figure S5: Liquid AHL dosage response curves for the reporter cells. The red curve is the $A_{3OC12HSL}$ response of cells harboring pFNK-503-qscrsaL, a $A_{3OC12HSL}$ detector plasmid. The blue curve is the I_{C4HSL} response of cells harboring the receiver plasmid pFNK-202-qsc119, a I_{C4HSL} detector plasmid.

Figure S6: Comparison of our experimental data with modeling results. **a-b**, Fluorescence intensity of receiver cells in response to AHL gradients in 2% M9 agar plates. In both panels, the four curves correspond to hours 0, 2.5, 5, and 8.75. **c-d**, For simulations, fluorescence intensity simulation results were obtained using our mathematical model. The estimated diffusion coefficient for $A_{3OC12HSL}$ is 83 $\mu m^2/s$ and for I_{C4HSL} is 1810 $\mu m^2/s$.

Figure S7: Additional experiments to verify that diffusion rate calculations are reasonably robust to changing biofilm characteristcs over time. Fluorescence intensity of receiver cells in response to AHL gradients in 2% M9 agar plates.The four curves correspond to hours 0, 2.5, 5, and 8.

Figure S8: Competitive binding of $A_{3OC12HSL}$ to RhlR inhibits activation of promoter p_{Rhl} by I_{C4HSL}. **a**, GFP expression from p_{Rhl} promoter is induced by I_{C4HSL} (blue bar) but is not induced by $A_{3OC12HSL}$ (red bar). **b**, GFP expression from p_{Rhl} promoter decreases with $A_{3OC12HSL}$ for a fixed concentration of I_{C4HSL}.

Figure S9: Populations of *E. coli* expressing constitutive fluorescent reporter proteins GFP or mCherry were mixed in various ratios of

[Green:Red] on M9 supplemented minimal media and then imaged by microscopy. Scale bar, 200 µm.

Figure S10: Behavior of cell populations with each cell harboring an intracellular green/red bistable toggle switch. **a**, A bistable toggle switch derived from Gardner *et al* (20). **b**, Flow cytometry fluorescence density plot of the toggle cells at time 0. **c**, Flow cytometry fluorescence density plot of cells scraped from the cell lawn at 24 hours. **d**-**e**, Microscope images of cell lawns harboring the toggle switch circuit at 24 hours. Both RFP (**d**) and GFP (**e**) are homogeneously distributed and qualitatively different from that of a population carrying the emergent circuit in Fig. 2**a**. Scale bar, 100 µm. **f**, Fluorescence density plot of the microscope images in panels **d**-**e**.

Figure S11: Moran's I of the patterns from our deterministic simulations.

Figure S12: Emergence of patterns over time. Snapshots of red fluorescence were taken every 30 minutes for 32 hours. Shown are images in 4-hour intervals. Scale bar, 100 µm. Left: Average minimium distance between spots as a function of time, blue shading indicates standard deviation. Right: Average spot diameter as a function of time.

Figure S13: **a**, GFP image and corresponding Fourier transform. **c**, Radial power spectrum of GFP and power law fit of -2.3. **b**, RFP image and corresponding Fourier transform. **d**, Radial Power spectrum of RFP with a powerlaw tail fit of -3.9. **e**, Pattern forming regimes in parameter space and estimated parameters for our system. The parameters fall above the region where stochastic patterns form but below the region where normal Turing patterns form. **f**, Characteristic separation of spots with average separation of $32 \pm 8 px$ (45 ± 11 μm).

Figure S14: RFP images and their corresponding Radial Power spectrums with powerlaw tail fits of -2.5, -2.5, -2.9 for IPTG concentrations of 10^{-3} M, $10^{-2.5}$ M, and 10^{-2} M respectively.

Figure S15: GFP images and corresponding Radial Power spectrums with a powerlaw tail fits of -2.1, -2.2, -2.2 for IPTG concentrations of 10^{-3} M, $10^{-2.5}$ M, and 10^{-2} M respectively. At IPTG concentrations smaller than 10^{-4} M The green channel begins to look spatially homogeneous as the signal is not strong enough to show-up beyond the background camera noise.

Figure S16: $A_{3OC12HSL}$ and I_{C4HSL} patterns produced in our stochastic simulation using the parameters given in Tables S6-S7. The red line indicates the location of the cross-section used for all other dynamic variables. Cross-sectional slices of variables U ($A_{3OC12HSL}$), V (IC4HSL), I_u (LasI), I_v (RhlI), C (CI), R_u (LasR), R_v (RhlR), L (free LacI), X_1 (LasR-$A_{3OC12HSL}$ complex), and X_2 (RhlR-I_{C4HSL} complex).

Figure S17: $A_{3OC12HSL}$ patterns produced in our stochastic simulation using $D_v/D_u = 100$ and the parameters given in Tables S6-S7 for three different concentrations of IPTG.

Figure S18: Spot size and spacing distributions for 30C12HSL produced in our stochastic simulation with $D_v/D_u = 100$ for three different values of IPTG.

Figure S19: $A_{3OC12HSL}$ patterns produced in our stochastic simulation using the measured diffusion ratio of $D_v/D_u = 21.6$ and the parameters given in Tables S6-S7 for three different concentrations of IPTG.

Figure S20: 2D power spectrum and radial power spectrum for 30C12HSL produced in our stochastic simulation using $D_v/D_u = 21.6$ for three different values of IPTG.

Figure S21: Spot size and spacing distributions for 30C12HSL produced in our stochastic simulation using $D_v/D_u = 21.6$ for three different values of IPTG.

Figure S22: Phase Diagram showing the type of phase as each parameter is varied from half of its nominal value to 1.5x its nominal value while keeping all other parameters fixed. Red indicates an unstable fixed point, magenta a stable homogeneous state, blue a stochastic pattern, and green deterministic Turing pattern.

Figure S23: Sensitivity of a phase to a parameter is indicated by plotting the difference in eigenvalues between 1.5x the nominal value of a parameter and half of the nominal value. Red indicates a parameter that when increased promotes traditional Turing patterns and blue indicates a parameter promoting stochastic patterns.

Figure S24: The Analytic power spectrum calculated for the parameter set given in Tables S1-S2.

Figure S25: The real part of the eigenvalues of the Jacobian for the parameter set given in Tables S1-S2 plotted as a funtion of k. All the eigenvalues are negative indicating that the pattern formed is stochastic.

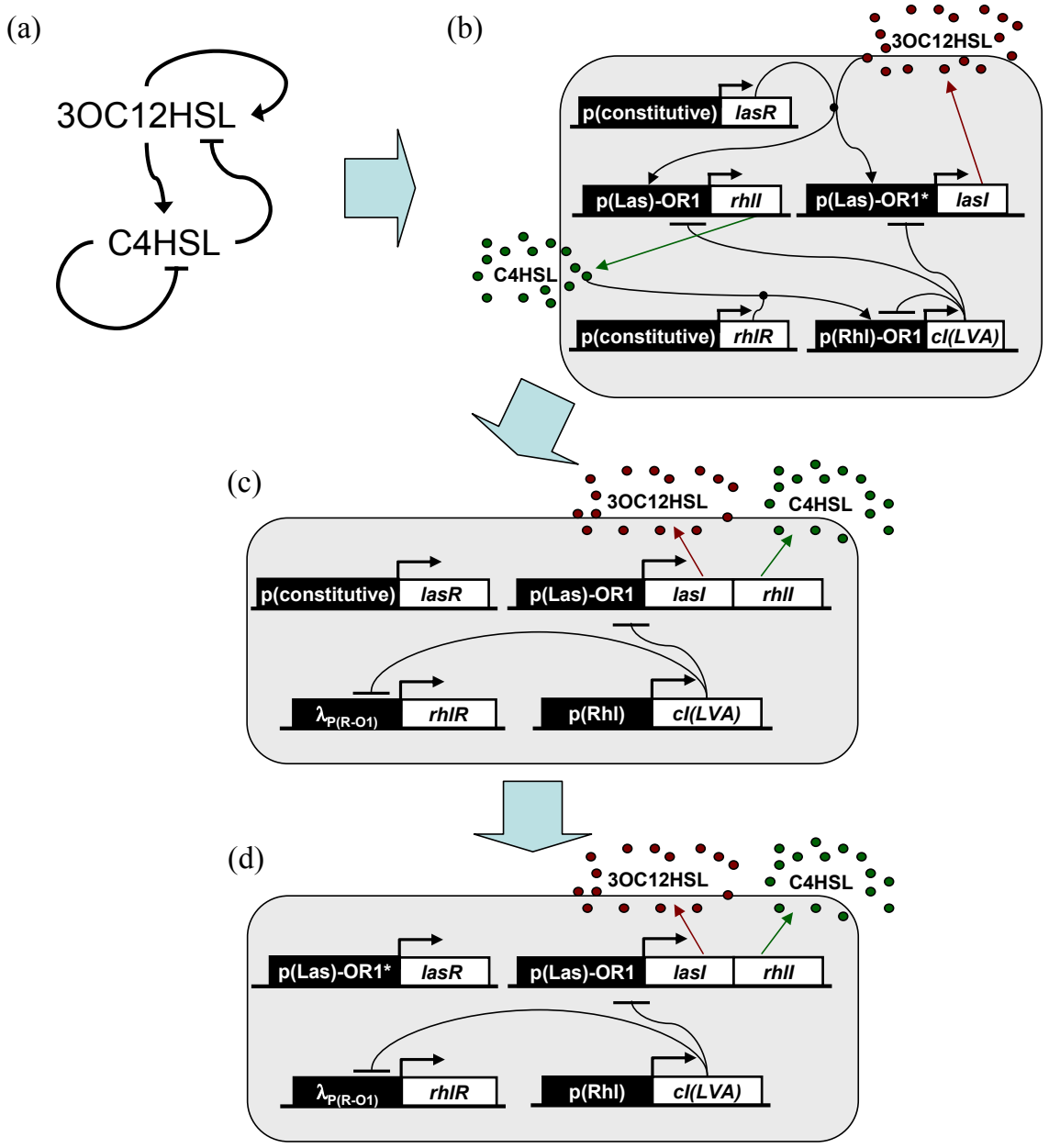

Fig. S1. Design of Turing pattern formation system. **a**, $A_{3OC12HSL}$ serves as the activator species and catalyzes its own synthesis as well as that of I_{C4HSL}. I_{C4HSL} is the inhibitor, as this signal ultimately represses production of $A_{3OC12HSL}$ and I_{C4HSL}. **b**, Initial genetic network implementation. $A_{3OC12HSL}$ binds LasR and activates p(Las)-OR1 promoters that express LasI and RhlI. LasI catalyzes synthesis of $A_{3OC12HSL}$, and RhlI catalyzes synthesis of I_{C4HSL}. I_{C4HSL} binds RhlR and activates p(Rhl)-OR1, which expresses CI, and CI represses the p(Las)-OR1 promoters in addition to p(Rhl)-OR1. **c**, Modeling results suggested that a design with a CI OR1 binding site in the promoter expressing RhlR instead of in p(Rhl) was more enriched for Turing instabilities. **d**, Placing LasR under control of the p(Las)-OR1 promoter effectively increases the p(Las)-OR1 response sensitivity to $A_{3OC12HSL}$. For clarity, arrows were not shown in (c) and (d) to indicate LasR binding $A_{3OC12HSL}$ and activating p(Las)-OR1 or RhlR binding I_{C4HSL} and activating p(Rhl).

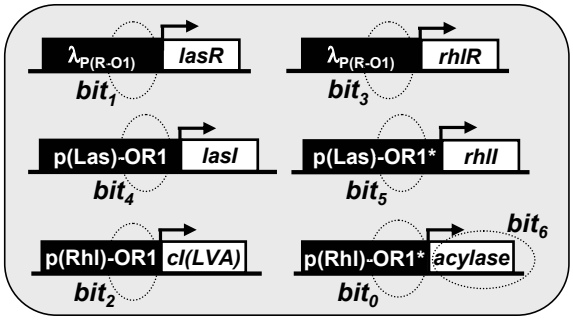

(a)

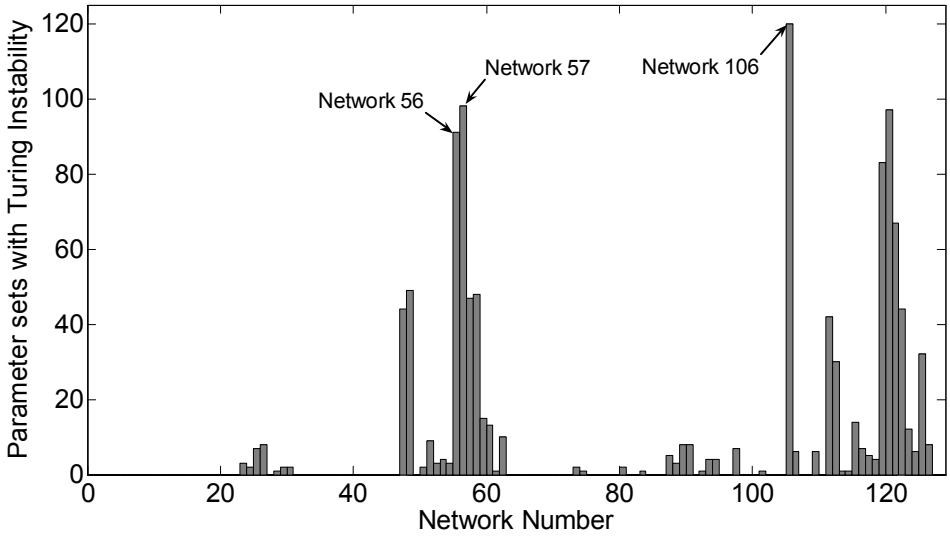

(b)

Fig. S2. Computational exploration of design variations. **a**, Several different designs were simulated with CI OR1 binding domains in different combinations of promoters and both with and without $A_{3OC12HSL}$ degrading acylase. In the simulations, a promoter contains an OR1 domain if the corresponding bit in the binary representation of the network number is a 1. Likewise, acylase is expressed only if bit_6 of the binary representation of the network number is 1. For example, $56_{10} = 0111000_2$, so Network 56 has an OR1 site in the p(Las)-OR1 promoters expressing LasI and RhlI and in the promoter expressing RhlR since bit_3, bit_4, and bit_5 are all 1. **b**, Number of random parameter sets found for each network. Although Network 106 was most enriched for Turing instabilities, this network requires acylase expression. Networks 56 and 57, depicted in Figure S1c, which do not require acylase expression were ultimately chosen instead.

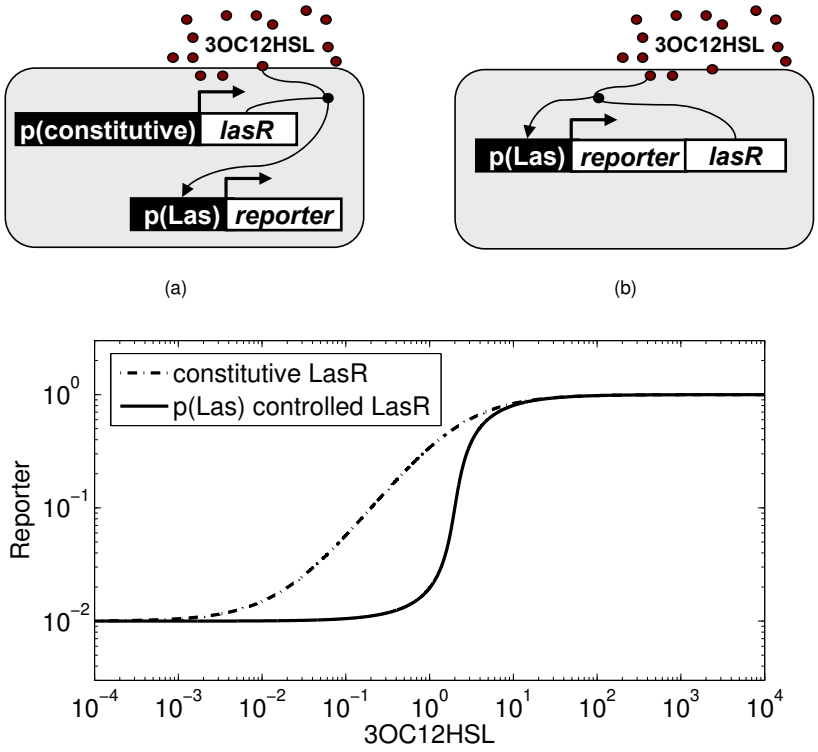

Fig. S3. Constitutive LasR and p(Las) controlled LasR. **a**, Genetic network with constitutively expressed LasR and a p(Las) promoter expressing a reporter gene. **b**, Genetic network with p(Las) expressing both a reporter and LasR. **c**, Reporter expression versus $A_{3OC12HSL}$ for these networks using the following parameters: $\alpha_0 = 0.01$, $\alpha_1 = 1$, $K = 0.5$, $d = 1$, $m = 1$.

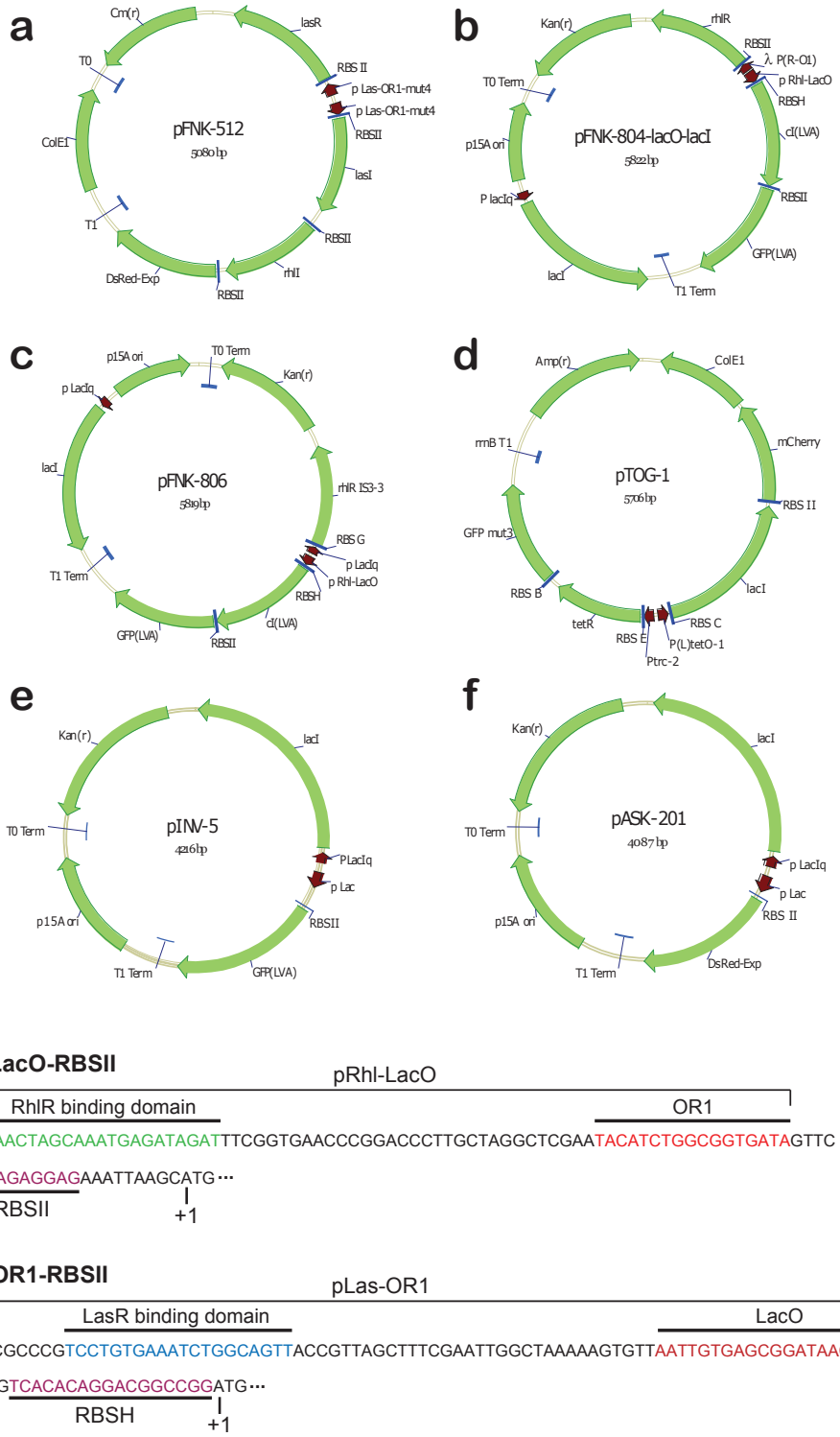

Fig. S4. Plasmids used in our patterning and control experiments. **a**, Plasmid pFNK-512 implements activation of $A_{3OC12HSL}$ and I_{C4HSL}. It corresponds to the upper part of the circuit diagram in Figure 1b in the main text. **b**, Plasmid pFNK-804-LacO-LacI corresponds the lower part of the circuit diagram. It implements inhibition of both signals. **c**, Plasmid pFNK806 is derived from pFNK804-LacO-LacI and provides better contrast between green and red fluorescence intensities. **d**, Plasmid pTOG-1 is a two-color bistable toggle switch. It is used to explore the role of collective commitment in pattern formation. **e-f**, pINV-5 and pASK-201 are IPTG-inducible plasmids that produce GFP and RFP correspondingly. Both are used in our control experiments. **g**, Sequences for the hybrid promoters $P_{Las-OR1}$ and $P_{Rhl-lacO}$.

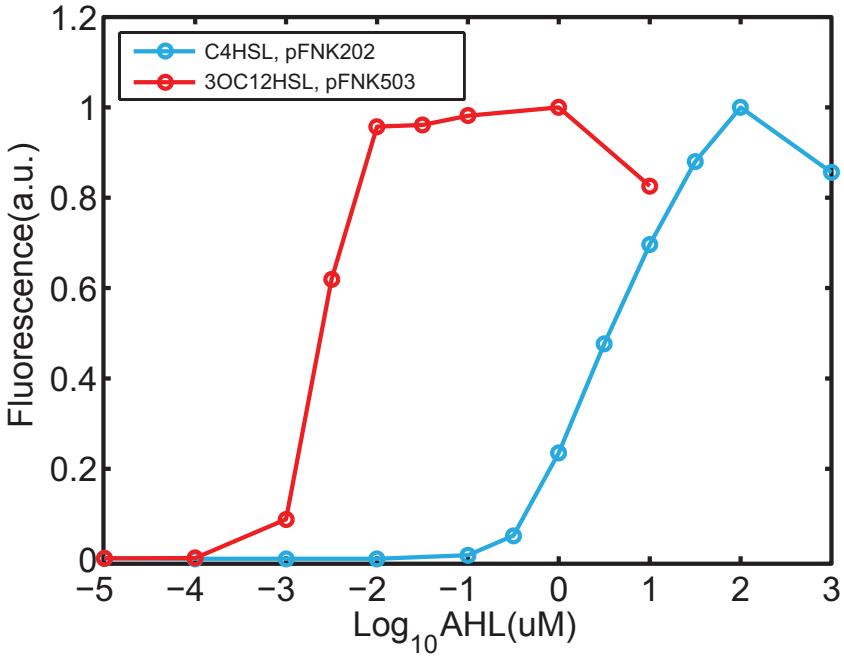

Fig. S5. Liquid AHL dosage response curves for the reporter cells. The red curve is the $A_{3OC12HSL}$ response of cells harboring pFNK-503-qscrsaL, a $A_{3OC12HSL}$ detector plasmid. The blue curve is the I_{C4HSL} response of cells harboring the receiver plasmid pFNK-202-qsc119, a I_{C4HSL} detector plasmid.

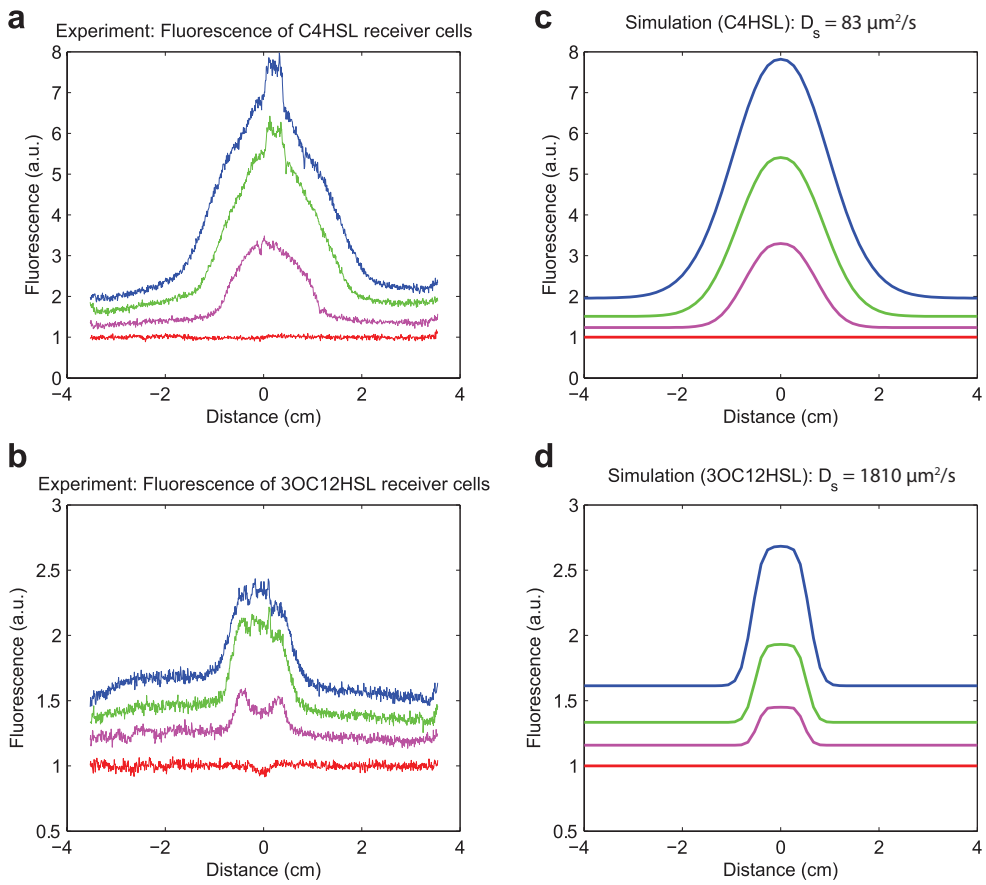

Fig. S6. Comparison of our experimental data with modeling results. **a-b**, Fluorescence intensity of receiver cells in response to AHL gradients in 2% M9 agar plates. In both panels, the four curves correspond to hours 0, 2.5, 5, and 8.75. **c-d**, For simulations, fluorescence intensity simulation results were obtained using our mathematical model. The estimated diffusion coefficient for $A_{3OC12HSL}$ is $83\,\mu m^2/s$ and for I_{C4HSL} is $1810\,\mu m^2/s$.

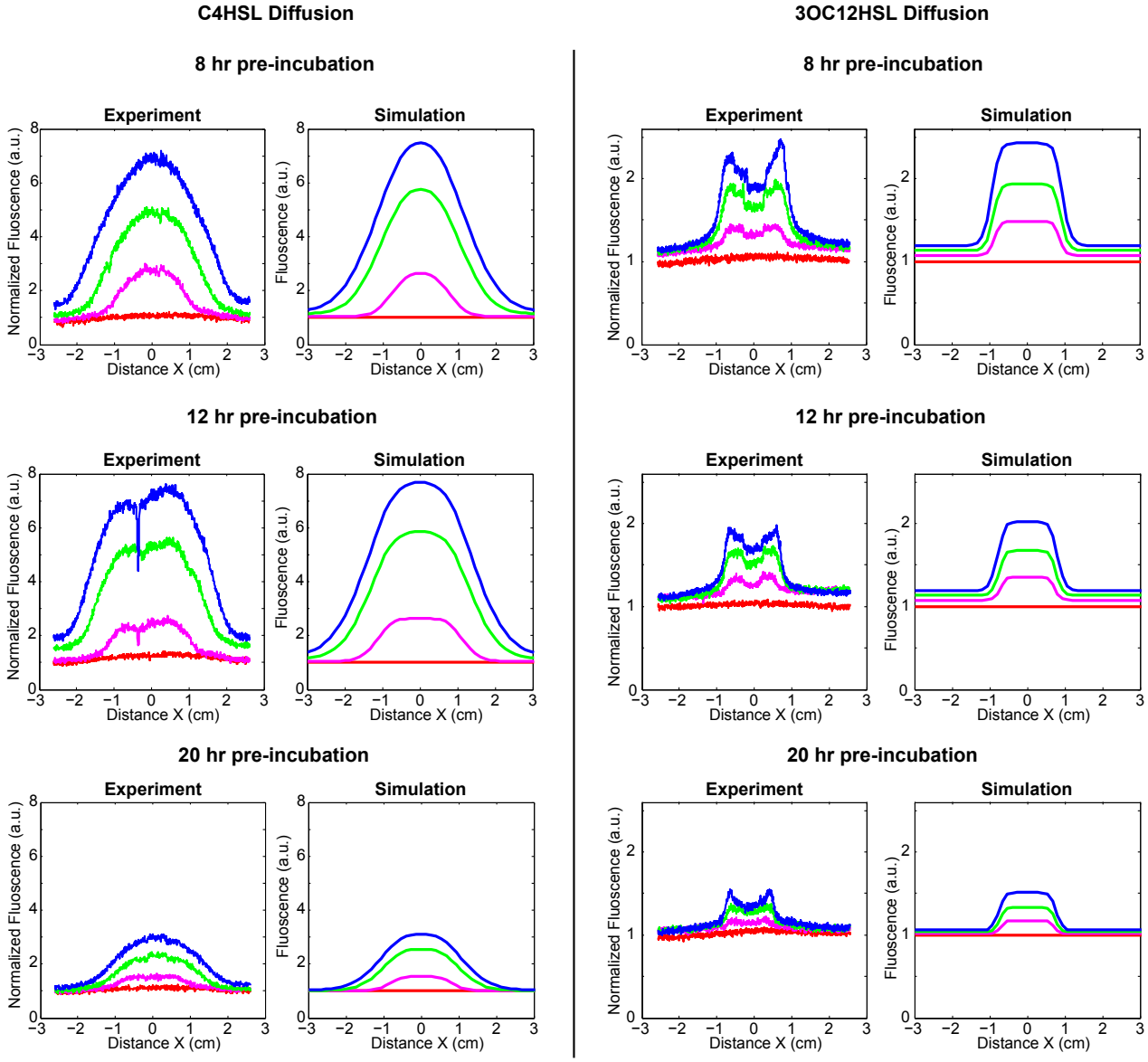

Fig. S7. Additional experiments to verify that diffusion rate calculations are reasonably robust to changing biofilm characteristcs over time. Fluorescence intensity of receiver cells in response to AHL gradients in 2% M9 agar plates.The four curves correspond to hours 0, 2.5, 5, and 8.

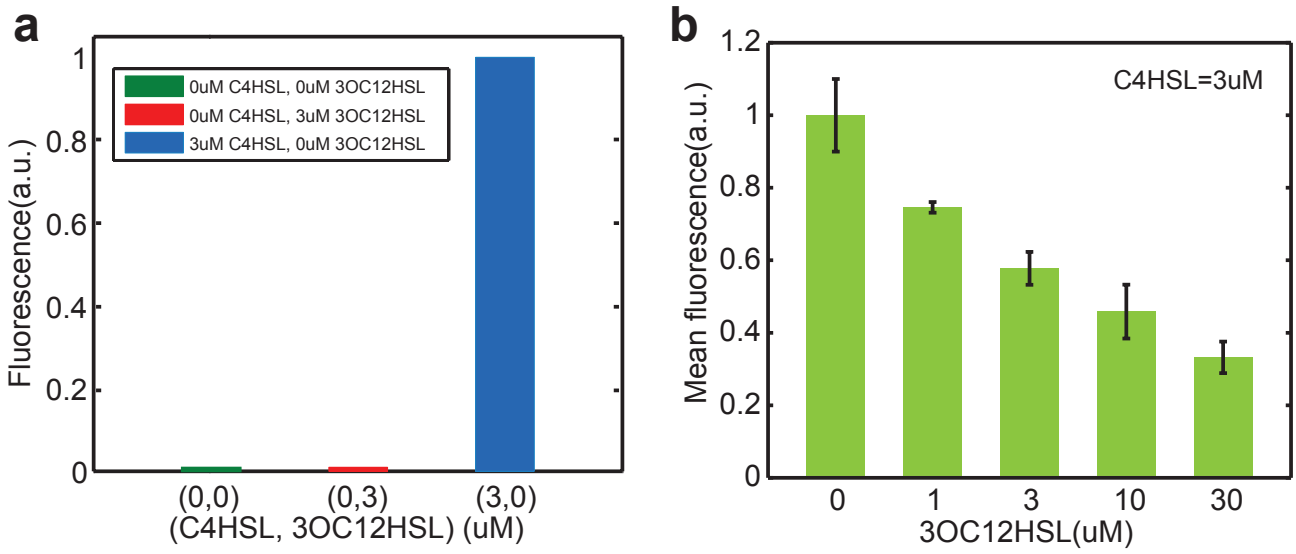

Fig. S8. Competitive binding of $A_{3OC12HSL}$ to RhlR inhibits activation of promoter p_{Rhl} by I_{C4HSL}. **a**, GFP expression from p_{Rhl} promoter is induced by I_{C4HSL} (blue bar) but is not induced by $A_{3OC12HSL}$ (red bar). **b**, GFP expression from p_{Rhl} promoter decreases with $A_{3OC12HSL}$ for a fixed concentration of I_{C4HSL}.

Fig. S9. Populations of *E. coli* expressing constitutive fluorescent reporter proteins GFP or mCherry were mixed in various ratios of [Green:Red] on M9 supplemented minimal media and then imaged by microscopy. Scale bar, $200\,\mu\mathrm{m}$.

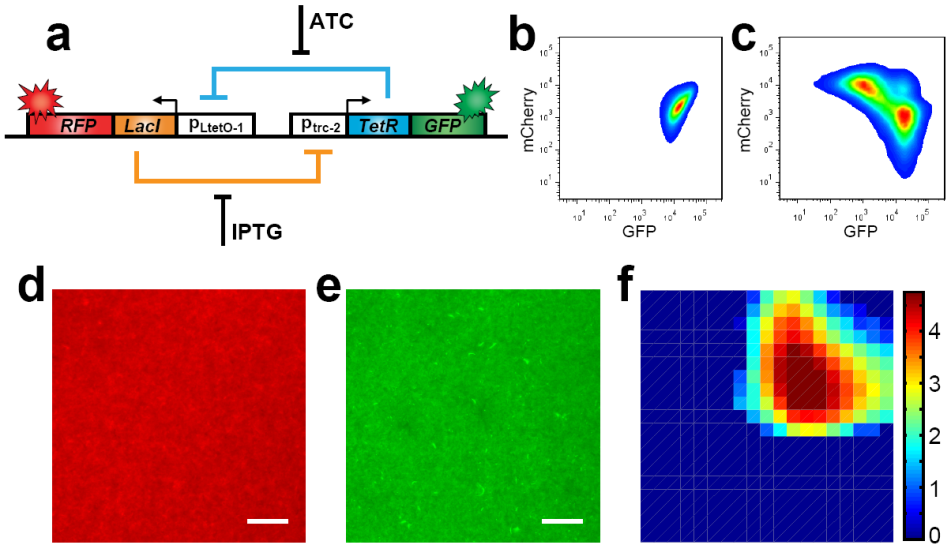

Fig. S10. Behavior of cell populations with each cell harboring an intracellular green/red bistable toggle switch. **a**, A bistable toggle switch derived from Gardner *et al* (20). **b**, Flow cytometry fluorescence density plot of the toggle cells at time 0. **c**, Flow cytometry fluorescence density plot of cells scraped from the cell lawn at 24 hours. **d**-**e**, Microscope images of cell lawns harboring the toggle switch circuit at 24 hours. Both RFP (**d**) and GFP (**e**) are homogeneously distributed and qualitatively different from that of a population carrying the emergent circuit in Fig. 2**a**. Scale bar, $100\,\mu\mathrm{m}$. **f**, Fluorescence density plot of the microscope images in panels **d**-**e**.

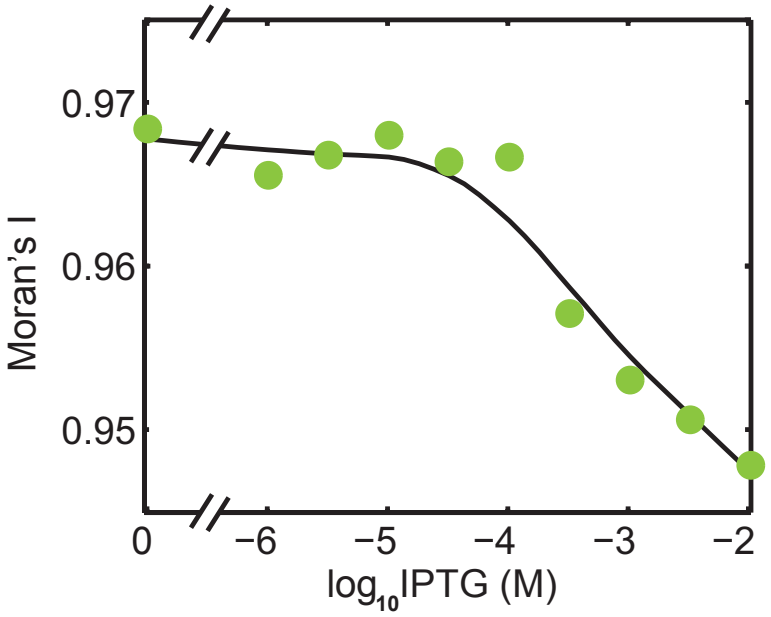

Fig. S11. Moran's I of the patterns from our deterministic simulations.

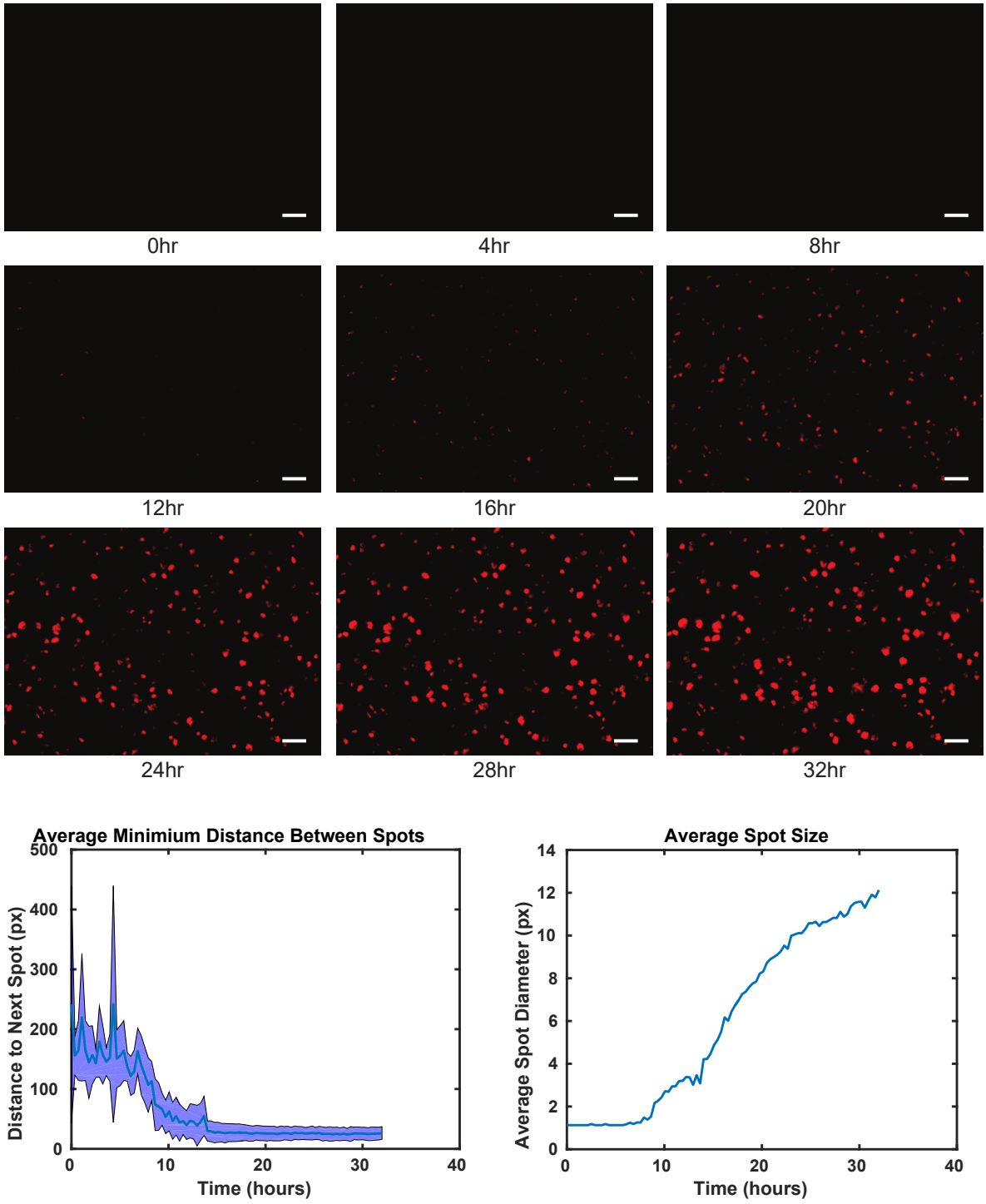

Fig. S12. Emergence of patterns over time. Snapshots of red fluorescence were taken every 30 minutes for 32 hours. Shown are images in 4-hour intervals. Scale bar, $100\,\mu\mathrm{m}$. Left: Average minimium distance between spots as a function of time, blue shading indicates standard deviation. Right: Average spot diameter as a function of time.

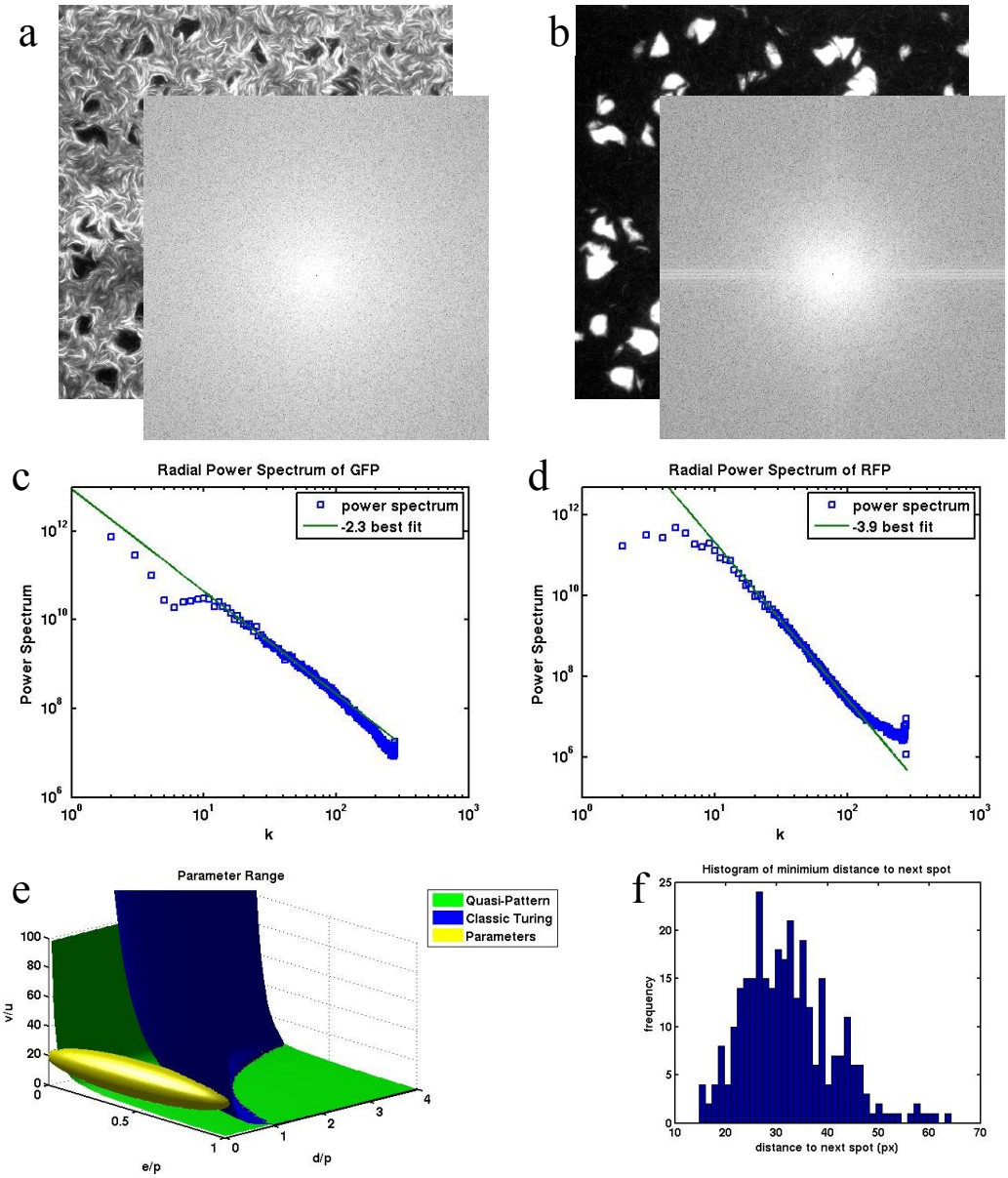

Fig. S13. a, GFP image and corresponding Fourier transform. **c**, Radial power spectrum of GFP and power law fit of -2.3. **b**, RFP image and corresponding Fourier transform. **d**, Radial Power spectrum of RFP with a powerlaw tail fit of -3.9. **e**, Pattern forming regimes in parameter space and estimated parameters for our system. The parameters fall above the region where stochastic patterns form but below the region where normal Turing patterns form. **f**, Characteristic separation of spots with average separation of $32 \pm 8px$ (45 ± 11 μm).

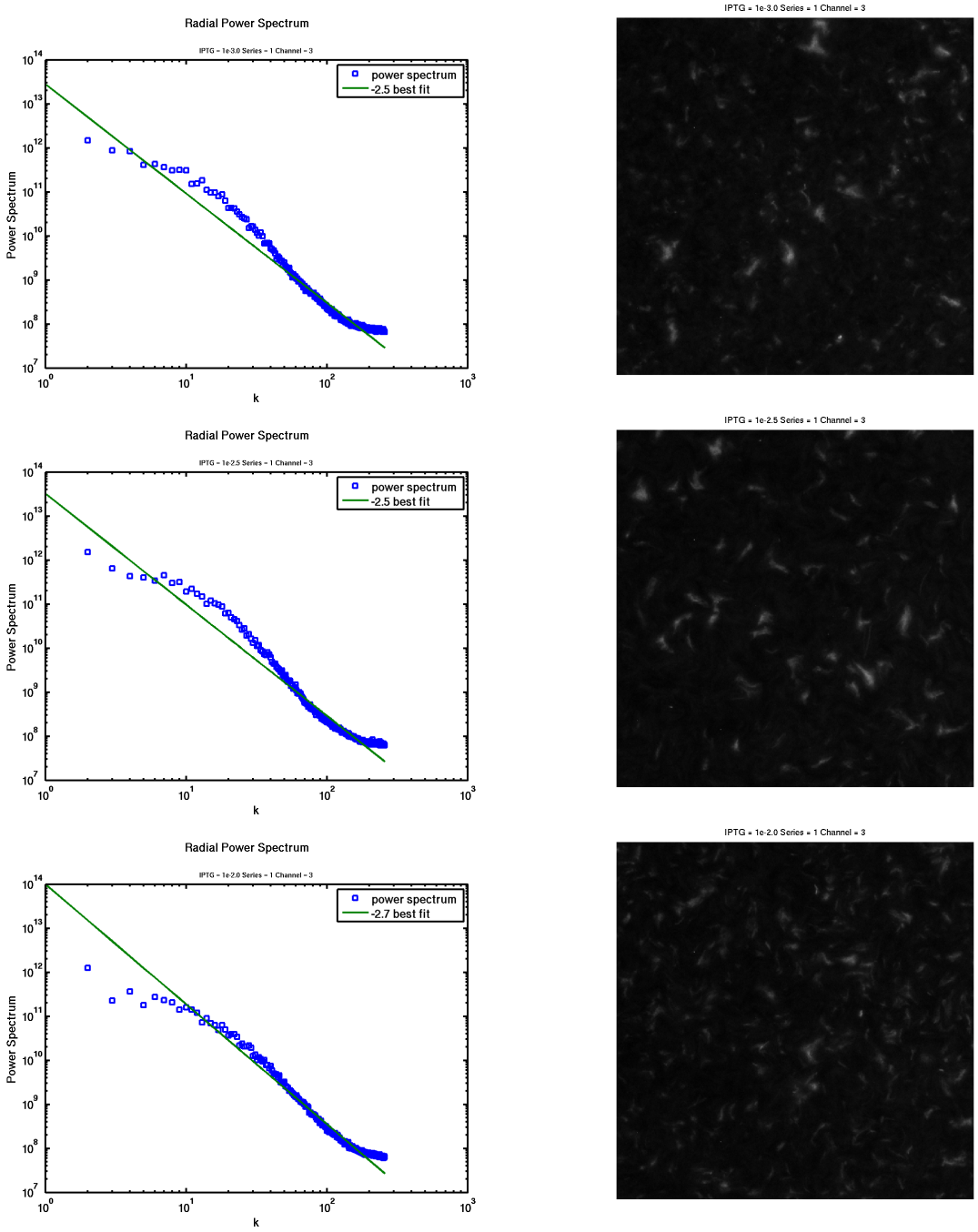

Fig. S14. RFP images and their corresponding Radial Power spectrums with powerlaw tail fits of -2.5, -2.5, -2.9 for IPTG concentrations of 10^{-3} M, $10^{-2.5}$ M, and 10^{-2} M respectively.

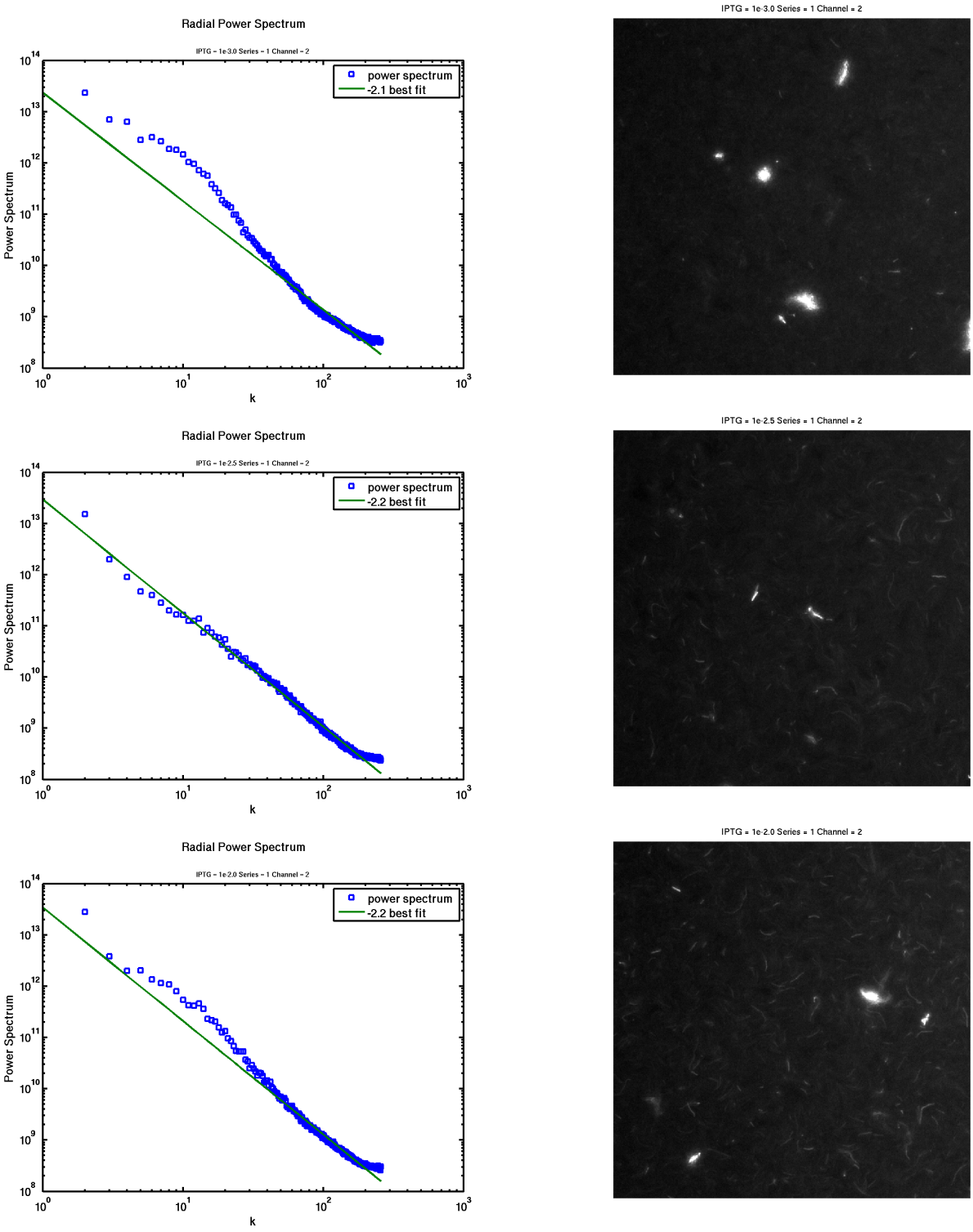

Fig. S15. GFP images and corresponding Radial Power spectrums with a powerlaw tail fits of -2.1, -2.2, -2.2 for IPTG concentrations of 10^{-3} M, $10^{-2.5}$ M, and 10^{-2} M respectively. At IPTG concentrations smaller than 10^{-4} M The green channel begins to look spatially homogeneous as the signal is not strong enough to show-up beyond the background camera noise.

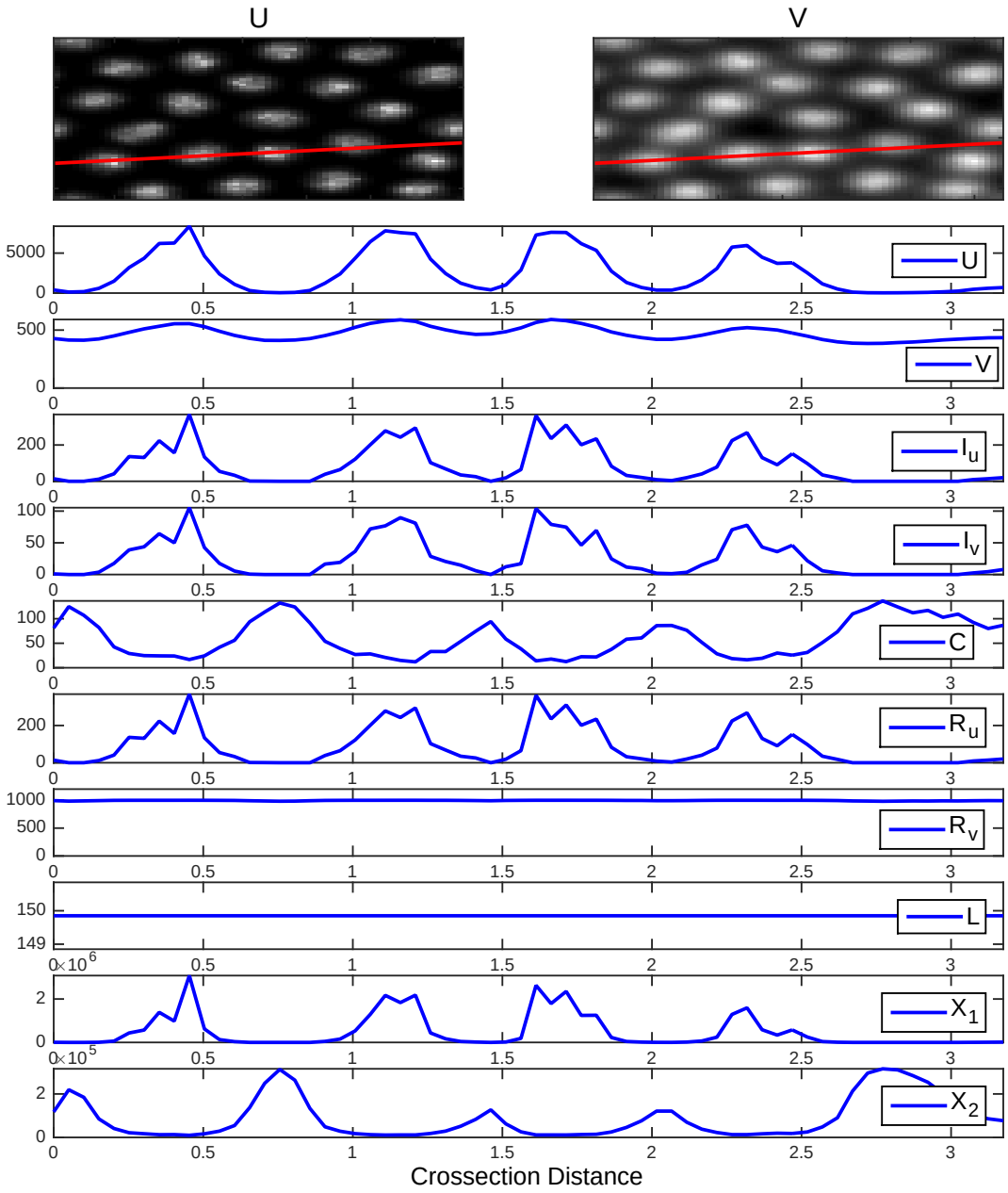

Fig. S16. $A_{3OC12HSL}$ and I_{C4HSL} patterns produced in our stochastic simulation using the parameters given in Tables S6-S7. The red line indicates the location of the cross-section used for all other dynamic variables. Cross-sectional slices of variables U ($A_{3OC12HSL}$), V (IC4HSL), I_u (LasI), I_v (RhlI), C (CI), R_u (LasR), R_v (RhlR), L (free LacI), X_1 (LasR-$A_{3OC12HSL}$ complex), and X_2 (RhlR-I_{C4HSL} complex).

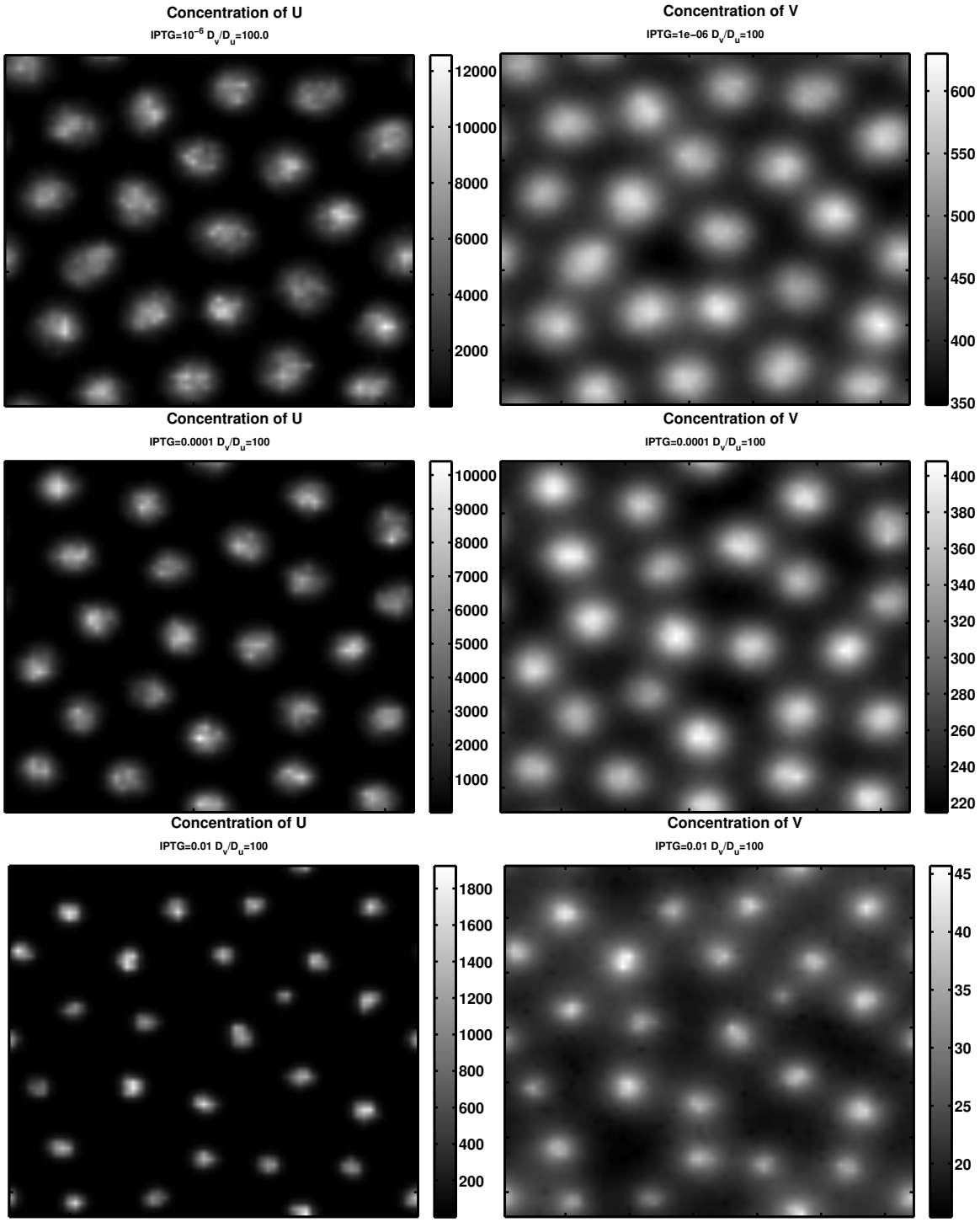

Fig. S17. $A_{3OC12HSL}$ patterns produced in our stochastic simulation using $D_v/D_u = 100$ and the parameters given in Tables S6-S7 for three different concentrations of IPTG.

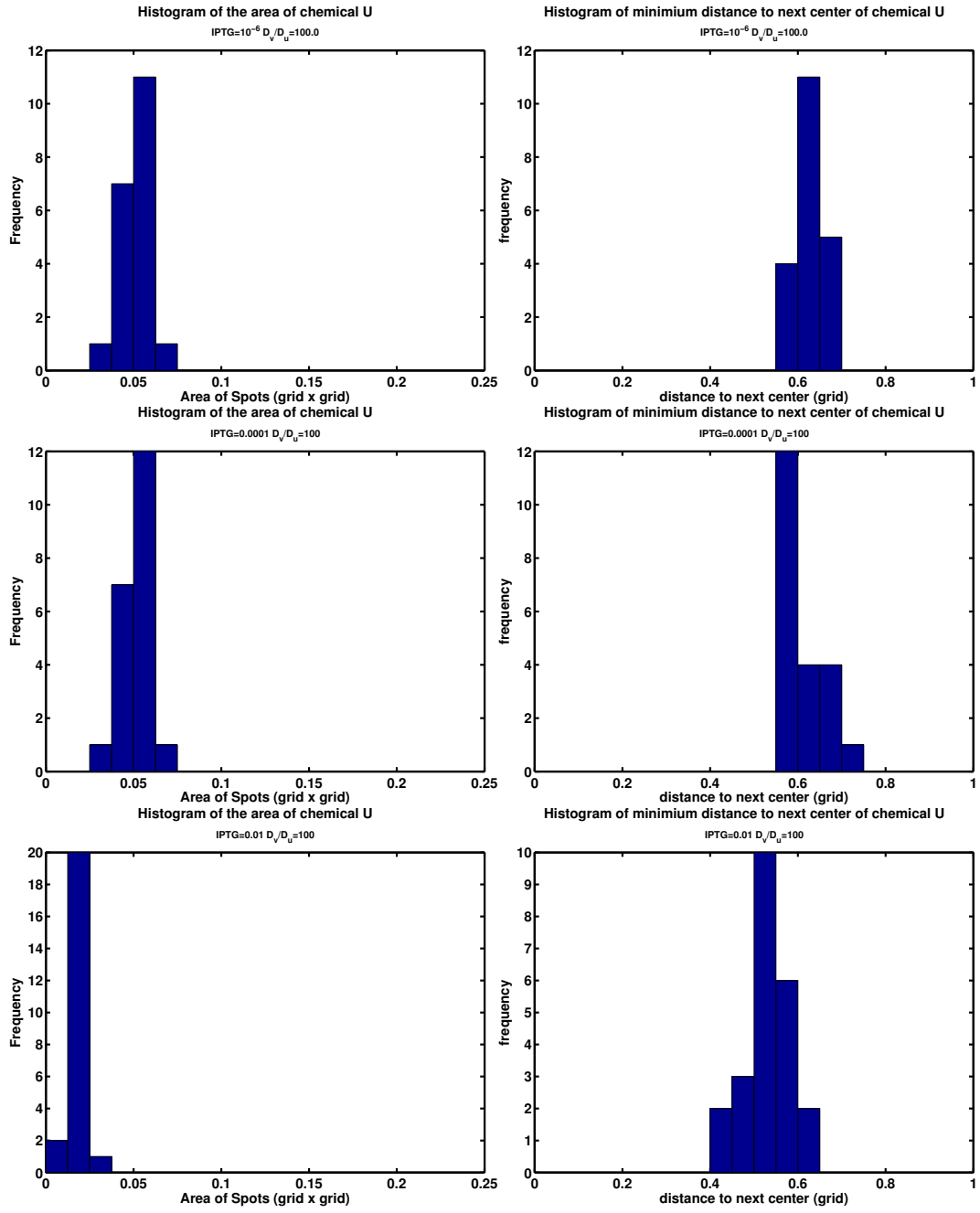

Fig. S18. Spot size and spacing distributions for 30C12HSL produced in our stochastic simulation with $D_v/D_u = 100$ for three different values of IPTG.

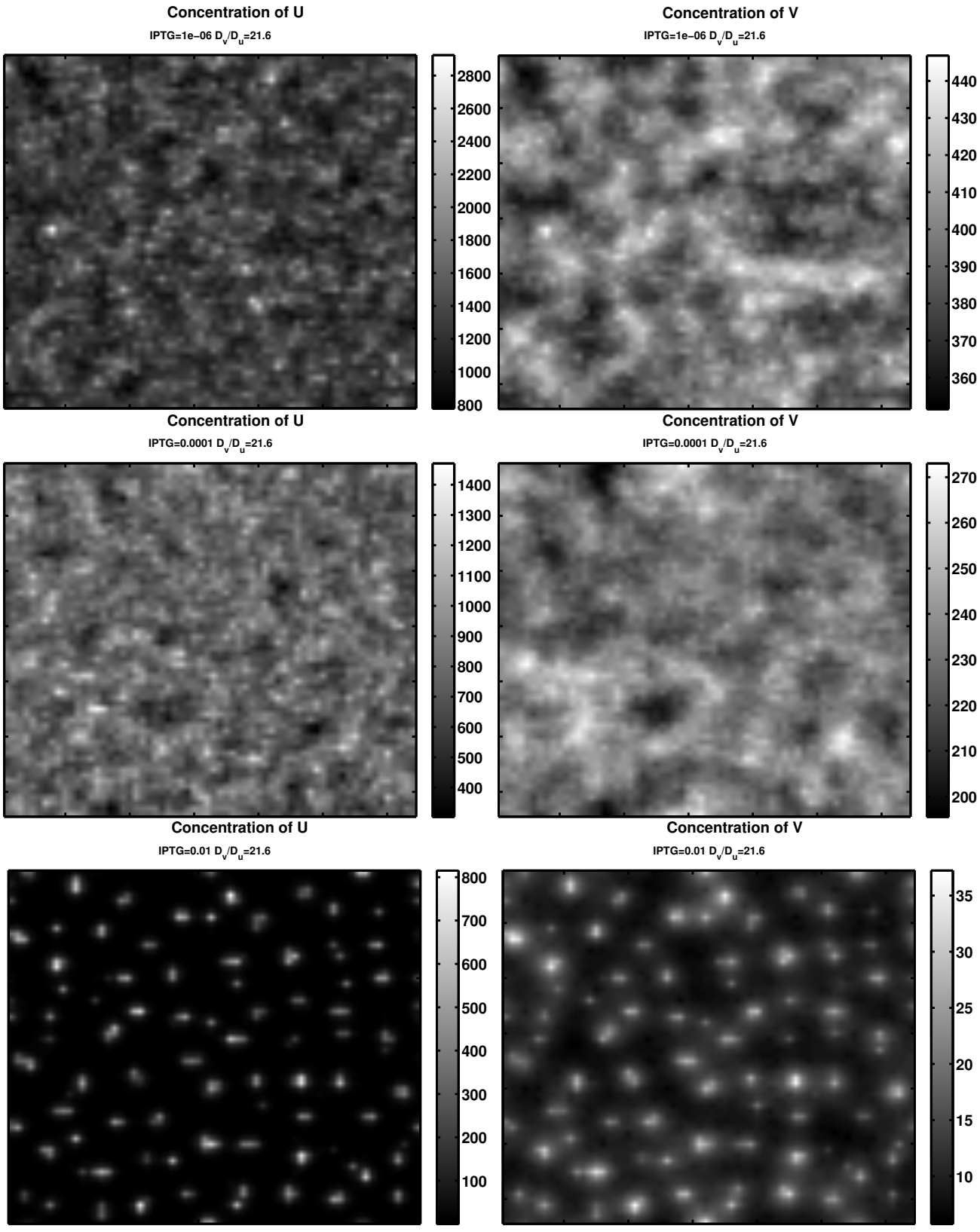

Fig. S19. $A_{3OC12HSL}$ patterns produced in our stochastic simulation using the measured diffusion ratio of $D_v/D_u = 21.6$ and the parameters given in Tables S6-S7 for three different concentrations of IPTG.

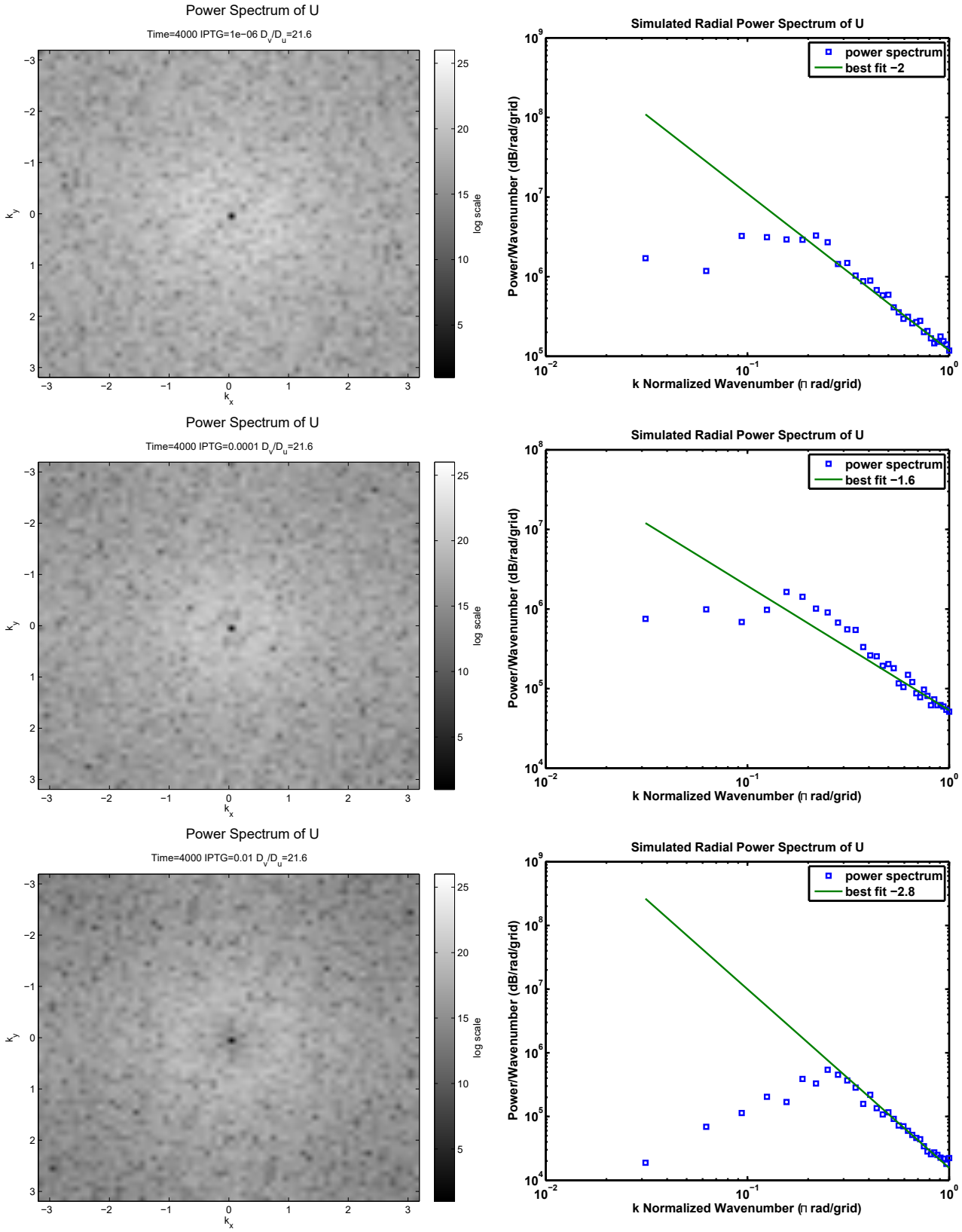

Fig. S20. 2D power spectrum and radial power spectrum for 30C12HSL produced in our stochastic simulation using $D_v/D_u = 21.6$ for three different values of IPTG.

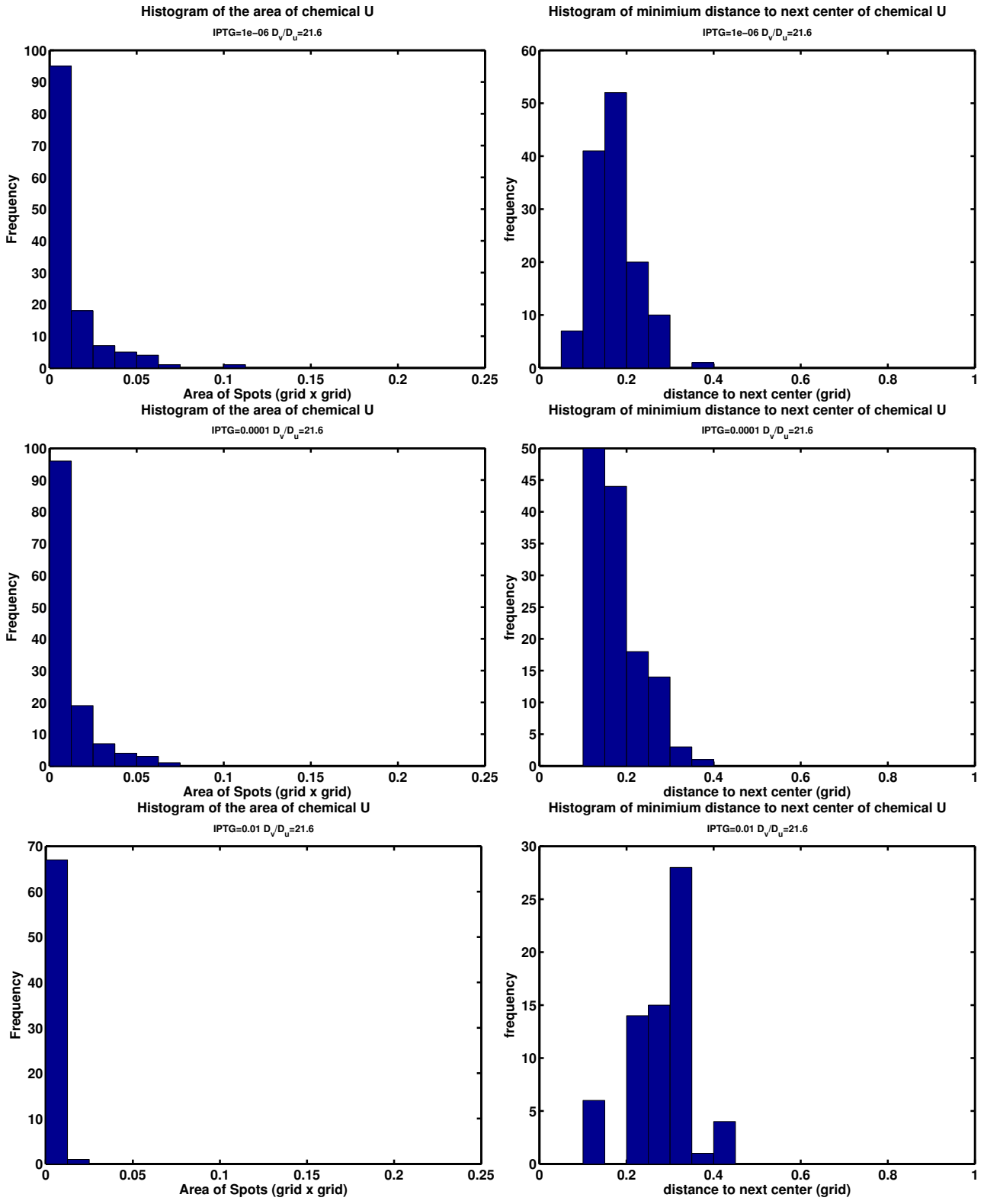

Fig. S21. Spot size and spacing distributions for 30C12HSL produced in our stochastic simulation using $D_v/D_u = 21.6$ for three different values of IPTG.

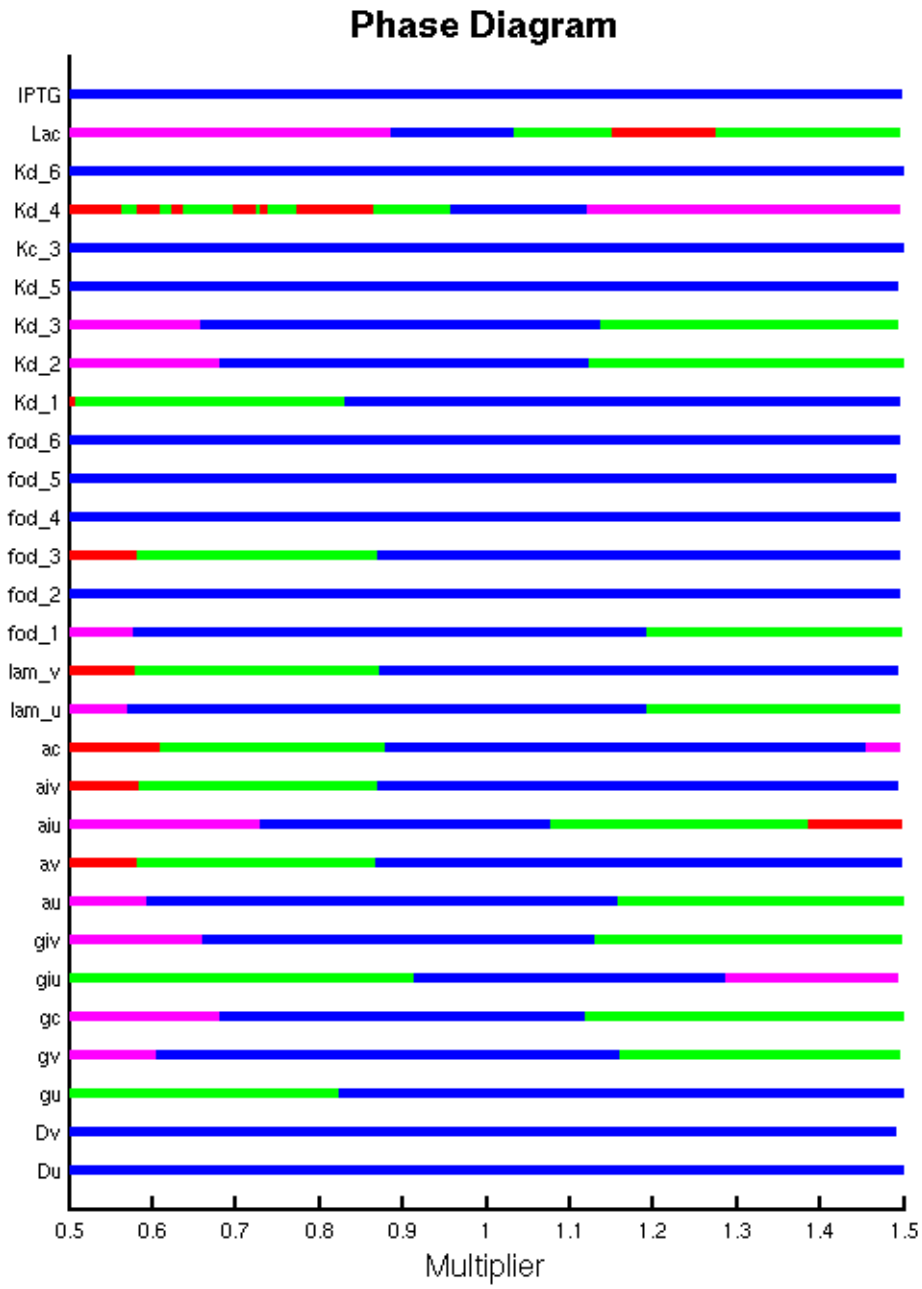

Fig. S22. Phase Diagram showing the type of phase as each parameter is varied from half of its nominal value to 1.5x its nominal value while keeping all other parameters fixed. Red indicates an unstable fixed point, magenta a stable homogeneous state, blue a stochastic pattern, and green deterministic Turing pattern.

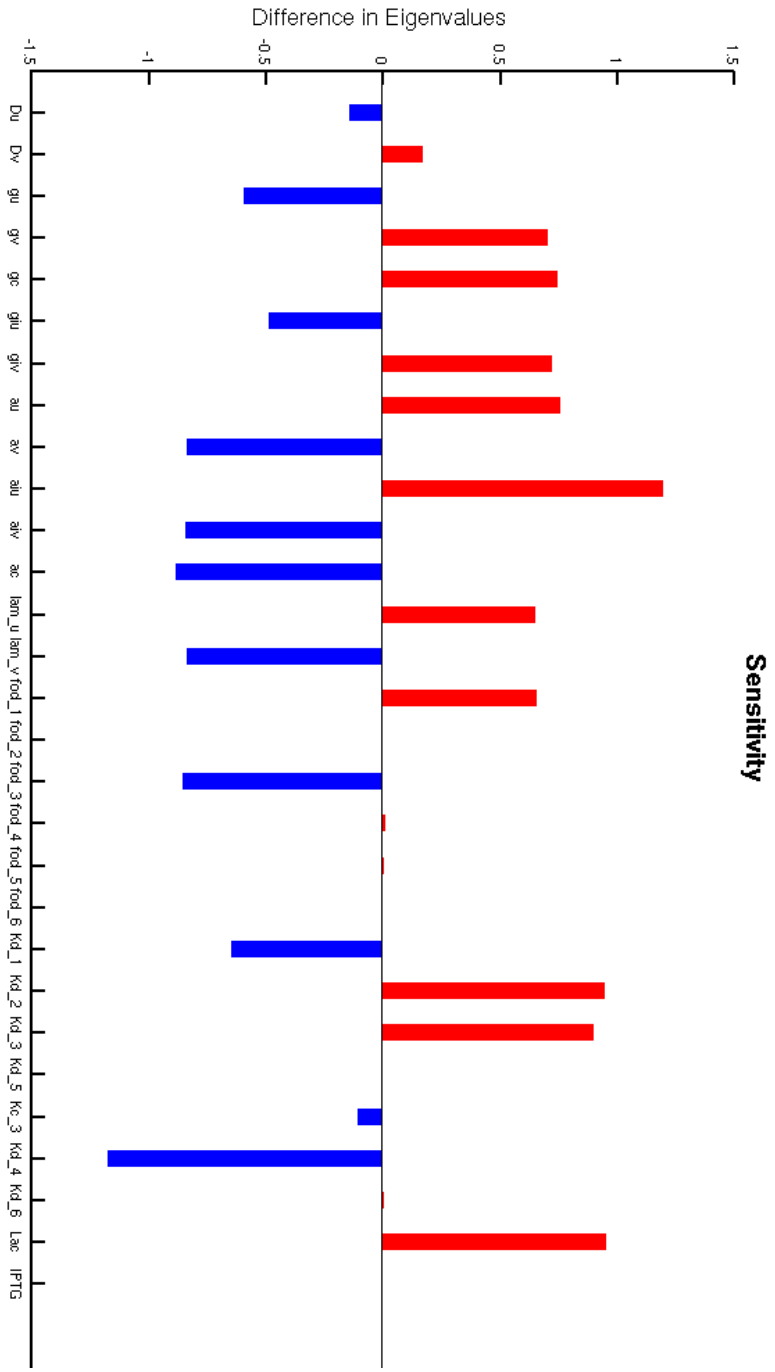

Fig. S23. Sensitivity of a phase to a parameter is indicated by plotting the difference in eigenvalues between 1.5x the nominal value of a parameter and half of the nominal value. Red indicates a parameter that when increased promotes traditional Turing patterns and blue indicates a parameter promoting stochastic patterns.

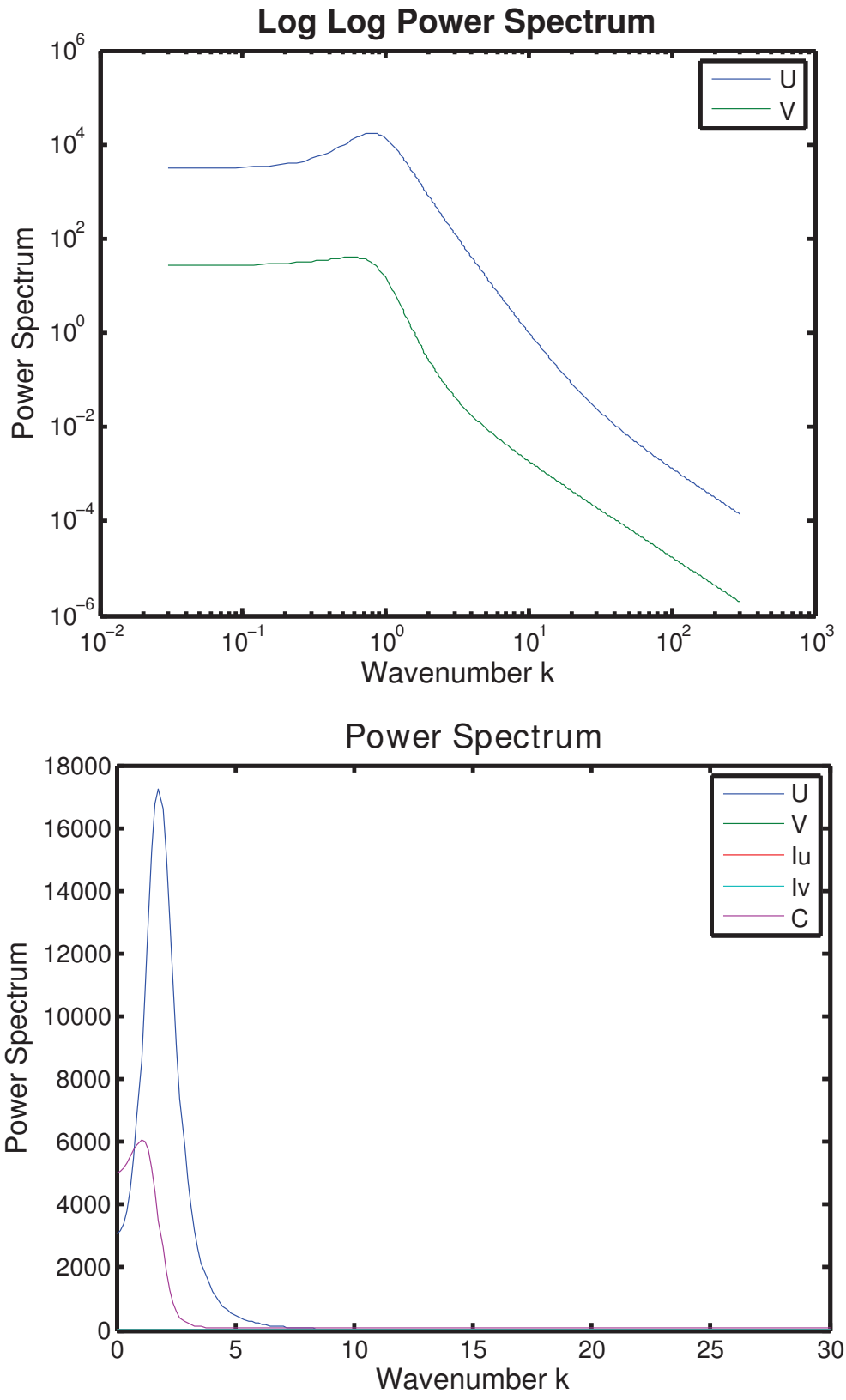

Fig. S24. The Analytic power spectrum calculated for the parameter set given in Tables S1-S2.

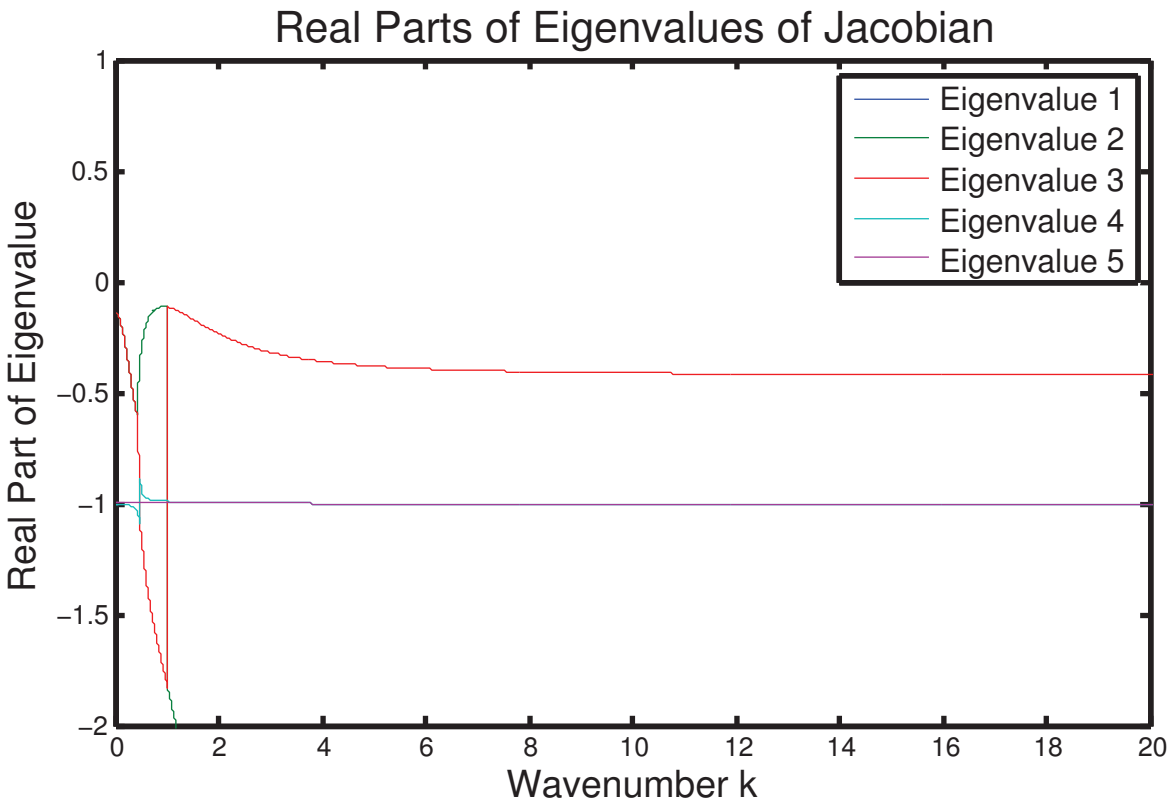

Fig. S25. The real part of the eigenvalues of the Jacobian for the parameter set given in Tables S1-S2 plotted as a funtion of k. All the eigenvalues are negative indicating that the pattern formed is stochastic.